Title
Low-Energy Clock Generation for Internet-of-Things Applications

Author
Esmaeelzadeh, Hani

Publication Date
2019

Peer reviewed|Thesis/dissertation

UNIVERSITY OF CALIFORNIA

Los Angeles

Low-Energy Clock Generation for Internet-of-Things Applications

A dissertation submitted in partial satisfaction
of the requirements for the degree
Doctor of Philosophy in Electrical and Computer Engineering

by

Hani Esmaeelzadeh

2019

ABSTRACT OF THE DISSERTATION

Low-Energy Clock Generation
for Internet-of-Things Applications

by

Hani Esmaeelzadeh
Doctor of Philosophy in Electrical and Computer Engineering
University of California, Los Angeles, 2019
Professor Sudhakar Pamarti, Chair

Aggressively duty-cycling the operation of a system between ON and OFF states has proven to be the most effective way to reduce the average power consumption in energy-constrained applications such as Internet-of-Things (IoT). Since these devices are either battery-powered with a very small form factor or rely on energy harvesting where small amount of ambient energy is captured to power up the device, ultra-low power consumption is crucial in enabling all the advantages that applications such as IoT and biomedical implantable/wearable devices are expected to produce. However, the amount of power saving in a duty-cycled system is usually constrained by two main factors: 1) the start-up time of the system; and 2) the OFF-state power consumption. The system start-up time is usually limited by the long start-up time of its reference oscillator, typically a high-Q, MHz-range crystal oscillator that usually takes several milliseconds to turn on. The OFF-state (sleep) power consumption, on the other hand, is dominated by the sleep timer that is an always-ON 32KHz crystal oscillator. Sleep timer synchronizes the transmitting and receiving bursts which requires a very accurate oscillation frequency to minimize the guard band in order to reduce the active energy consumption. To address the mentioned challenges, we have developed circuit techniques and architectures that enable low-power clock generation.

To kick-start high-Q oscillators, such as crystal and/or MEMS-based reference oscillators, pre-energization of the resonator through injecting energy for a precise duration is proposed.

A universal analysis for energy injection into high-Q resonators is developed and used to calculate the optimal injection duration essential to obtain a minimum start-up time. The proposed method ameliorates the sensitivity of the start-up time to the matching between the injection and resonance frequencies. To further relax the frequency accuracy requirement of the injection oscillator, energy injection with a dynamically-adjusted injection duration is presented. Measurement results from a 65nm CMOS IC show that the proposed technique reduces the start-up time of multiple tested crystal oscillators to about 100-120 number of oscillation cycles. The measured start-up time using the proposed precisely-timed energy injection method is 15 times faster than the best case reported in the literature while consuming the lowest start-up energy of $\sim$12nJ.

In order to reduce the sleep power consumption, an ultra-low power sleep timer that is based on a DC-only sustaining amplifier is presented. New oscillator architecture is proposed that enables sub-nW power consumption in a 32KHz crystal oscillator by amplifying the oscillation signal at DC, instead of amplifying it at the oscillation frequency. Measurement results of 20 different 65nm standard CMOS dies show an average power consumption of 0.55nW drawn from a 0.5V supply at room temperature for a 32KHz crystal oscillator. The measured long-term stability of the sleep timer indicated by the Allan deviation floor is 14ppb. The proposed oscillator architecture does not require any calibration schemes or multiple supply domains, unlike most prior art.

The dissertation of Hani Esmaeelzadeh is approved.

Milos D. Ercegovac

Subramanian S. Iyer

C.-K. Ken Yang

Sudhakar Pamarti, Committee Chair

University of California, Los Angeles

2019

To my mother ...

TABLE OF CONTENTS

1 Introduction **1**

1.1 Motivation 1

1.2 Dissertation Outline 4

2 Start-Up Time in High-Q Oscillators **6**

2.1 Introduction 6

2.2 Equivalent Circuit 8

2.3 General Form of a High-Q Oscillator 12

2.4 Start-Up Behavior of High-Q Oscillators 15

2.5 Prior Art 17

3 Precisely-Timed Energy Injection for Fast Start-Up of High-Q Oscillators 21

3.1 Introduction 21

3.2 Pre-energization: Preview and Challenges 24

3.3 Precisely-Timed Energy Injection 27

3.3.1 Concept 27

3.3.2 Injection Duration $\left(T_{inj}\right)$ 29

3.3.3 PVT-Invariant Injection Duration 31

3.4 Impact of Injection Frequency and Duration Errors on Start-Up Time 32

3.4.1 Tolerable Injection Frequency Error (TIFE) 34

3.4.2 Tolerable Injection Duration Error (TIDE) 37

3.5 Circuit Implementation 38

3.5.1 Crystal Oscillator With Amplitude Regulator Loop 39

3.5.2 Temperature-Compensated Ring Oscillator 40

3.5.3 Buffer 41
3.6 Measurement Results and Comparison 42
3.7 Extended Tolerable Injection Frequency Error 52
3.8 A Comparison of Injection-Based Fast Start-Up Techniques 55

4 Ultra-Low Power 32KHz Crystal Oscillator 63
4.1 Performance Requirement of Sleep Timers 64
4.2 Pierce XO as a Sleep Timer 65
4.3 Review of Prior Art 67
4.4 Sub-nW Sleep Timer Based on a DC-Only Sustaining Amplifier 70
4.4.1 Theory of Operation 72
4.4.2 Frequency Conversion Using Orthogonal I/Q signals 73
4.4.3 Ultra-Low Power Realization 77
4.4.4 Effect of Nonidealities 82
4.4.5 Circuit Implementation 87
4.4.6 Measurement Results 94

5 Conclusion 102

A Derivation of high-Q oscillator's motional current envelope 104

B Time-domain derivation of oscillator's motional current 106

References 109

LIST OF FIGURES

1.1 A typical power profile of a duty-cycled IoT device. 3

1.2 A simplified block diagram of a generic IoT radio. 4

2.1 Quartz crystal resonator: (a) simplified structure (b) symbol. 7

2.2 Equivalent circuit of a high-Q resonator: (a) with all possible modes (b) with a single mode of interest. 9

2.3 (a) Magnitude and (b) phase of a high-Q resonator over frequency. 10

2.4 Parallel-resonance oscillation at ω_{SS}. 11

2.5 General form of an oscillator: (a) combination of the resonator with a nonlinear circuit (b) splitting into motional impedance Z_m and circuit impedance Z_C. . . 12

2.6 Nonlinear oscillation mechanism: (a) equivalent circuit of the oscillator (b) intersection of the locus of $Z_C(|i_m|)$ with that of $-Z_m$. 13

2.7 Amplitude control loop by bias regulator. 14

2.8 Variation of the time constant during oscillation buildup. 16

2.9 Transient response of an oscillator during start-up. 17

2.10 Traditional quick start-up techniques by increasing the negative resistance: (a) by increasing the transconductance of the active circuit (b) by initially decreasing the capacitive load. 19

2.11 Quick start-up of a high-Q oscillator by pre-energizing the resonator. 20

3.1 (a) General form of an oscillator (b) start-up time improvement through "pre-energization" of the resonator. 22

3.2 Transient response of the motional current of a high-Q resonator driven by a square-wave/sinusoidal injection signal. 25

3.3 Impact of injection duration on the start-up time for three different cases of (a) short, long, and (b) optimum injection durations. 26

3.4 Prior solutions to overcome the frequency mismatch problem: (a) chirp injection (b) dithered injection. 27

3.5 Sensitivity of the proposed precisely-timed energy injection to the variations in the injection frequency (a) in frequency domain, the injection signal is a relatively wideband sinc function (b) start-up time of the proposed solution is much less sensitive to the frequency mismatch as opposed to the conventional case. 28

3.6 A resonator driven by an arbitrary injection signal. 30

3.7 Constant, PVT-insensitive injection duration by making the injection amplitude (V_{inj}) track the steady-state oscillation amplitude ($V_{m,SS}$). 31

3.8 Simulation result of amplitude settling error versus frequency settling error for a 50MHz crystal oscillator. 33

3.9 Impact of $\Delta\omega_{inj} = \omega_{inj} - \omega_m$ on amplitude settling. 33

3.10 Variations in $I_{m,SS}$ as a function of frequency mismatch, $\Delta\omega_{inj} = \omega_{inj} - \omega_m$. In order to maintain an ε variation in $I_{m,SS}$, the frequency mismatch needs to be kept within $\pm 5\sqrt{\varepsilon}/T_{inj}$. 35

3.11 TIFE versus the tolerable amplitude/frequency settling errors for $\lambda = 2$ and $p = 2000$ppm. 36

3.12 Block diagram of the proposed fast start-up crystal oscillator. 38

3.13 Steady-state oscillation amplitude, $V_{m,SS}$, of a crystal oscillator with an amplitude-regulator loop linearly varies over temperature. 40

3.14 Temperature-compensated, current-starved ring oscillator [1] (a) schematic (b) measured variation of oscillation frequency over temperature. 41

3.15 A simple technique to reduce the output slew rate variation of the buffer under temperature variations. 42

3.16 Implemented test-board including the fabricated IC and six different tested crystal devices. 43

3.17 Measured transient response of the 10MHz oscillator during start-up (measured at the gate of M_1 in Fig. 3.12) for three different injection durations: start-up time is minimized for $T_{inj,opt.} = 7.7\mu s$. 45

3.18 Measured start-up sensitivity of the 10MHz oscillator (a) sensitivity to the variations in the optimal injection duration (b) sensitivity to the injection frequency mismatch: proposed technique shows more than 20x faster start-up with much less sensitivity to the injection frequency. 46

3.19 Measured start-up time variation of the 10MHz crystal oscillator over temperature: (top) 80% variation in start-up time when injection duration is arbitrarily chosen to 6μs, (bottom) start-up time and its variation are significantly reduced when the optimal injection duration of 7.7μs is applied. 49

3.20 Measured crystal oscillator start-up variations over temperature for six different crystal devices (ESR ranging from 15Ω to 750Ω) at three different frequencies. . 50

3.21 Extending the frequency insensitivity range of the 10MHz oscillator by dynamically adjusting the injection duration (measured results). 53

3.22 A possible implementation of the dynamically-adjusted injection duration technique to extend the TIFE, hence the temperature range. 54

3.23 Power spectral density of different injection duration. 56

3.24 Frequency variation of a linear chirp-modulated signal over time. 57

3.25 Normalized spectrum of a chirp-modulated signal with $\Big(\Delta f_{chirp} = 10\% f_m, T_{chirp} = 100\mu s\Big)$, and $\Big(\Delta f_{chirp} = 50\% f_m, T_{chirp} = 500\mu s\Big)$. 58

3.26 Optimal injection duration of the single-frequency, precisely-timed injection technique compared to the chirp injection technique over different oscillation frequency. 59

3.27 Simulated time-domain waveforms of (a) chirp frequency with $\Delta f_{chirp} = 10\% f_m$ and $T_{chirp} = 100\mu s$ (b) resonator's motional current in response to the chirp waveform (c) resonator's motional current due to a single-frequency injection signal. 60

3.28 Injection frequency profile of a chirped, precisely-timed injection technique. . . . 61

4.1 A simplified timing profile of an IoT radio. 63

4.2 Average power consumption of a duty-cycled radio as a function of the timing accuracy of the sleep timer for various duty-cycle ratios [2]. 64

4.3 Conventional Pierce crystal oscillator. 65

4.4 Power consumption of Pierce crystal oscillators quadratically increases with the oscillation frequency. 66

4.5 Circuit architecture of the ULP XO developed in [3]. 68

4.6 Architecture and waveforms of the self-charging XO proposed in [4]. 69

4.7 Circuit architecture of the XO proposed in [5]. 69

4.8 (a) Basic concept of the proposed ULP XO (b) phase difference between the XO_1 and XO_2 waveforms degrades the frequency stability. 71

4.9 Phase difference across the resonator as a result of mixer's gate-driver. 72

4.10 Employing orthogonal I/Q paths to maintain zero-phase shift across the resonator-series resonance. 73

4.11 Principle of operation of the ULP XO with I/Q frequency conversion. 75

4.12 Frequency response of the ULP TIA. 76

4.13 (a) Output adder functionality (b) low-power implementation of the output adder using 25%-duty-cycle signals, $D_1, \cdots, D_4$. 78

4.14 (a) Realization of V_1 (b) differential implementation is used to realize V_2. 79

4.15 (a) Block diagram of the ULP XO (b) clock timing diagram. 81

4.16 Frequency deviation of a high-Q resonator as a function of phase shift across it. 83

4.17 magnitude and phase of a high-Q resonator's impedance using straight-line phase approximation. 84

4.18 (a) Conventional PTAT current source (b) Ultra-low power PTAT current source. 88

4.19 Trans-impedance amplifier with voltage-controlled feedback resistor to control the gain. 89

4.20 Ultra-low power, low-voltage opamp. 90

4.21 Amplitude control loop. 92

4.22 (a) Delay-locked loop implementation (b) simulated transient response of DLL. . 93

4.23 25%-duty-cycle clock generation circuit. 94

4.24 ULP XO test board and the chip micrograph. 95

4.25 Ultra-low current measurement setup. 96

4.26 Test board: all sensitive traces are surrounded by an equal-potential guard ring/plane (on all PCB layers) to minimize leakage. 96

4.27 Measurement results for 20 dies: (a) power consumption and (b) frequency variations over temperature. 97

4.28 Measurement results for 20 dies: (a) power consumption and (b) frequency variations over supply voltage. 98

4.29 Measured Allan deviation. 99

4.30 Measured sensitivity of the oscillation frequency to intentionally-introduced mismatch in the I/Q phase using external signal generators. 100

4.31 Power contribution of main blocks of the ULP 32kHz XO. 100

B.1 A high-Q resonator driven by an injection signal. 107

LIST OF TABLES

1.1 A comparison of different battery specifications 2

2.1 Conventional quick start-up techniques 18

3.1 Energy consumption breakdown during start-up 47

3.2 Performance summary of the proposed fast start-up technique and comparison with prior art 51

4.1 Performance summary and comparison with state-of-the-art 32kHz XOs 101

ACKNOWLEDGMENTS

I wish to express my sincere gratitude to those people without whom it would not be possible to complete this work.

First and foremost, I would like to thank my advisor, Professor Sudhakar Pamarti, for his continuous support and guidance throughout my PhD and beyond. I am thankful for the unique opportunity he gave me to work on what I desire and for all the time and energy he dedicated especially throughout our many multi-hour one-on-one meetings.

I would also like to express my appreciation towards my doctoral committee members: Professor C.-K. Ken Yang, Professor Subramanian S. Iyer, and Professor Milos D. Ercegovac, for their generous time and support throughout this research. I had the opportunity to learn from their invaluable comments during my Qualifying examination and the thesis review.

I am grateful to the support I received from the staff of the Electrical and Computer Engineering department at UCLA, particularly: Deeona Columbia, Kyle Jung, Ryo Arreola, Mandy Smith, and Fe Asuncion.

I have been fortunate to work among talented researchers at the Integrated Circuits and Systems Lab (ICSL). I learned a lot from their scientific knowledge and benefited from their friendship: Farid Shirinfar, Neha Sinha, Sameed Hameed, Jeffrey Lee, Szu-Yao Hung, Sina Basir-Kazeruni, Alireza Yousefi, Hariprasad Chandrakumar, Dejan Rozgic, Wenlong Jiang, Vahagn Hokhikyan, Shi Bu, and Jiyue Yang. I learned a lot from my technical discussions with Hari. Neha and Sameed helped me a lot during my first tape-out. Shi and Jiyue were extremely helpful in getting things done at UCLA during the last several months of my PhD, while I was away.

Most of all, I would like to take this opportunity to thank my closest friend in life: my amazing mom who has always been there for me through thick and thin. I love you, mom; more than words can say! I am very blessed for having my little brother Mahdi in my life, who's always been the life and soul of the party.

VITA

2011	B.S. (Electrical Engineering) K.N. Toosi University of Technology, Tehran, Iran.
2013	M.S. (Electrical Engineering) Sharif University of Technology, Tehran, Iran.
2014	Graduate Division Fellowship University of California, Los Angeles.
2016	Advanced to PhD Candidacy University of California, Los Angeles.
2016–2017	IC Design Intern Qualcomm Technologies, Inc., San Diego, California.
2016–2017	Broadcom Foundation Fellowship University of California, Los Angeles.
2017	Qualcomm Innovation Fellowship Finalist (twice).
2017–2018	Broadcom Foundation Fellowship University of California, Los Angeles.
2018–2019	Dissertation Year Fellowship University of California, Los Angeles.
2014–2018	Graduate Student Researcher, Electrical and Computer Engineering University of California, Los Angeles.
2018–Present	RF/mm-Wave IC Designer Movandi Corporation, Newport Beach, California.
2018	Predoctoral Achievement Award IEEE Solid-State Circuits Society.

PUBLICATIONS

H. Esmaeelzadeh and S. Pamarti, "A 0.55nW/0.5V 32kHz Crystal Oscillator Based on a DC-Only Sustaining Amplifier for IoT," *IEEE ISSCC*, Feb. 2019.

H. Esmaeelzadeh and S. Pamarti, "A Quick Startup Technique for High-Q Oscillators Using Precisely Timed Energy Injection," *IEEE Journal of Solid-State Circuits*, vol. 53, no. 3, pp. 692-702, March 2018.

H. Esmaeelzadeh and S. Pamarti, "A precisely-timed energy injection technique achieving 58/10/2μs start-up in 1.84/10/50MHz crystal oscillators," *2017 IEEE Custom Integrated Circuits Conference (CICC)*, Austin, TX, 2017, pp. 1-4.

H. Esmaeelzadeh, M. Sharifkhani and M. Shabany, "A low-power 10-Bit 40-MS/s pipeline ADC using extended capacitor sharing," *2014 IEEE International Symposium on Circuits and Systems (ISCAS)*, Melbourne VIC, 2014, pp. 1147-1150.

CHAPTER 1

Introduction

1.1 Motivation

Ultra-low-power (ULP) wireless radios are the key enabler of a wide variety of applications such as Internet-of-Things (IoT) and biomedical implantable/wearable devices. These energy-constrained applications are typically powered by very small batteries. Battery-operated systems have limited energy storage capability due to small form-factors and/or operate in environments that rule out frequent energy replenishment [6]. In recent years, energy harvesting (EH), where small amount of ambient energy is captured and converted into electric power, has also been used as an alternative way to power ULP radios [7–9]. Nonetheless, among other challenges, ultra-low power consumption becomes a necessity for these emerging applications.

In the past decade, significant efforts have been made to reduce the power consumption of wireless radios. For example, the power consumption of Bluetooth/Bluetooth Low-Energy (BT/BLE) radios has been drastically reduced, down to a few mW [10, 11]. However, this is not sufficient as the size of the batteries for IoT applications is often very small and consequently, they have a small capacity. Furthermore, replacing batteries is labor-intensive and typically a maintenance-free operation of several years is required. Table 1.1 summarizes the specifications of some of the commercially available batteries. It shows that as the battery size becomes smaller, its capacity and the maximum current it can support decreases. Therefore, the circuit blocks in a battery-powered system have to be energy efficient with a low instantaneous power consumption as well. For instance, for a coin-size battery cell with 100mAh capacity, the overall power consumption of the radio has to be as low as a few μW to

Table 1.1: A comparison of different battery specifications

Manufacturer	**Product Name**	**Output Voltage (V)**	**Capacity (mAh)**	**Maximum Current (mA)**	**Size (mm^3)**
PowerStream [13]	PGEB014461	3.7	200	400	2684
PowerStream [14]	GMB-300910	3.7	15	120	270
ST [15]	EFL700A39	3.9	0.7	5	129
Cymbet [16]	CBC050	3.8	0.05	0.3	57.6
Cymbet [17]	CBC012	3.8	0.012	0.1	18.75

enable a 10-year life time [12]. This requires that the power consumption of state-of-the-art wireless radios should be reduced by several orders of magnitude without sacrificing their performances, which is very challenging.

In order to reduce the average power consumption, "burst-mode" operation where the system is aggressively duty-cycled between ON and OFF states has been introduced. A simplified, typical power profile of an IoT system is shown over time in Fig. 1.1. As seen, in a burst-mode system, the power-hungry circuitry, i.e. the radio core, is activated only for a short period when needed, and is turned off for most of the time to conserve power consumption. The wake-up function is typically performed by a sleep timer usually running at a real-time frequency, i.e. 32.768KHz. The power reduction in Fig. 1.1 is limited by two main factors: *the start-up time of the system*, and *sleep-mode power consumption*. As will be shown in chapter 2, the start-up time of the system is limited by the start-up time of its reference oscillator, which is typically a MHz-range crystal oscillator (XO). As seen in Fig. 1.1, the XO start-up time is much longer than the active time of the power-hungry

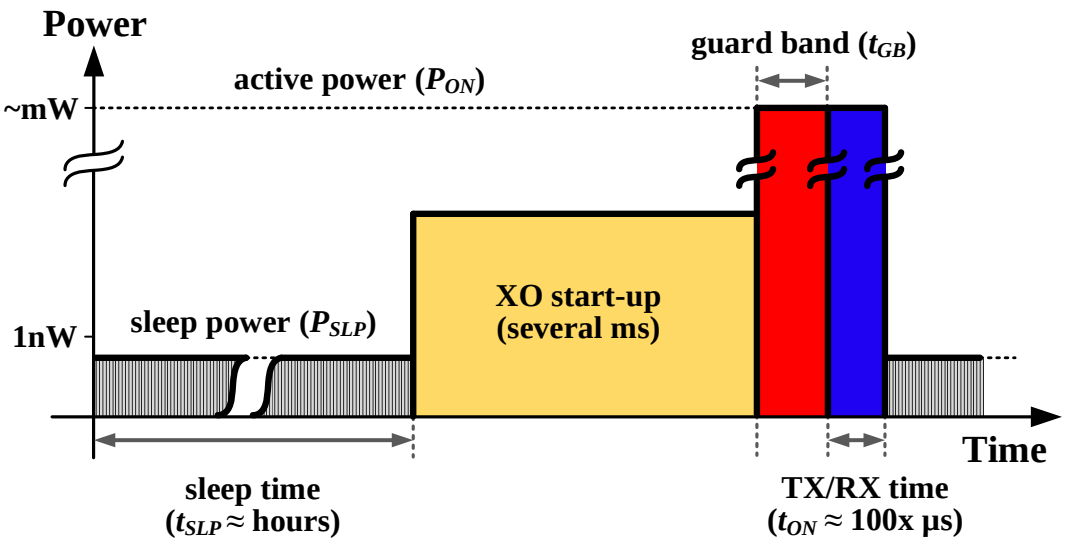

Figure 1.1: A typical power profile of a duty-cycled IoT device.

radio, i.e. TX/RX time which increases the average power consumption. Therefore, it is important to have a quick reference oscillator at start-up in order to reduce the average power consumption. It is also important to have a robust and predictable start-up time that is not sensitive to fabrication process, supply voltage, and temperature (PVT) variations. As discussed in the following chapters, it is very challenging to achieve in reference oscillators because of their extremely high quality factors which make them very slow at start-up (several milliseconds for a MHz-range XO). Furthermore, the start-up time of conventional oscillators relies on the amount of noise in the circuit and it makes the start-up behavior quite random and PVT-sensitive.

The second factor limiting the power saving is the sleep power consumption. As seen in Fig. 1.1, a highly duty-cycled system spends most of the time in the sleep mode. As a result, the sleep power consumption in many cases becomes the dominant contributor to the overall average power consumption of the system. Typically, the sleep power consumption is dominated by the power consumption of the sleep timer and has to be in the nano-watt range. Another important performance factor for the sleep timer is its frequency accuracy. Sleep timer synchronizes the transmitting and receiving bursts. As a result, if its oscillation frequency is not accurate, the receiver has to turn on early during a period called "guard

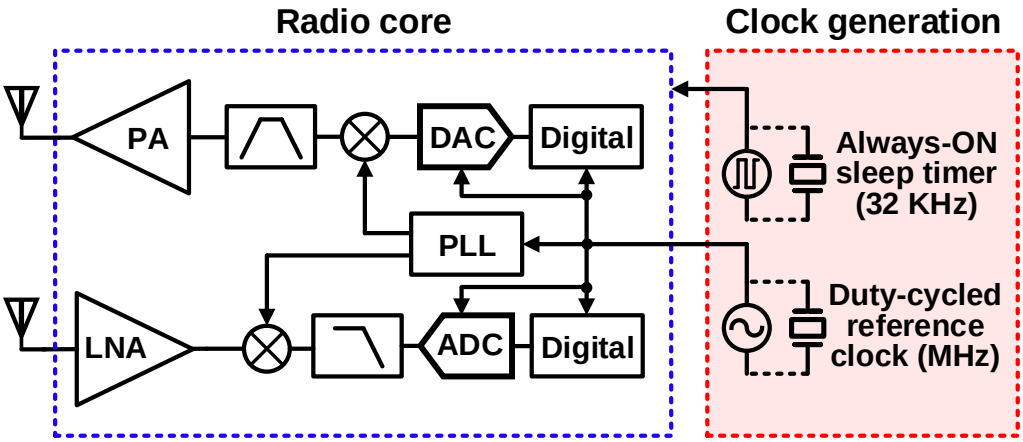

Figure 1.2: A simplified block diagram of a generic IoT radio.

band", denoted by t_{GB} in Fig. 1.1, to make sure that it receive the transmitted packet. This increases the average power consumption as the high-power radio has to be ON during the guard band as well.

Overall, in order to reduce the average power consumption, it is crucial for the reference clock to have a robust and quick start-up, and for the sleep timer to be extremely low power with a high timing accuracy.

A generic radio for IoT applications is shown in Fig. 1.2. The radio core includes the RF frontend as well as the backend digital processing. The scope of this work focuses on the clock generation unit that has two main components: a MHz-range crystal oscillator that provides the reference clock for the radio core and is duty cycled along with the whole radio core to save power; and the always-ON sleep timer which is usually a 32KHz real-time clock that provides time-keeping and synchronization.

1.2 Dissertation Outline

This dissertation addresses the challenges of clock generation for energy-constrained applications such as IoT by (1) proposing a "precisely-timed" energy injection technique to robustly reduce the start-up time of high-Q reference oscillators to only about 100 oscillation cycles;

and (2) introducing a novel oscillator architecture that achieves sub-nW power consumption in sleep timers.

Chapter 2 briefly describes high-Q resonators such as quartz crystal and MEMS, and goes over their electrical model. The nonlinear start-up behavior of high-Q oscillators is discussed with a review of prior art on start-up reduction techniques along with their challenges and shortcomings.

Chapter 3 takes an in-depth look at the different injection-based start-up techniques and details the proposed "precisely-timed" energy injection, describing the technique and important circuit design aspects that reduce it to practice, especially over PVT variations. The challenges associated with the "pre-energization" technique, namely *sensitivity to injection frequency* and *long transient time* are discussed in detail and addressed by the proposed technique. A universal analysis for energy injection into high-Q resonators is presented and used to calculate the optimal injection duration essential to obtain a minimum start-up time. Measurement results from a 65nm standard CMOS IC is provided as a proof-of-concept. The chapter concludes with a detailed comparison of chirped, dithered, and precisely-timed injection techniques.

Chapter 4 introduces the new ultra low power oscillator architecture for sleep timers. After going over the performance requirements of sleep timers and a review of the prior art, a sub-nW sleep timer architecture based on a DC-only sustaining amplifier is introduced. The impact of nonidealities on the performance of the proposed sleep timer is analyzed in detail and followed by the circuit implementation. Measurement results over 20 different 65nm standard CMOS dies show an average power consumption of 0.55nW at room temperature with an Allan deviation floor of 14ppb[1].

Chapter 5 concludes the dissertation by summarizing the key contributions.

[1]part per billion

CHAPTER 2

Start-Up Time in High-Q Oscillators

High-Q oscillators such as crystal- or MEMS-based oscillators are extensively used in electronic systems to generate the clock signal for digital and analog circuits as well as timekeeping applications. Their indispensable role in electronic systems stems from their unparalleled precision and stability. The precision and stability of high-Q resonators, e.g., quartz crystal or MEMS, is several orders of magnitude better than their integrated electronic counterparts. This is because there is no combination of available electronic components that is more precise and constant with time and temperature. The high quality factor of crystal/MEMS resonators makes them extremely slow at start-up such that the agility of the whole system is limited to the start-up time of the high-Q resonator. Slow start-up becomes problematic in energy-constrained systems such as IoT where ultra-low power consumption is achieved by intermittent operation of the system. This chapter starts with introducing the basics of quartz crystal and MEMS resonators and provides a general theory of high-Q oscillators that includes the nonlinear effects, based on the technique introduced in [18]. Then, the start-up time of oscillators is discussed and a literature of fast start-up techniques to kickstart high-Q oscillators is reviewed.

2.1 Introduction

The first high-Q oscillator which was a quartz crystal oscillator was invented by Walter Guyton Cady in 1921 [19]. Soon after, George Washington Pierce developed a very elegant oscillator circuit using a single vacuum tube [20, 21], that has been adapted to integrated circuits and is currently the most commonly-used crystal oscillator configuration. Since then,

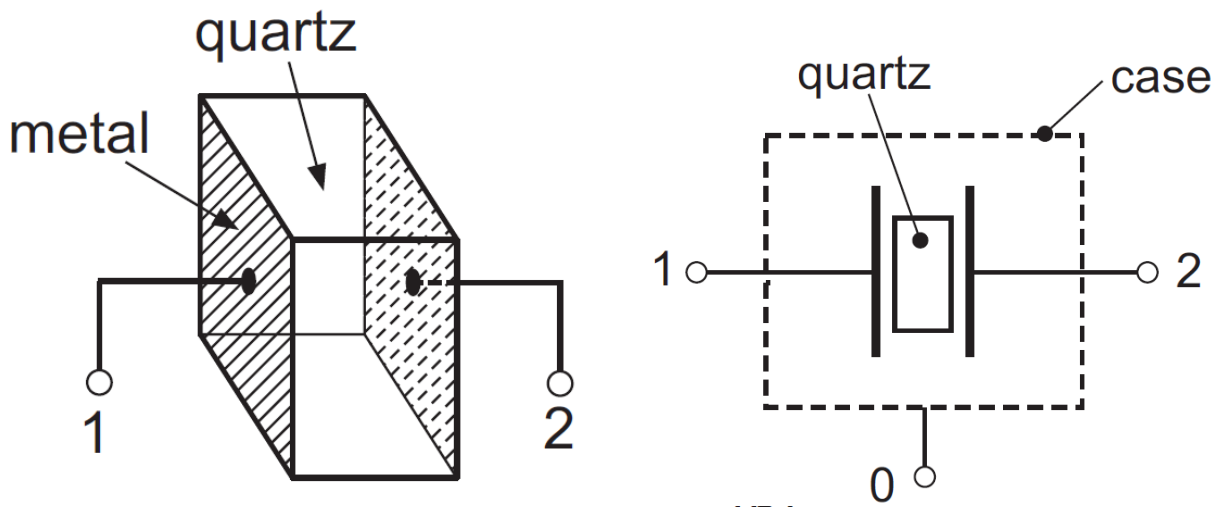

(a) (b)

Figure 2.1: Quartz crystal resonator: (a) simplified structure (b) symbol.

crystal oscillators have been one of the key components in radio-frequency (RF) transceivers and digital circuits for generating an accurate and precise frequency.

A quarts crystal or a MEMS resonator is basically a passive mechanical device driven electrically by means of an electromechanical transducer. An oscillator is built by combining it with an electronic circuit that provides the necessary energy of oscillation and compensates the losses. The frequency of oscillation should be defined by the precise resonant frequency of the resonator, with a minimum influence of the circuit. This is made easier by the enormous quality (Q-) factor of the crystal/MEMS resonator that is much larger than that of a standard electrical resonator [22]. As illustrated by Fig. 2.1, a quartz resonator is essentially a capacitor, the dielectric of which is silicon dioxide (SiO_2) that exhibits piezoelectric properties. Therefore, a part of the electrical energy stored in the capacitor is converted to mechanical energy.

In addition to its piezoelectric properties, quartz has the advantage of being an excellent mechanical material, with very small internal friction. It has therefore a very high intrinsic quality factor, of the order of 10^6.

The resonant frequency depends on the shape and the dimensions of the piece of quartz. Possible frequencies range from 1KHz for large cantilever resonators to hundreds of MHz for very thin thickness-mode resonators [23].

Modern etching techniques, developed by the microelectronics industry, made the fabrication of very small microMicro-electro-mechanical (MEMS) resonator possible. MEMS resonators can be made of polysilicon glass, of aluminum, or of silicon itself. Therefore, they are compatible with integrated circuits while exhibit a very high quality factor. However, these materials are not piezoelectric, hence the resonator must be combined with an electromechanical transducer. The transducer can be either a layer of piezoelectric material deposited on the resonator, or an electrostatic transducer. Electrostatic actuation mechanism is easy to integrate and implement with CMOS technology. However, a high actuation voltage is needed.

2.2 Equivalent Circuit

The equivalent electrical circuit of a high-Q resonator, whether a quartz crystal or a MEMS, is shown in Fig. 2.2(a). Unlike simple LC oscillators, mechanical resonators always possess several resonance frequencies, corresponding to different possible modes of oscillation (eigenmodes). Each possible mode of oscillation i of the resonator corresponds to a motional impedance $Z_{m,i}$ formed by the series resonant circuit $R_{m,i}$, $C_{m,i}$, and $L_{m,i}$. The motional inductance L_m is proportional to the mass of the mechanical resonator. The motional capacitance C_m is proportional to the inverse of its stiffness. The motional resistance R_m represents the mechanical losses. Once oscillation has taken place at one mode, the other modes are not excited and thus the other branches in the equivalent circuit can be ignored as shown in Fig. 2.2(b).

Figure 2.3 plots the magnitude and phase of the impedance of a high-Q resonator around its fundamental mode. The equivalent circuit of Fig. 2.2(b) has two resonance frequencies: series resonance frequency ω_m and parallel (anti-resonance) frequency ω_p. The series

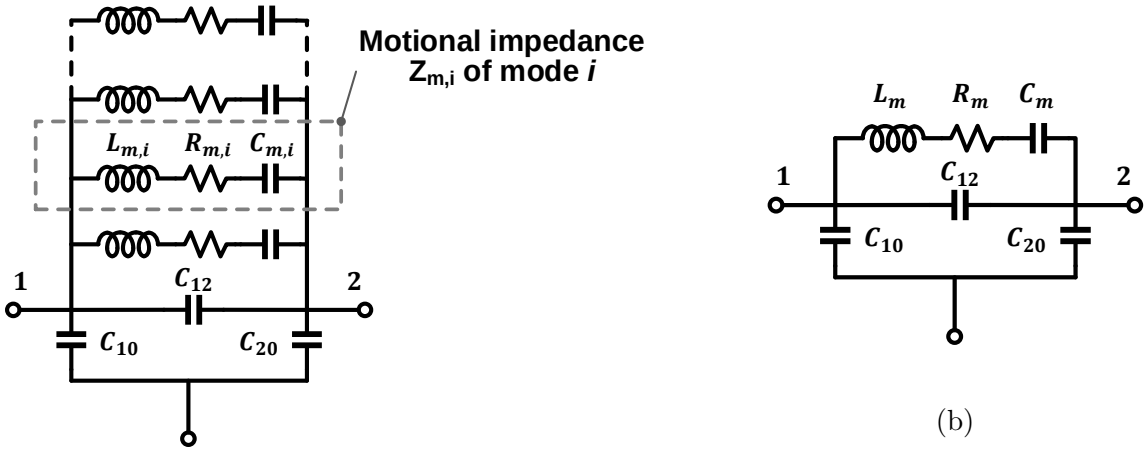

(a) (b)

Figure 2.2: Equivalent circuit of a high-Q resonator: (a) with all possible modes (b) with a single mode of interest.

resonance frequency is given by

$$\omega_m = \frac{1}{\sqrt{L_m C_m}} \tag{2.1}$$

At series resonance, the crystal motional branch is low impedance, with an equivalent series resistance (ESR) of R_m. The parallel resonance frequency is given by

$$\omega_p = \frac{1}{\sqrt{L_m C_m}} \cdot \sqrt{1 + \frac{C_m}{C_O}} \tag{2.2}$$

$$\simeq \omega_m \cdot \left(1 + \frac{C_m}{2C_O}\right)$$

where $C_O = C_{12} + \frac{C_{10}C_{20}}{C_{10}+C_{20}}$ is called the static capacitance. The impedance of the resonator at the parallel resonance is

$$R_p = \left(\frac{QC_m}{C_O}\right)^2 \cdot R_m \tag{2.3}$$

$$= M^2 \cdot R_m$$

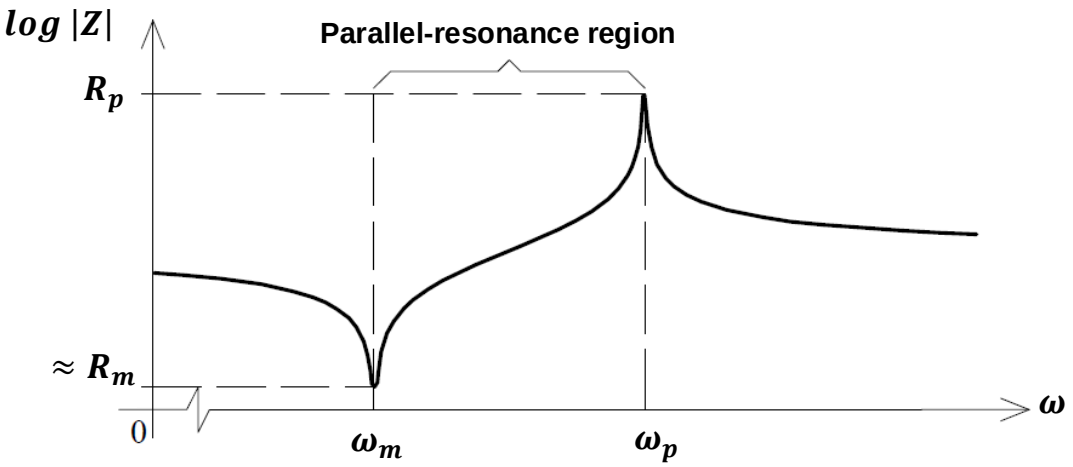

(a)

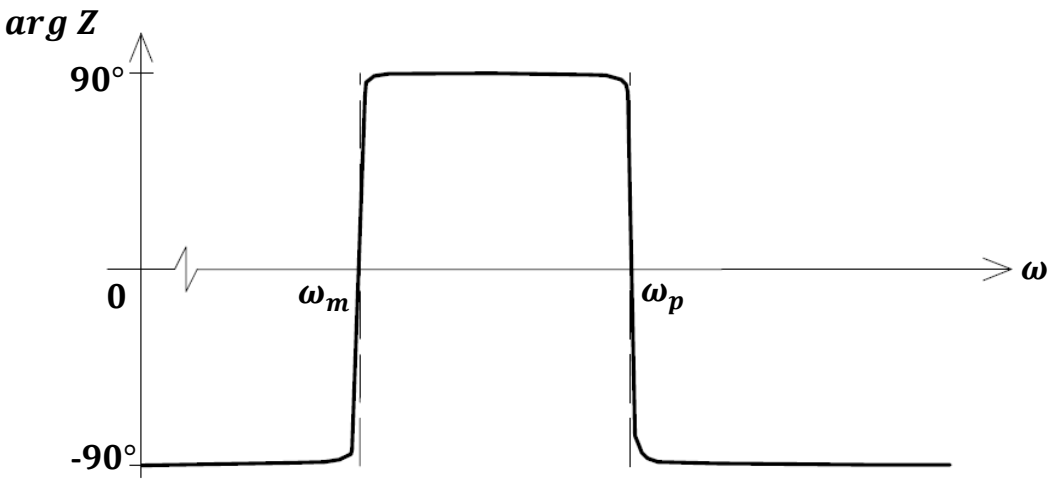

(b)

Figure 2.3: (a) Magnitude and (b) phase of a high-Q resonator over frequency.

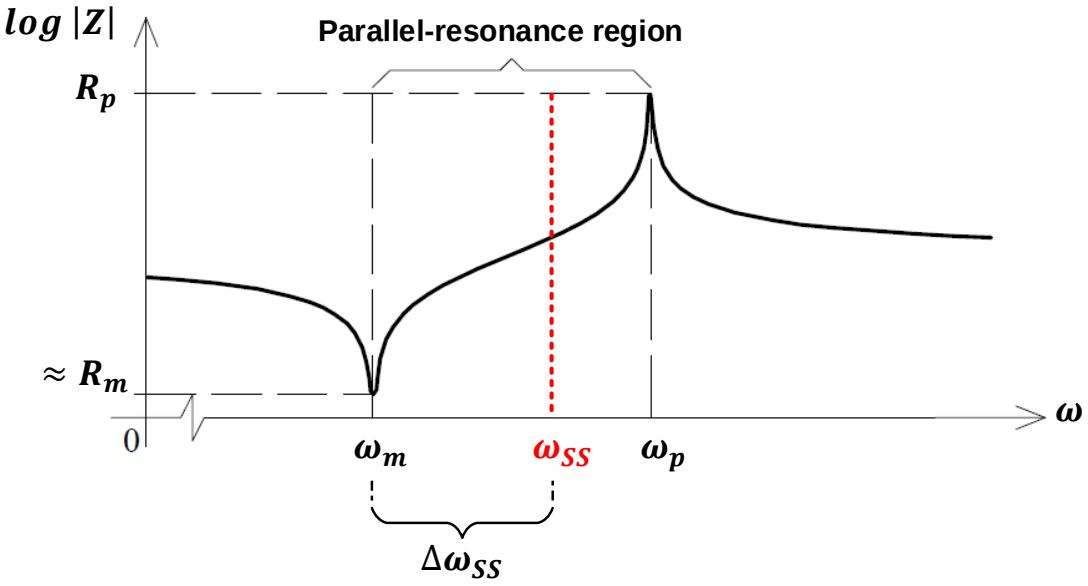

Figure 2.4: Parallel-resonance oscillation at ω_{SS}.

where $M = \frac{QC_m}{C_O}$ is called the resonator figure of merit and is the maximum possible ratio of currents through Zm and the static capacitor C_O [23].

The relative frequency separation between the series and parallel resonance frequencies, i.e., $\frac{\omega_p - \omega_m}{\omega_m}$, is called the frequency pulling and is given by

$$p = \frac{\omega_p - \omega_m}{\omega_m} = \omega_m \cdot \left(\frac{C_m}{2C_O}\right) \tag{2.4}$$

Since $C_m/C_O \ll 1$, the frequency pulling, p, is very small, typically <0.3%. Within this frequency range, called the parallel-resonance region, the motional branch of Fig. 2.2(b) is equivalent to an effective inductor that resonates with the external capacitance to produce steady-state oscillation at frequency ω_{SS}, where $\omega_m < \omega_{SS} < \omega_p$ as shown in Fig. 2.4.

The quality factor of the resonator is given by

$$Q = \frac{1}{R_m C_m \omega_m} = \frac{\omega_m L_m}{R_m} = \frac{1}{R_m} \cdot \sqrt{\frac{L_m}{C_m}} \tag{2.5}$$

The Q-factor of crystal/MEMS resonators is very large, typically ranging from 10^4 to 10^6. This high Q-factor is the main contributor to the low phase noise and jitter of the oscillators incorporating quartz crystal or MEMS. However, as will be discussed later, the high Q-factor

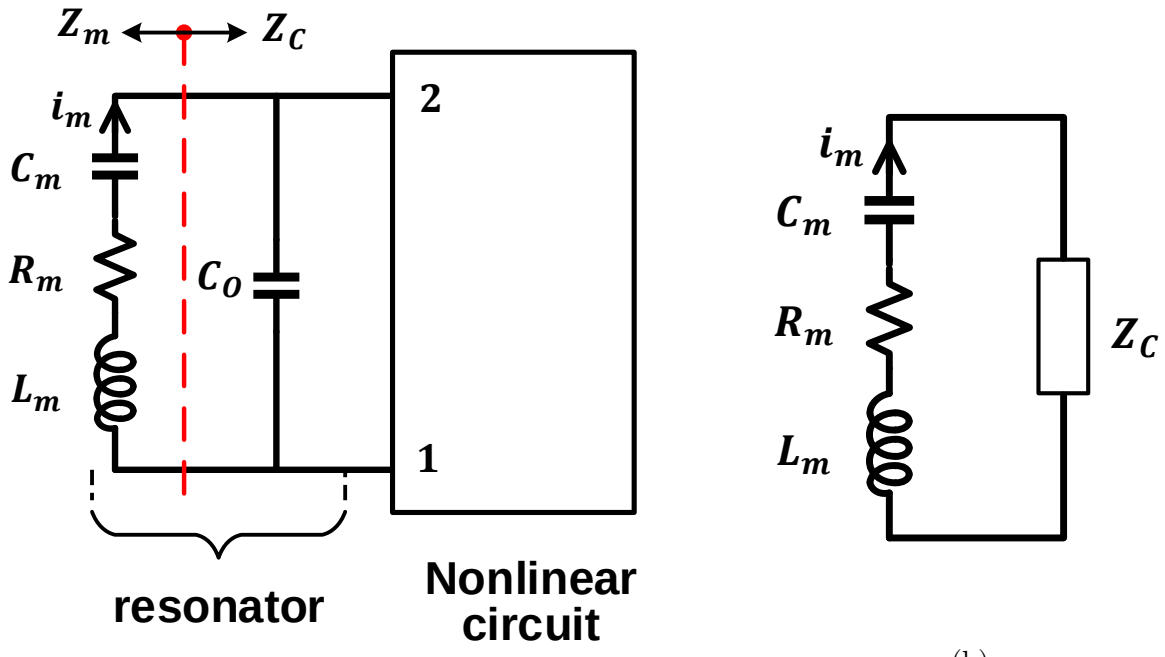

Figure 2.5: General form of an oscillator: (a) combination of the resonator with a nonlinear circuit (b) splitting into motional impedance Z_m and circuit impedance Z_C.

imposes a very long start-up time on oscillators. The long start-up time limits the power saving capability of duty-cycled systems.

2.3 General Form of a High-Q Oscillator

In order to compensate the loss of the resonator and sustain the oscillation, the resonator must be combined with an active circuit to form a full oscillator, as illustrated by Fig. 2.5(a). It is important to point out that the active circuit has to have some amount of nonlinearity to precisely compensate for the loss of the resonator and limit the amplitude of oscillation.

Due to the high Q-factor of the resonator, the motional current i_m flowing through the motional impedance Z_m is always sinusoidal. Therefore, the best way to analyze the behavior of the oscillator, while including the necessary nonlinearity of the active circuit, is to split it

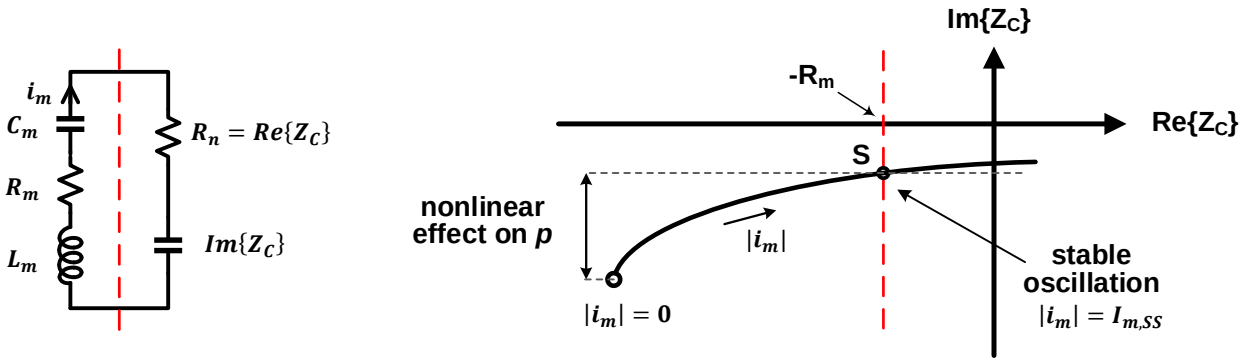

Figure 2.6: Nonlinear oscillation mechanism: (a) equivalent circuit of the oscillator (b) intersection of the locus of $Z_C(|i_m|)$ with that of $-Z_m$.

conceptually into the motional impedance Z_m and the active circuit's nonlinear impedance Z_C that also includes the static capacitor C_O of the resonator, as shown in Fig. 2.5(b) [18]. The nonlinear impedance Z_C is a function of the oscillation amplitude $|i_m|$, i.e., $Z_C(|i_m|)$.

Figure 2.6 illustrates the evolution of oscillation [23]. Initially, the motional current flowing in the resonator, i_m, is very small, resulting in a linear amplification of the signal by the active circuit since the net resistance is negative. It can be readily shown that the amplitude of any existing oscillation grows exponentially with the following time constant,

$$\tau = \frac{-2L_m}{R_m + R_n} = -\frac{2Q}{\omega_m} \cdot \frac{R_m}{R_m + R_n} \tag{2.6}$$

As i_m grows, at some point, the nonlinearity of the active circuit kicks in and reduces the its impedance, i.e., Z_C. The locus of the impedance Z_C as a function of the amplitude of the motional current i_m is sketched in Fig. 2.6(b). Stable oscillation occurs at point **S**, where the amount of energy injected by the active circuit is exactly equal to the loss of the resonator. Hence, at stable oscillation, the following critical conditions are met:

$$R_n = \mathrm{Re}\{Z_C\} = -R_m \tag{2.7}$$

$$\mathrm{Im}\{Z_C\} = -\,\mathrm{Im}\{Z_m\} \tag{2.8}$$

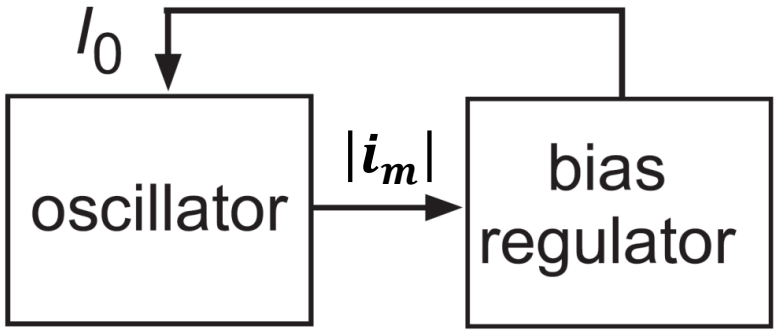

Figure 2.7: Amplitude control loop by bias regulator.

At steady state, i.e., point **S** in Fig. 2.6(b), the stable amplitude of the motional current i_m reaches its steady-state value $I_{m,SS}$.

It is important to note that because of the active circuit nonlinearity, (2.7) and (2.8) are functions of the circuit nonlinearity. Since nonlinearity varies over process, voltage, and temperature (PVT), the oscillation amplitude and frequency becomes functions of PVT. The linear impedance Z_C, at very small i_m, depends on the bias current I_O applied to the circuit. Nonlinear effects can be minimized by reducing this current when the oscillation amplitude increases. Figure 2.7 illustrates a conceptual block diagram of a bias regulator loop. With such an "amplitude control loop", stable oscillation occurs very close to the critical condition and the oscillation amplitude and frequency will be less sensitive to PVT variations.

Since the motional current $I_{m,SS}$ represents the mechanical velocity and L_m represents the equivalent mass moving at this velocity, the mechanical energy of oscillation is

$$E_m = \frac{L_m I_{m,SS}^2}{2} = \frac{Q R_m I_{m,SS}^2}{2\omega} \tag{2.9}$$

Since this energy is proportional to the square of the amplitude, it should be limited to avoid destruction and limit nonlinear effects and aging. However, it should be much larger than the noise energy in order to limit the phase noise [23].

The motional current is sinusoidal, with an RMS value of $I_{m,SS}/\sqrt{2}$. The power dissipated

in the resonator is thus given by

$$P_m = \frac{R_m I_{m,SS}^2}{2} = \frac{I_{m,SS}^2}{2\omega Q C_m} \tag{2.10}$$

This power must be provided by the sustaining circuit shown in Fig. 2.5(a) in order to maintain the amplitude of oscillation. Otherwise, at each period of oscillation $^{2\pi}/_{\omega}$, the energy would be reduced by

$$\Delta E_m = \frac{2\pi P_m}{\omega} = \frac{2\pi}{Q} \cdot E_m \tag{2.11}$$

2.4 Start-Up Behavior of High-Q Oscillators

As already established in Fig. 2.6(b), any existing initial motional current of amplitude $|I_{m0}|$ will grow exponentially according to

$$|i_m| = |I_{m0}| \cdot \mathrm{e}^{t/\tau} \tag{2.12}$$

where τ is the time constant of the circuit given by (2.6). However, as already pointed out, any oscillator must be nonlinear to keep a certain level of oscillation amplitude and the nonlinearity is usually provided by the active circuit. This nonlinearity causes a progressive reduction of the negative resistance with the increase of oscillation amplitude (Fig. 2.6(b)), which can be expressed as

$$R_n = R_{n0} \cdot \mathbb{F}(|i_m|) \tag{2.13}$$

where $\mathbb{F}(|i_m|)$ is a monotonously decreasing function with $\mathbb{F}(0) = 1$, $\mathbb{F}(I_{m,SS}) = -^{R_m}/_{R_{n0}}$, and R_n0 is the small-signal value of the negative resistance, i.e.,

$$R_{n0} = \mathrm{Re}\left\{ Z_C(|i_m| = 0) \right\} \tag{2.14}$$

As long as the motional current is small enough, the active circuit remains linear with an impedance $Z_C(|i_m| = 0)$, corresponding to a minimum time constant τ_0 given by

$$\tau_0 = \frac{-2L_m}{R_m + R_{n0}} \tag{2.15}$$

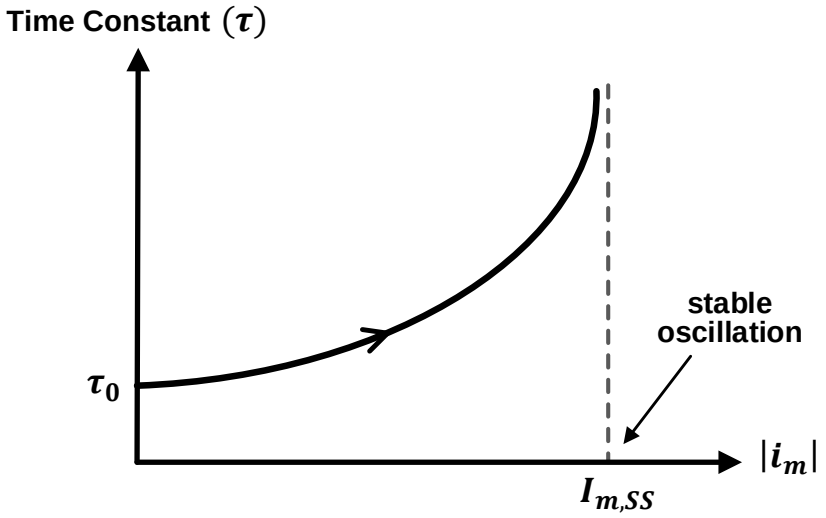

Figure 2.8: Variation of the time constant during oscillation buildup.

When nonlinearities start to appear, the amount of negative resistance starts to decrease as illustrated in Fig. 2.6(b), thereby increasing the time constant as shown in . The time constant becomes infinite at stable oscillation where the magnitude of negative resistance is exactly equal to the positive resistance according to (2.7).

By introducing the expression (2.13) in (2.6), we obtain

$$\tau = \frac{-2L_m}{R_m + R_{n0} \cdot \mathbb{F}(|i_m|)} \tag{2.16}$$

which should be infinite for $|i_m| = I_{m,SS}$ (stable oscillation). Hence, by using (2.15),

$$\tau = \tau_0 \cdot \frac{1 - \mathbb{F}(I_{m,SS})}{\mathbb{F}(I_{m,SS}) - \mathbb{F}(|i_m|)} \tag{2.17}$$

Introducing this result in (2.12) and integration gives the time T_{ab} needed for the oscillation to grow from an arbitrary point **a** in Fig. 2.6(b), corresponding to a current amplitude $|i_{m,a}|$, to another point **b**, corresponding to a current amplitude $|i_{m,b}|$:

$$T_{ab} = \tau_0 \cdot \int_{|i_{m,a}|}^{|i_{m,b}|} \frac{1}{|i_m|} \cdot \frac{1 - \mathbb{F}(I_{m,SS})}{\mathbb{F}(I_{m,SS}) - \mathbb{F}(|i_m|)} \, \mathrm{d}|i_m| \tag{2.18}$$

Start-up time is defined as the time it takes for the circuit, i.e., nonlinearity, to move the impedance Z_C from its small-signal value to the stable point **S** shown in Fig. 2.6(b).

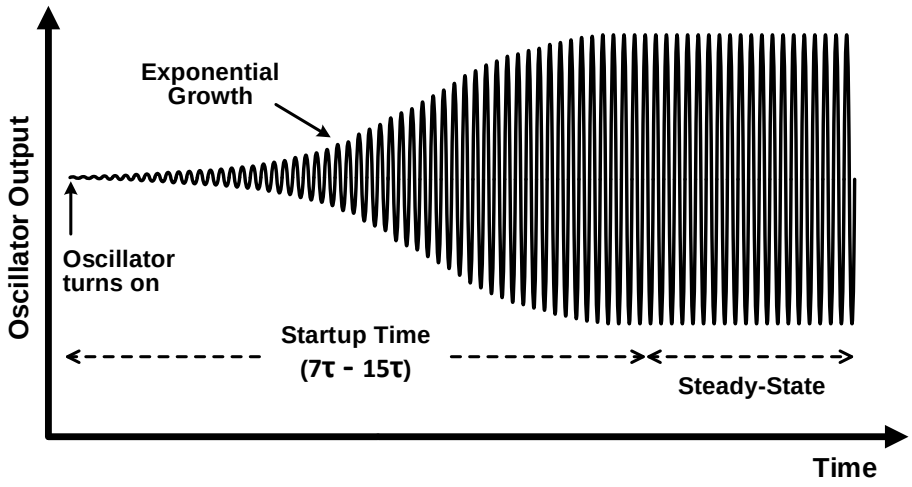

Figure 2.9: Transient response of an oscillator during start-up.

In practice, for high-Q oscillators, the start-up time to reach 90% of the stable amplitude ranges from $7\tau_0$ to $15\tau_0$ [23]. For instance, a 10MHz crystal oscillator with a Q-factor of 100,000 takes up to several milliseconds to fully turn on which is not acceptable for low-power applications. The transient response of a high-Q oscillator during start-up is shown in Fig. 2.9.

High-Q resonators, despite their suitable performance and reliability, are facing challenges in the merging energy-constrained applications such as Internet of Things (IoT) and wearable technologies. The main drawback of these resonators are their long start-up time compared to rest of the system. A long start-up time limits the rate at which a system can be duty-cycled to save power, hence it adversely impacts the battery life or performance in energy-harvesting systems.

2.5 Prior Art

Conventionally, oscillators self-start by amplifying the internally-generated noise, i.e., thermal energy kT, to a level that creates enough energy in the resonator to sustain oscillation as illustrated in Fig. 2.9. As mentioned earlier, high-Q resonators with a Q-factor in the

Table 2.1: Conventional quick start-up techniques

Method	**Start-up reduction**	**Limitations**
Using a higher frequency resonator	✓	• Higher steady-state power
Using a resonator in a larger package (low L_m)	✓	• Larger form factor
Initially increasing the g_m of the amplifier (by increasing the bias current at start-up)	✓	• Limited improvement • PVT-sensitive start-up time
Initially decreasing the capacitive load C_L	✓✓	• Limited improvement • PVT-sensitive start-up time • Long frequency settling
Pre-energizing the resonator (by an injection oscillator at start-up)	✓✓✓	• Sensitive to injection frequency • Long transient time

order of 10^4-10^6 have an extremely long start-up time according to (2.6), which is too long for many low-power applications that rely on duty-cycling the system to achieve ultra-low power consumption. Furthermore, since the start-up relies on amplifying the circuit noise, the start-up time becomes very unpredictable and varies over PVT. To reduce the start-up time of high-Q oscillators, several quick start-up techniques have been reported [24–32]. A summary of these techniques along with their limitations is listed in Table 2.1.

Initially increasing the transconductance (g_m) of the active circuit during start-up, as depicted in Fig. 2.10(a), increases the small-signal negative resistance, and hence reduces the time constant of the circuit according to (2.6). However, since there is usually a linear relationship between the g_m and the time constant of most oscillators, e.g., the commonly-used Pierce oscillator, the amount of achieved improvement is very limited. Furthermore, the start-up time is quite random as it still relies on amplifying the circuit noise.

The second approach to reduce the start-up time is to initially reduce the capacitive

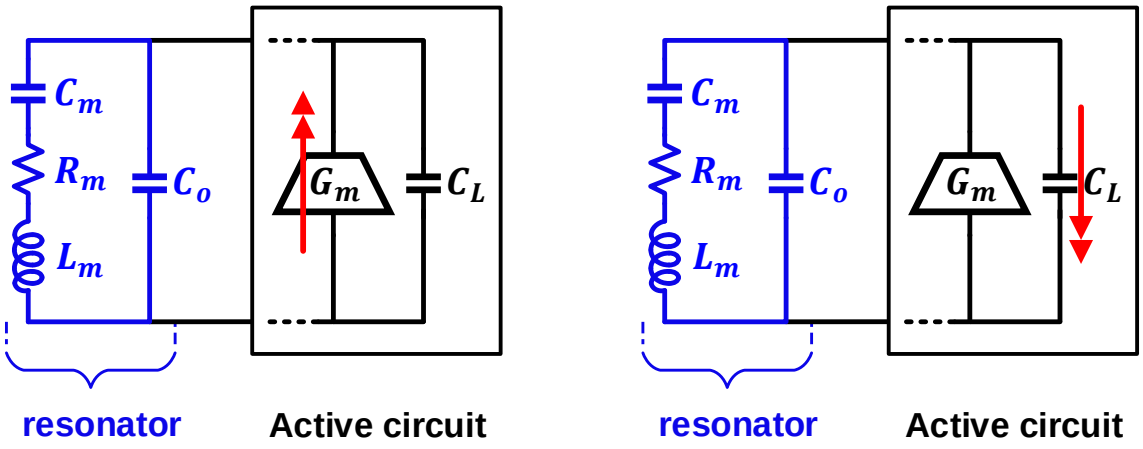

(a) (b)

Figure 2.10: Traditional quick start-up techniques by increasing the negative resistance: (a) by increasing the transconductance of the active circuit (b) by initially decreasing the capacitive load.

load of the resonator, and add the required load capacitors later on at steady state. This technique is illustrated in Fig. 2.10(b). However, the amount of improvement in this work is also limited as the amount of capacitive reduction is limited to the parasitic capacitances of the circuit and the stray capacitance of the PCB and the I/O pads. Furthermore, as the load capacitors are added later on, the oscillation frequency is disturbed and the oscillator ends up having a long frequency settling. Moreover, the start-up still depends on the initial amount of circuit noise and hence it varies over PVT.

The most effective attempt in prior art to kick-start an oscillator is by pre-energizing the resonator by means of another source of energy such as a ring oscillator or an RC oscillator as shown in Fig. 2.11. This way, the oscillation amplitude, instead of starting with a small noise level, starts with a much bigger amplitude and it can reach steady state much faster.

Despite its effectiveness, there are two main issues with the pre-energization technique that need to be addressed. The first major problem is that pre-energization is very sensitive to the frequency of the injection signal, i.e., ω_{inj} in Fig. 2.11. This stems from the fact

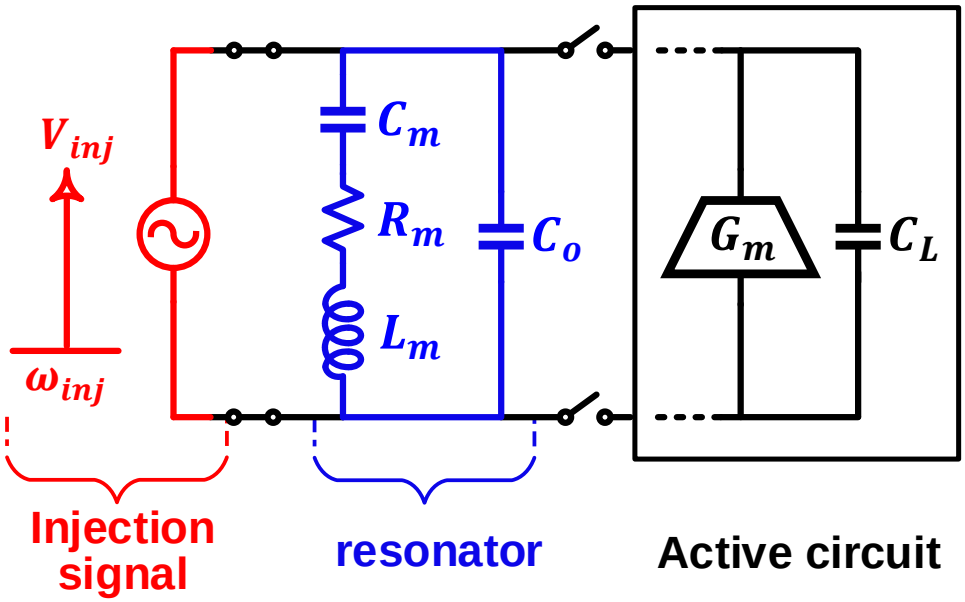

Figure 2.11: Quick start-up of a high-Q oscillator by pre-energizing the resonator.

that the resonator has a very high quality factor. As a result, in frequency domain, the resonator has a very sharp characteristic with a very narrow bandwidth. Consequently, the injection frequency has to be exactly equal to the natural resonance frequency of the high-Q resonator in order to energize it. Otherwise, even a small offset in frequency would prevent the resonator from getting energized.

The second issue of pre-energization is that there is usually a long transient time after the injection signal is disconnected, which directly adds up to the start-up time. This is because that with even perfectly-matched injection and resonance frequencies, the amount of energy built up into the resonator during pre-energization might be very small or very large. Hence, after the injection source is disconnected, the active circuit sluggishly attempts to adjust the energy level to its steady-state value, which increases the start-up time.

In the next chapter, the pre-energization technique and its challenges are thoroughly reviewed and a novel "precisely-timed energy injection" technique is proposed that addresses both of the mentioned challenges and drastically reduces the start-up time to only about 100 number of oscillation cycles.

CHAPTER 3

Precisely-Timed Energy Injection for Fast Start-Up of High-Q Oscillators

3.1 Introduction

Aggressively duty-cycling the operation of electronic systems between ON and OFF states is an effective way of reducing the power consumption in ultra-low-power systems such as Internet-of-Things (IoT) and biomedical implantable or wearable devices [33–37]. However, the rate of duty-cycling, and hence the amount of power saving, is constrained by the start-up time of the system, which itself is limited by the long start-up time of its reference oscillator. Crystal/MEMS resonators are commonly used as the reference oscillators in electronic systems. However, their extremely high quality factor ($Q \sim 100,000$) makes them very slow during start-up. For instance, a 10MHz crystal oscillator, with reasonable power consumption, takes several milliseconds to turn on and settle to within 10ppm of its final frequency [26, 27, 38–41]. In contrast, the start-up time of other circuit blocks such as low-dropout (LDO) regulators and phase-locked-loops (PLL) is usually less than $10\mu s$ [42].

Consider the generic feedback oscillator shown in Fig. 3.1(a)[1]. It has been shown (using a linear model, [43]) that the start-up time of an oscillator with an oscillation frequency of ω_{SS}, is

$$T_{start-up} \propto \frac{Q}{\omega_{SS}}.\left|\frac{1}{1+R_n/R_m}\right|.\ln(\frac{1}{i_m(0)}) \tag{3.1}$$

where R_m and R_n are the resonator's motional resistance and the negative resistance pre-

[1]Here, the resonator is modeled by its equivalent series RLC network, which is a valid model for most resonators such as crystals and MEMS.

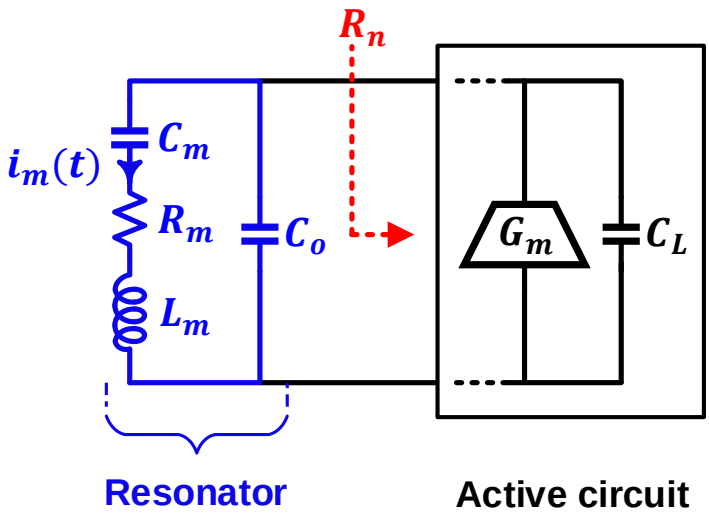

(a)

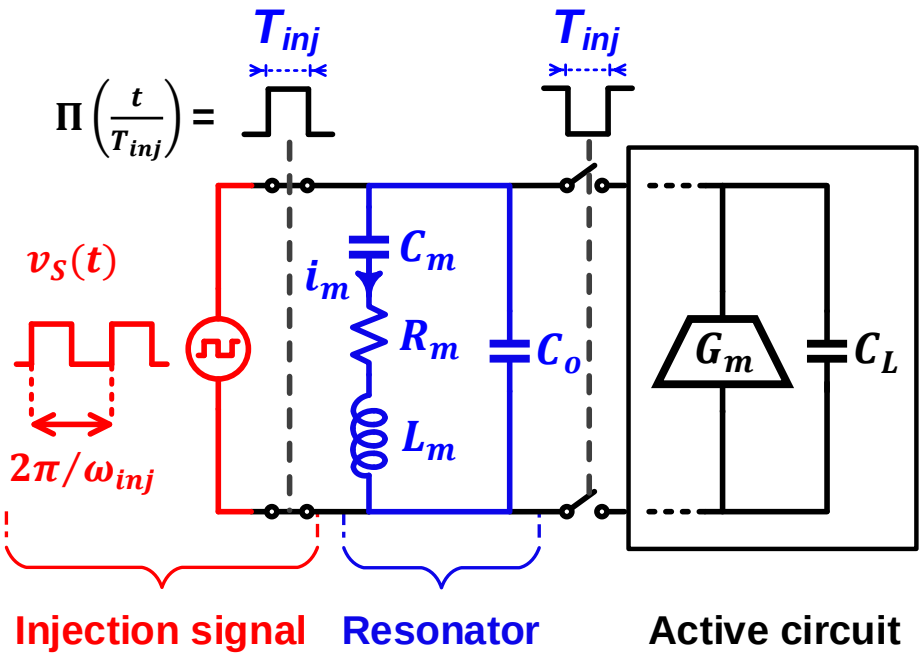

(b)

Figure 3.1: (a) General form of an oscillator (b) start-up time improvement through "pre-energization" of the resonator.

sented by the active circuitry, respectively, and $i_m(0)$ is the initial value of the current flowing into the motional branch of the resonator. It is evident that low-frequency, high-Q oscillators take a very long time to get started. Conventional enhanced start-up techniques have mostly focused on increasing the magnitude of R_n in order to quickly start the oscillator. This is done by either increasing the amplifier's transconductance [25, 26, 29, 44] or decreasing the capacitive loading of the resonator [31, 45, 46]. Nevertheless, both techniques achieve limited improvements. This is because the time-constant only linearly scales with the transconductance and the amount of capacitor reduction is limited to the parasitics and stray capacitance of the printed circuit board (PCB). Besides, both techniques rely solely on amplifying circuit noise making the start-up time sensitive to process, voltage, and temperature (PVT) variations - undesirable for precise duty cycle control.

"Pre-energization" wherein a low-Q, integrated "injection" oscillator dumps a surge of energy into the resonator prior to the aforementioned feedback-based start-up, as shown in Fig. 3.1(b), is emerging as an effective way to speed up a high-Q oscillator [28, 47, 48]. Since oscillation starts with a much bigger amplitude than circuit noise, it can potentially reach steady-state in a shorter amount of time. The integrated "injection" oscillator, e.g., a ring or relaxation oscillator, itself starts up very quickly owing to its low-Q factor. However, there are two major challenges associated with pre-energization: (1) there is usually a long transient time after the injection oscillator is disconnected, and (2) start-up time is very sensitive to the mismatch between the injection frequency, ω_{inj}, and the resonator's resonance frequency, ω_m. Since integrated ring and relaxation oscillators exhibit large sensitivity to PVT variations, researchers have resorted to calibration [28, 48], injection frequency chirping [29], or dithering [30] the injection frequency around the resonance frequency with limited success. These challenges of pre-energization is discussed in detail in Section 3.2.

In this chapter, we present a technique that employs conventional single-frequency pre-energization, but only for a narrow, precisely-controlled injection duration, $T_{inj,opt.}$ [49, 50]. This technique reduces the start-up time by 15x compared to the best case in prior art. Furthermore, the achieved start-up time is very predictable, and its sensitivity to ω_{inj} is reduced to the extent that simple, temperature-compensated integrated oscillators can be

used as the injection signal.

This chapter elaborates on the proposed "precisely-timed energy injection" technique, describing the technique and important circuit design aspects that reduces it to practice, especially over PVT corners. In addition, a new analysis that quantifies the technique's reduced sensitivity to the injection frequency mismatch and other circuit errors is described. Section 3.3 explains the main concept and an analysis of the "precisely-timed energy injection" technique. Section 3.4 quantifies the impacts of the injection frequency and duration errors on the start-up time. Section 3.5 details the implemented circuit, and Section 3.6 describes detailed measurement results.

3.2 Pre-energization: Preview and Challenges

The simplified schematic shown in Fig. 3.1(b) is a general representation of pre-energization in prior art: the resonator is driven open-loop by a voltage source, $v_s(t)$, for a finite but arbitrary duration, T_{inj}. In most cases, $v_s(t)$ is a square-wave of frequency ω_{inj}.

The transient response of a (second-order) high-Q resonator, when driven by a square- (or sine-) wave injection oscillator, is plotted in Fig. 3.2. So, during pre-energization, the envelope of the motional current, $i_{m,env}(t)$, follows an under-damped response and reaches $i_{m,env}(T_{inj})$ at the end of the injection period, i.e., at $t = T_{inj}$. Subsequently, the oscillator settles, slowly, starting from $i_{m,env}(T_{inj})$ till its steady-state value, $I_{m,SS}$, is reached, as illustrated in Fig. 3.3 for different values of T_{inj}.

This presents two significant problems. First, the start-up time is minimized only if the energy deposited in the resonator during pre-energization is equal to the energy under steady-state oscillation, i.e., $i_{m,env}(T_{inj}) = I_{m,SS}$, as shown in Fig. 3.3(b). Otherwise, as is evident from Fig. 3.3(a), the oscillator will have a long transient settling upon disconnecting the injection signal to adjust the energy level. This slow transient settling results in a long start-up time, thereby limiting the benefits of pre-energization. Furthermore, $i_{m,env}(T_{inj})$, and hence the settling time, can vary significantly over PVT corners.

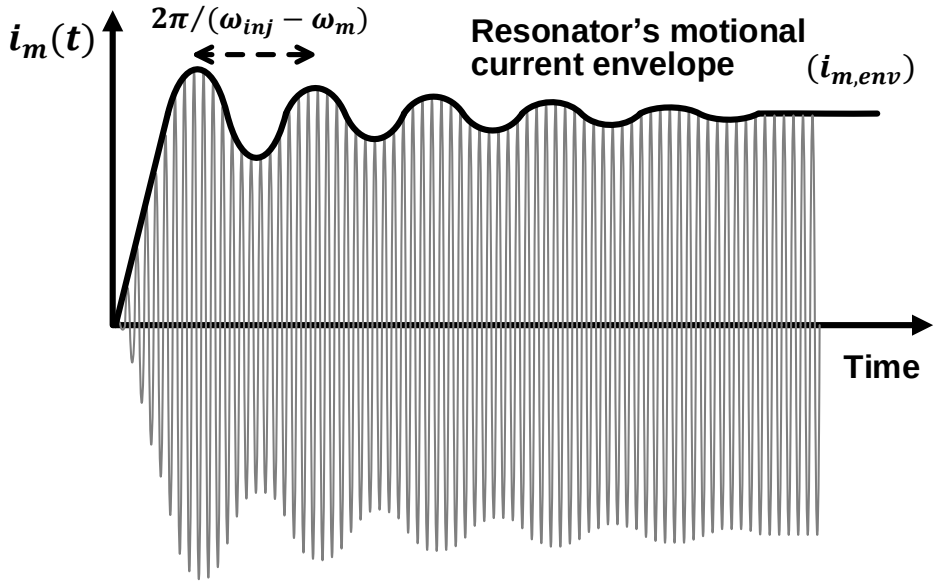

Figure 3.2: Transient response of the motional current of a high-Q resonator driven by a square-wave/sinusoidal injection signal.

Secondly, Owing to the high Q of the resonator (typically 100K-1M), unless ω_{inj} is within about $\pm$500ppm of ω_m, the resonator rejects much of the injected energy rendering the technique ineffective. As a result, the start-up time is very sensitive to the frequency mismatch between the injection frequency, ω_{inj}, and the resonator's resonance frequency, ω_m. Calibration of the injection oscillator [28,48] reduces static frequency mismatches, but even the best temperature-compensated integrated oscillators exhibit more than $\pm 5,000$ppm frequency mismatch over PVT variations [1,51–55]. Injection frequency chirping [29] and dithering [30] around ω_m, as shown in Fig. 3.4, have been employed with the hope that ω_{inj} approaches ω_m at least for a small duration during the pre-energizaion period. However, the amount of energy dumped into the resonator at the end of the injection period is still very small resulting in a long and PVT-variant settling transient.

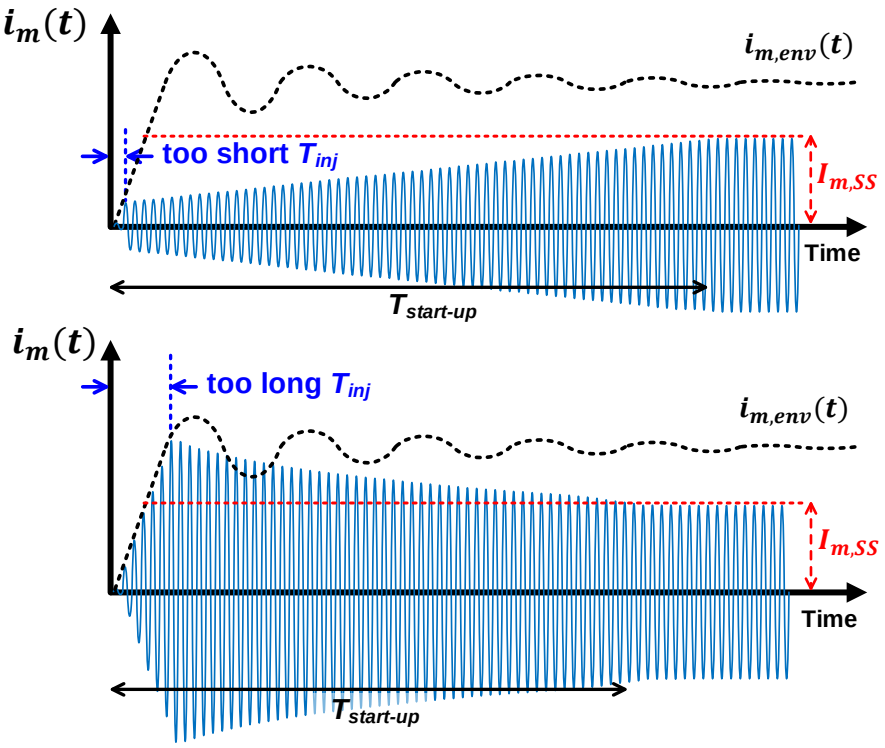

(a)

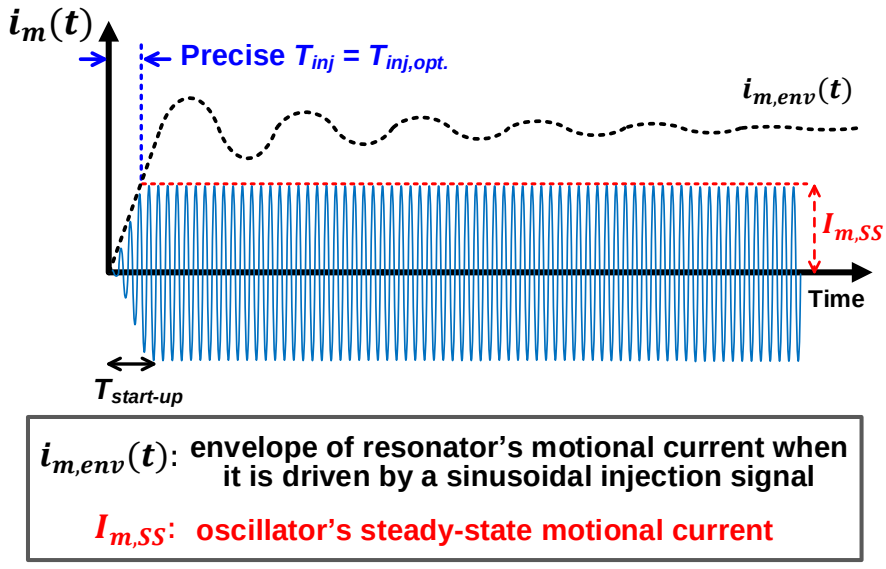

(b)

Figure 3.3: Impact of injection duration on the start-up time for three different cases of (a) short, long, and (b) optimum injection durations.

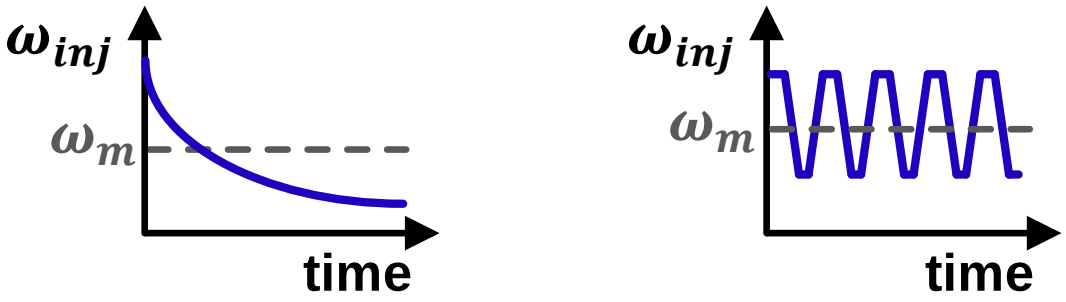

(a) (b)

Figure 3.4: Prior solutions to overcome the frequency mismatch problem: (a) chirp injection (b) dithered injection.

3.3 Precisely-Timed Energy Injection

3.3.1 Concept

The proposed technique is based on the fundamental realization that *the amount of energy injected into the resonator is determined not just by the injection frequency, ω_{inj}, but also, just as significantly, by the duration of injection, T_{inj}* [49, 50]. The technique simply terminates pre-energization precisely at the right time, $T_{inj} = T_{inj,opt.}$, such that the energy built up in the resonator is equal to its value under steady-state closed-loop oscillation condition, i.e., when $i_{m,env}(T_{inj,opt.}) = I_{m,SS}$. As shown in Fig. 3.3(b), ideally there will be no settling transient upon disengagement of the injection oscillator, thereby minimizing the start-up time. Section 3.3.2 calculates the optimal injection duration, $T_{inj,opt.}$, while Section 3.3.3 describes a simple technique to make $T_{inj,opt.}$ a PVT-invariant constant that can be set without *a priori* knowledge of $I_{m,SS}$.

It is important to note that the optimal injection duration, $T_{inj,opt.}$, marks the first time when the motional current's envelope reaches the target value, $I_{m,SS}$, during pre-energization. As shown later, this makes the start-up time a very small value, e.g., just ∼100 number of

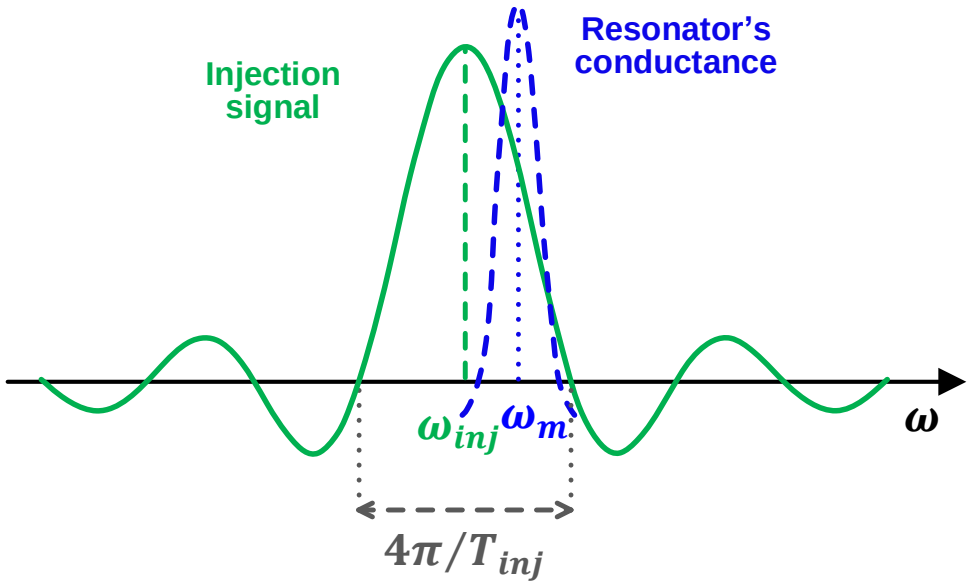

(a)

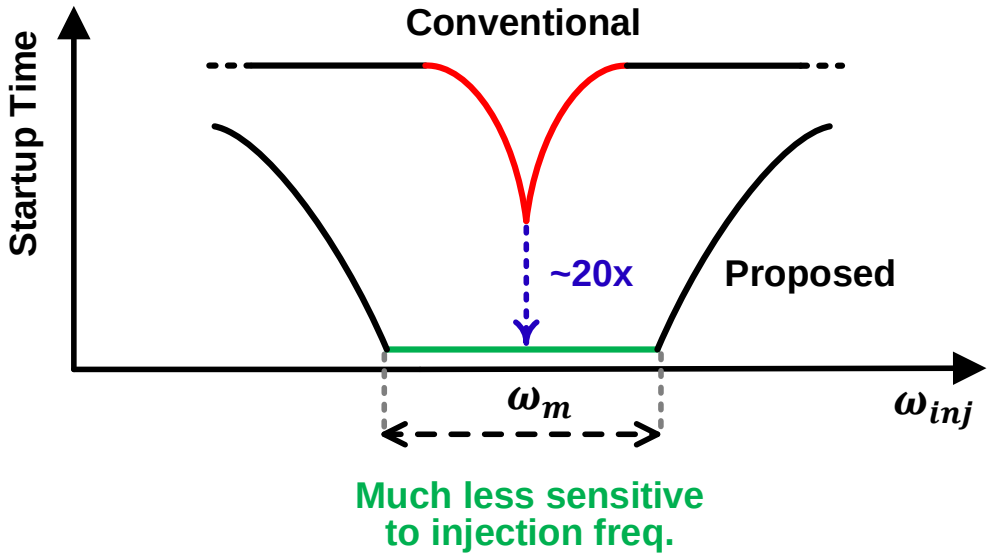

(b)

Figure 3.5: Sensitivity of the proposed precisely-timed energy injection to the variations in the injection frequency (a) in frequency domain, the injection signal is a relatively wideband sinc function (b) start-up time of the proposed solution is much less sensitive to the frequency mismatch as opposed to the conventional case.

cycles for the different measured cases in the demonstrated prototype (see Section 3.6). More importantly, note that single-frequency pre-energization for such a short duration, $T_{inj,opt.}$, amounts to driving the narrow-band resonator in open-loop with a very wide bandwidth sinc-shaped[2] signal centered at ω_{inj}, with a main lobe width of $4\pi/T_{inj}$, as shown in Fig. 3.5(a). The wide main lobe ensures that the resonator is sufficiently energized even for a large mismatch between ω_{inj} and ω_m, unlike conventional pre-energization. Consequently, the proposed quick start-up technique is much less sensitive to the injection frequency errors than prior art, as depicted in Fig. 3.5(b). Section 3.4 provides a quantitative analysis of this effect. It is important to note that in the case of conventional pre-energization (arbitrary T_{inj}), even with perfectly-matched injection and resonance frequencies, the oscillator still might take a long time to get started due to under/over energization of the resonator as shown in Fig. 3.3(a). This explains the lower start-up time of the proposed solution compared to the conventional technique in Fig. 3.5(b).

Another by-product of using a small injection duration is the low start-up energy consumption as all the start-up auxiliary circuitry is ON only for the short duration of $T_{inj,opt.}$. This is verified by our measurement results in Section 3.6.

In summary, as shown in Fig. 3.3(b) and 3.5(b), precisely timing the injection duration addresses both of the challenges in pre-energization, namely *sensitivity to injection frequency* and *long transient time*. The rest of the chapter provides an analysis to compute the optimal injection duration and how to make it invariant over PVT variations.

3.3.2 Injection Duration (T_{inj})

As Fig. 3.3(b) suggests, start-up time is minimized when

$$i_{m,env}(t = T_{inj,opt.}) = I_{m,SS} \tag{3.2}$$

To determine $i_{m,env}(t)$, consider a high-Q resonator driven by an arbitrary voltage source, $v_{inj}(t)$ as shown in Fig. 3.6. As derived in Appendix A, the envelope of the motional current

[2]Here, a sinc function is defined as $\text{sinc}(x) = \frac{\sin(x)}{x}$.

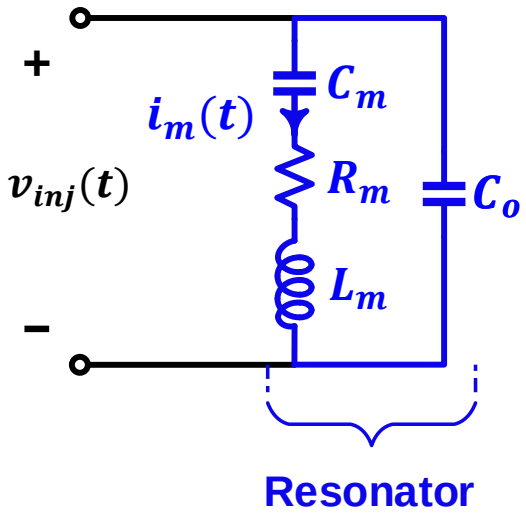

Figure 3.6: A resonator driven by an arbitrary injection signal.

is given by

$$i_{m,env}(t) = \left| V_{inj+}(j\omega_m) \right| \cdot \frac{\mathrm{e}^{-t/\tau}}{L_m} \tag{3.3}$$

where $V_{inj+}(j\omega) = V_{inj}(j\omega)$ for $\omega > 0$, but 0 otherwise, i.e., it is the positive-frequency half of the Fourier transform of $v_{inj}(t)$, and $\tau = 2Q/\omega_m$ is the time-constant of the circuit.

In case of the finite injection shown in Fig. 3.1(b), it can be shown that during pre-energization, i.e., $0 \leq t \leq T_{inj}$, $v_{inj}(t) = v_S(t) \cdot \Pi(t/T_{inj})$, where $\Pi(t)$ is a unit pulse of unit time duration. As a result, for the case of injecting a single frequency[3], i.e., $v_S(t) = V_{inj} \cdot \cos(\omega_{inj} t)$, $V_{inj+}(j\omega)$ is simply a sinc function translated in frequency to ω_{inj}. Hence, using (3.3), it can be shown that the envelope of the motional current at the end of the injection duration, T_{inj}, is

$$i_{m,env}(T_{inj}) = \frac{T_{inj} \cdot V_{inj}}{2L_m} \cdot \left| \mathrm{sinc}\left[\frac{T_{inj}}{2} \cdot \Delta\omega_{inj} \right] \right| \cdot \mathrm{e}^{-T_{inj}/\tau} \tag{3.4}$$

where $\Delta\omega_{inj} = \omega_{inj} - \omega_m$ is the mismatch between the injection and resonance frequencies.

[3]Due to the high Q factor of the resonator, considering only the first harmonic of a square-wave driving source is sufficient, where $V_{inj} = \frac{4}{\pi} \cdot V_d$, and V_d is the square-wave amplitude.

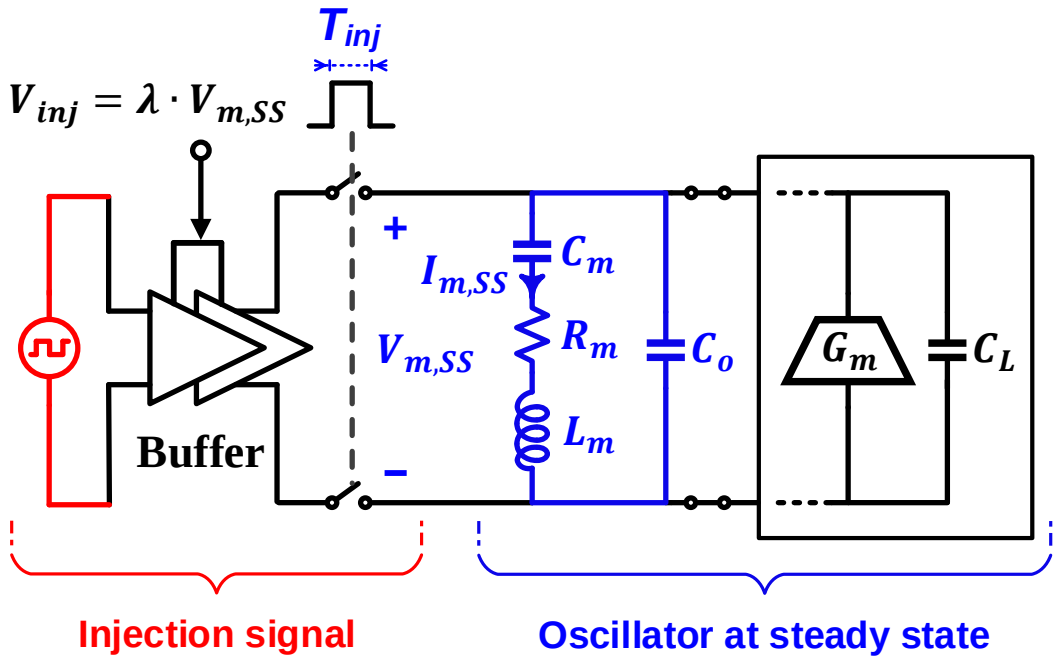

Figure 3.7: Constant, PVT-insensitive injection duration by making the injection amplitude (V_{inj}) track the steady-state oscillation amplitude ($V_{m,SS}$).

Assuming $T_{inj} \ll \tau$ and $T_{inj} \cdot |\Delta\omega_{inj}| \ll 2$, the optimum injection duration can be shown to be

$$T_{inj,opt.} = \frac{2L_m \cdot I_{m,SS}}{V_{inj}} \tag{3.5}$$

3.3.3 PVT-Invariant Injection Duration

While it is conceptually simple, realizing $T_{inj,opt.}$ in practice is problematic since $I_{m,SS}$ and V_{inj} vary over PVT, and L_m depends on the resonator's process variations. Our solution is to make V_{inj} track the steady-state amplitude across the resonator under normal oscillation conditions, $V_{m,SS}$, as illustrated in Fig. 3.7. By making $V_{inj} = \lambda \cdot V_{m,SS}$, where λ is a suitable constant, and noting that the ratio $I_{m,SS}/V_{m,SS}$ is the resonator's motional admittance,

$T_{inj,opt.}$ reduces to

$$T_{inj,opt.} = \frac{1}{\lambda \cdot \Delta\omega_{SS}} \tag{3.6}$$

Note that the chosen constant λ can be precisely implemented using a feedback amplifier. Note also that $\Delta\omega_{SS} = \omega_{SS} - \omega_m$ is the difference between the steady-state oscillation frequency, ω_{SS}, and the resonator's resonance frequency, ω_m, and it too has minimal variations thanks to the high stability of high-Q reference oscillators such as crystal and/or MEMS oscillators. Therefore, according to (3.6), $T_{inj,opt.}$ is a very predictable and constant number that can be calculated and set at design time.

It is important to note that the steady-state oscillation amplitude, $V_{m,SS}$, is not usually known before the oscillator has started up. Furthermore, $V_{m,SS}$ can vary over PVT corners. Hence, the implementation of the technique shown in Fig. 3.7 requires delicate consideration. For instance, in oscillators that peg $V_{m,SS}$ to a fixed reference (bandgap) voltage, V_{ref}, by using an amplitude regulator, then V_{inj} can be simply set using V_{ref}. In this work, we consider the popular case of the Pierce oscillator with an amplitude regulator proposed by Vittoz *et al* [18], which provides a $V_{m,SS}$ that linearly varies over temperature. Therefore, as described in Section 3.5.1, a proportional-to-absolute-temperature (PTAT) regulator can be used to set the injection amplitude, V_{inj}.

3.4 Impact of Injection Frequency and Duration Errors on Start-Up Time

This section quantifies the impact of injection frequency and timing errors on the start-up time, i.e., the impact of non-zero values of $\Delta\omega_{inj} = \omega_{inj} - \omega_m$ and $\Delta T_{inj} = T_{inj} - T_{inj,opt.}$.

Start-up time is generally defined as the time required to first reach and subsequently stay within a target frequency settling error. Since measuring real-time frequency with ppm accuracy, especially for very low start-up times, is very challenging, we quantify the start-up time in terms of a target oscillation amplitude settling error, ε.

Note that using amplitude settling behavior as a proxy for frequency settling behavior is a

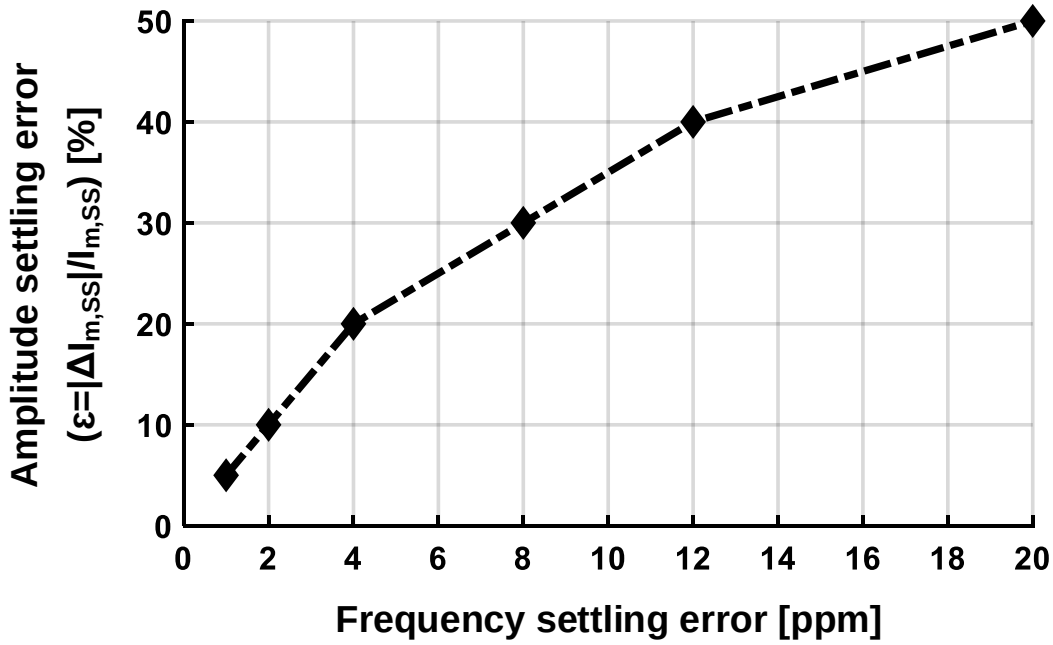

Figure 3.8: Simulation result of amplitude settling error versus frequency settling error for a 50MHz crystal oscillator.

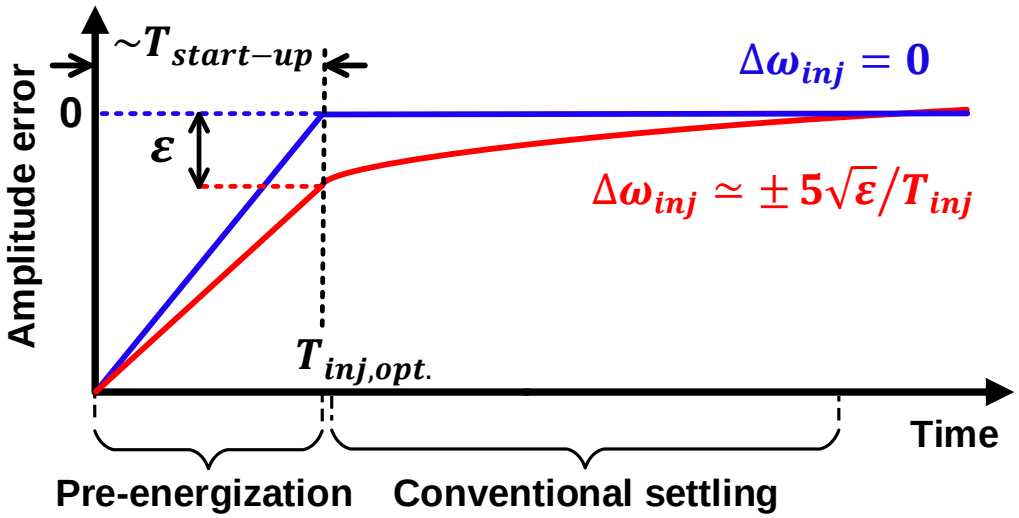

Figure 3.9: Impact of $\Delta\omega_{inj} = \omega_{inj} - \omega_m$ on amplitude settling.

common practice [29], [56]. To independently verify, we have performed thorough transistor-level circuit simulations of a typical 50 MHz crystal oscillator without and with the proposed fast start-up technique. Fig. 3.8 shows the simulated relationship between the amplitude and frequency settling errors for the fast start-up technique. The monotonic relation clearly suggests that amplitude settling is a valid proxy for frequency settling measurements. For instance, the frequency error at 90% amplitude (ε =10%) is within 2ppm, which explains why in prior art, e.g., [29] and [56], the start-up time is often measured as the time at which the oscillation amplitude is at 90% of its steady-state value.

Now, the effect of $\Delta\omega_{inj}$ and ΔT_{inj} on the start-up time can be quantified in terms of a target amplitude settling error, ε, and Fig. 3.8 can translate it to an equivalent target frequency settling error.

Fig. 3.9 depicts typical amplitude settling in the proposed fast start-up technique. Ideally, when there are no frequency or timing errors, i.e., $\Delta\omega_{inj} = 0$ and $\Delta T_{inj} = 0$, then the motional current amplitude at the end of the pre-energization period is exactly equal to its value under steady state oscillations, i.e., there is no subsequent transient and the start-up time is exactly $T_{start-up} = T_{inj,opt.}$.

However, any errors will result in an amplitude error, ε, at the end of the pre-energization period, as illustrated for the case of $\Delta\omega_{inj} \neq 0$ in the figure. Conventional oscillator settling will subsequently reduce the motional current amplitude (and frequency) errors from ε towards zero. However, a start-up time of $T_{inj,opt.}$ is guaranteed simply by ensuring that the total motional current amplitude settling error at the end of the pre-energization period is smaller than the target ε.

3.4.1 Tolerable Injection Frequency Error (TIFE)

The dependence of the motional current's envelope value at the end of the pre-energization period, $i_{m,env}(T_{inj})$, on the injection frequency error, $\Delta\omega_{inj}$, was already derived in Section 3.3.2, specifically in (3.4). This dependence is plotted in Fig. 3.10. Note that it simply follows the sinc-function shape of the Fourier transform of the injection signal. It can be

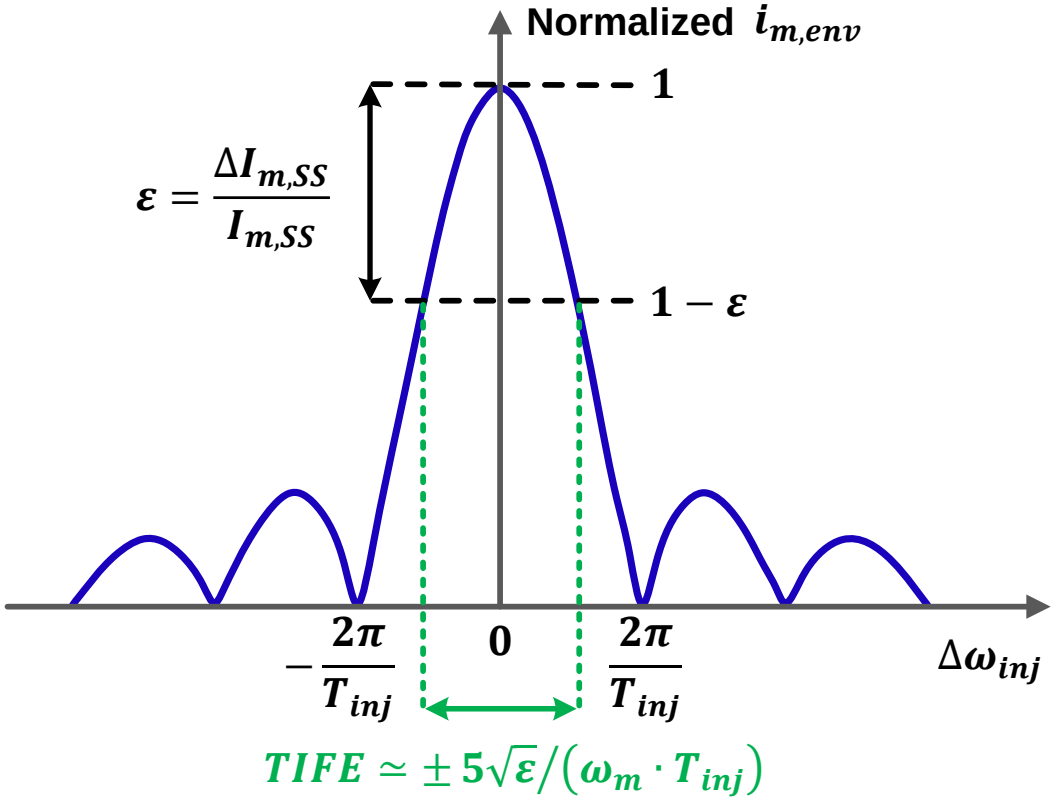

Figure 3.10: Variations in $I_{m,SS}$ as a function of frequency mismatch, $\Delta\omega_{inj} = \omega_{inj} - \omega_m$. In order to maintain an ε variation in $I_{m,SS}$, the frequency mismatch needs to be kept within $\pm 5\sqrt{\varepsilon}/T_{inj}$.

shown that the normalized motional current amplitude error is less than ε if

$$\left|\Delta\omega_{inj}\right| \leq \frac{5\sqrt{\varepsilon}}{T_{inj,opt.}}, \tag{3.7}$$

as shown in the figure. Normalized to ω_m, this represents the tolerable injection frequency error (TIFE) for which the start-up time needed to reach a target amplitude settling error, ε, remains $T_{start-up} = T_{inj,opt.}$:

$$TIFE(\epsilon) = \frac{\Delta\omega_{inj}}{\omega_m} \cong \pm 5\sqrt{\varepsilon} \cdot \lambda \cdot p \tag{3.8}$$

where $p = (\omega_{SS} - \omega_m)/\omega_m$ is the frequency pulling factor of the high-Q oscillator.

Fig. 3.11 plots the calculated TIFE as a function of both the amplitude and frequency settling errors for $\lambda = 2$ and $p = 2000$ppm, where Fig. 3.8 was used to translate from

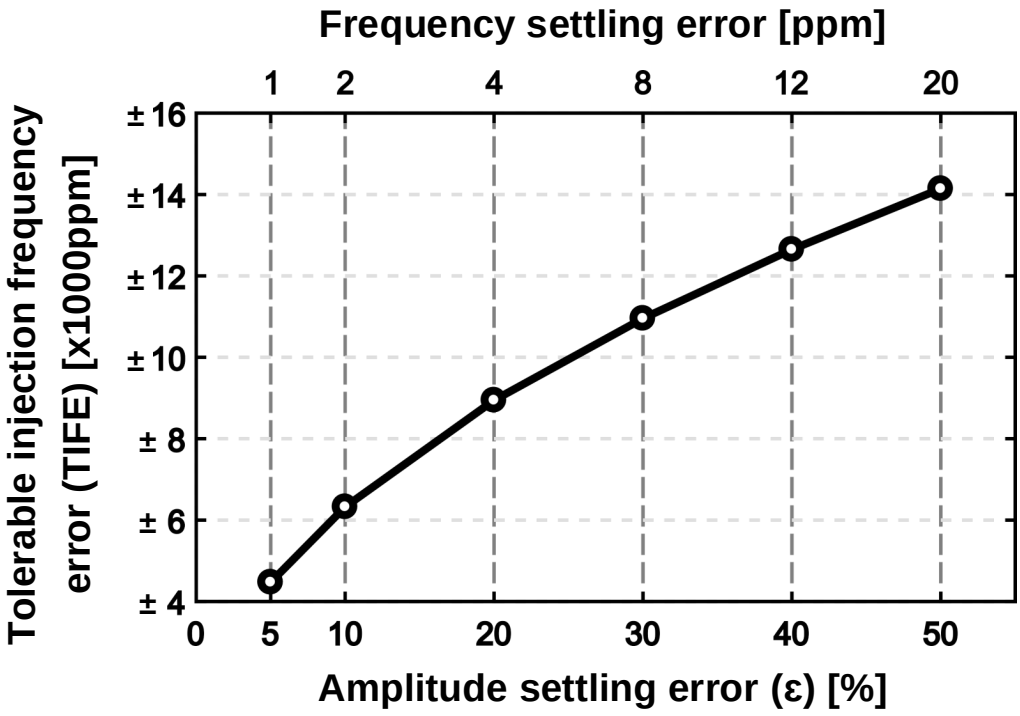

Figure 3.11: TIFE versus the tolerable amplitude/frequency settling errors for $\lambda = 2$ and $p = 2000$ppm.

amplitude to frequency settling errors. As can be seen, the start-up time to reach within 2ppm of frequency error (i.e., for $\varepsilon = 10\%$), remains invariant over TIFE of ±6300ppm, which agrees with the measured TIFE in Section 3.6. State-of-the-art, temperature-compensated, integrated oscillators [1, 51–55] have temperature sensitivities well within this range, which guarantees that they can be used for successful quick start-up over the required operating temperature range, as described later in Section 3.5.

It is interesting to examine the dependency of TIFE on the quality factor of the resonator. A theoretical study in [23] has shown that the pulling factor, p, has the following dependency on the Q factor,

$$\frac{\mathrm{d}p}{\mathrm{d}Q} = \frac{-1}{2Q^2} \cdot \frac{1}{\sqrt{\left(\frac{R_n}{R_m}\right)^2 - 1}} \tag{3.9}$$

As seen in (3.9), for a high-Q oscillator, $\frac{dp}{dQ}$ is negligible suggesting that the pulling factor, and hence the TIFE, are almost independent of the Q factor.

It is worth noting that the improved TIFE of this work is a result of using a precise, short T_{inj}. Even though the key idea of precisely-timed injection is applied to the case of a single-frequency $v_S(t)$, the same idea can be combined with frequency chirping and/or dithering to improve the TIFE of these techniques. The calculation of $T_{inj,opt.}$ for frequency chirping/dithering is beyond the scope of this chapter, however, one can follow the same procedure outlined in Section 3.3.2 to determine the ideal $T_{inj,opt.}$ in each of these cases.

3.4.2 Tolerable Injection Duration Error (TIDE)

The actual injection duration, T_{inj}, can deviate from the ideal value, $T_{inj,opt.}$, for various reasons. The duration error, ΔT_{inj}, will result in an error in the motional current amplitude at the end of pre-energization. For small values of T_{inj}, $I_{m,SS}$ linearly tracks T_{inj}, as is evident from both Fig. 3.2 and (3.4). Consequently, the normalized amplitude error remains less than ε if $|\Delta T_{inj}| < \varepsilon \cdot T_{inj}$. This represents the tolerable injection duration error, TIDE. For instance, as shown by the measurement results (see Section 3.6), for the case of $\varepsilon = 10\%$, the start-up time remains constant for ±10% variations in T_{inj}.

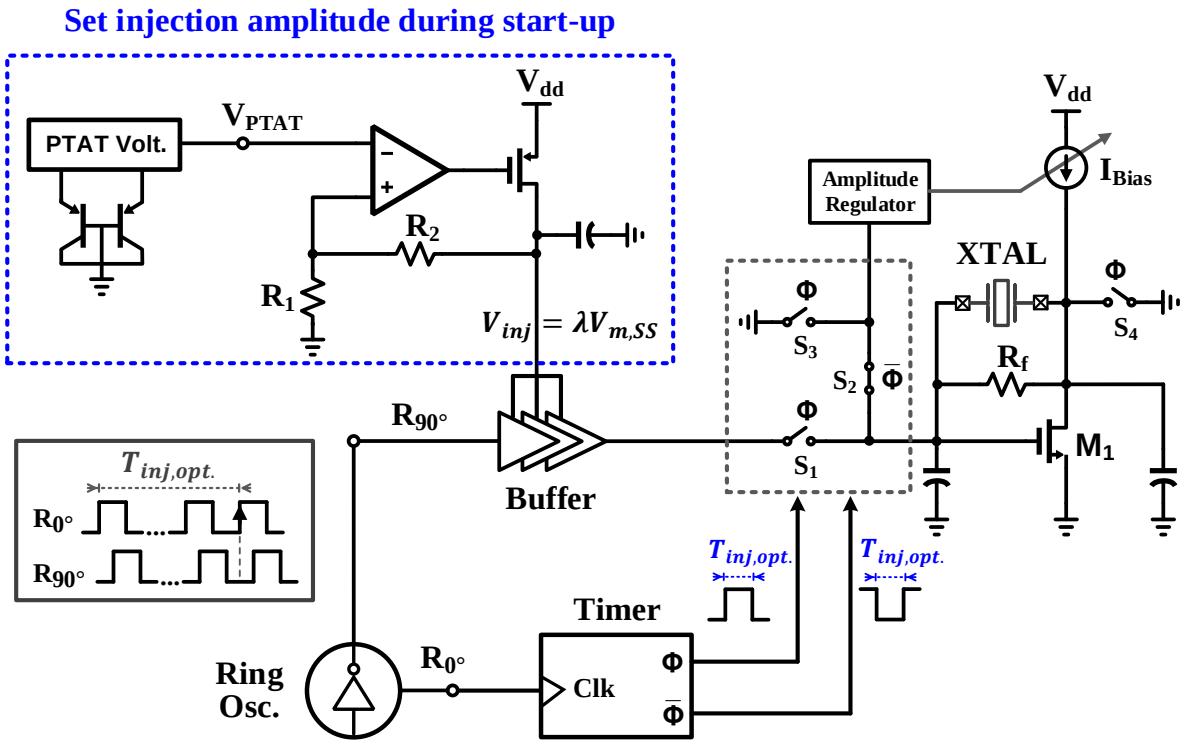

Figure 3.12: Block diagram of the proposed fast start-up crystal oscillator.

3.5 Circuit Implementation

The block diagram of the proposed precisely-timed energy injection technique incorporated in a crystal oscillator is shown in Fig. 3.12. The crystal oscillator is implemented in a commonly-used Pierce configuration along with an amplitude-regulator loop [18, 20, 21]. A proportional-to-absolute-temperature (PTAT) voltage regulator is used to set the injection amplitude, V_{inj}, during start-up. As explained in the following subsection, a PTAT source makes V_{inj} linearly track $V_{m,SS}$ over temperature fluctuations in order to guarantee a constant $T_{inj,opt.}$. Since our proposed technique relaxes the matching requirement between ω_{inj} and ω_m, a simple temperature-compensated ring oscillator with a temperature sensitivity of 85ppm/°C is used as the injection oscillator. At start-up, switch S_1 connects the injection (ring) oscillator to the crystal resonator, through a buffer, for the fixed duration of $T_{inj,opt.}$, during which $i_{m,env}$ builds up to its steady-state value, $I_{m,SS}$.

A simple timer is used to control $T_{inj,opt.}$ by counting an appropriate number ($N = 1/2\pi\lambda p$) of full cycles of the ring oscillator. Note that λ and p, and hence the number of cycles, N, is known *a priori*. As shown in our measurements in Section 3.6, the number of cycles, N, is ~ 100. Since we are counting the cycles of the ring oscillator, the timing error, $|\Delta T_{inj}|$, is less than 0.5 cycle corresponding to only 0.5% error, which is well within the required TIDE of $\pm 10\%$. As shown in Fig. 3.12, the injection signal and the timer's clock are derived from two different phases of the ring oscillator (R_{0° and R_{90°). This ensures that the amplitude regulator is not interrupted with any abrupt voltage change at the end of $T_{inj,opt.}$, and hence it performs a smooth and fast settling. Switches S_2 and S_3 are also used to isolate the amplitude regulator from the fluctuations in the injection signal. Even though a single-ended injection is shown in Fig. 3.12 for the sake of simplicity, the actual implementation is done differentially. To save power, all the start-up auxiliary circuitry is turned off at the end of $T_{inj,opt.}$, which leads to a low start-up energy consumption. The following subsections go over the design of the main crystal oscillator, the injection oscillator, and the buffer in more detail.

3.5.1 Crystal Oscillator With Amplitude Regulator Loop

Amplitude regulators are prevalently used in crystal oscillators to control the oscillation amplitude, $V_{m,SS}$. By adaptively adjusting the bias current, amplitude regulators decrease the contribution of the active circuit's nonlinearities towards the oscillation amplitude and frequency [18]. Therefore, a more stable and predictable oscillation amplitude/frequency is obtained over PVT variations.

Analysis in [23] shows that the oscillation amplitude of a crystal oscillator with an amplitude-regulator loop linearly varies over temperature. As it is evident from Fig. 3.13, the measured variations of $V_{m,SS}$ linearly change over temperature, which agrees with the theoretical prediction. As a result, if V_{inj} is set by a PTAT voltage regulator, as shown in Fig. 3.12, it would linearly track the variations in $V_{m,SS}$. Consequently, $T_{inj,opt.}$ becomes a PVT-invariant constant, following the analysis carried out in Section 3.3.3. Note that since

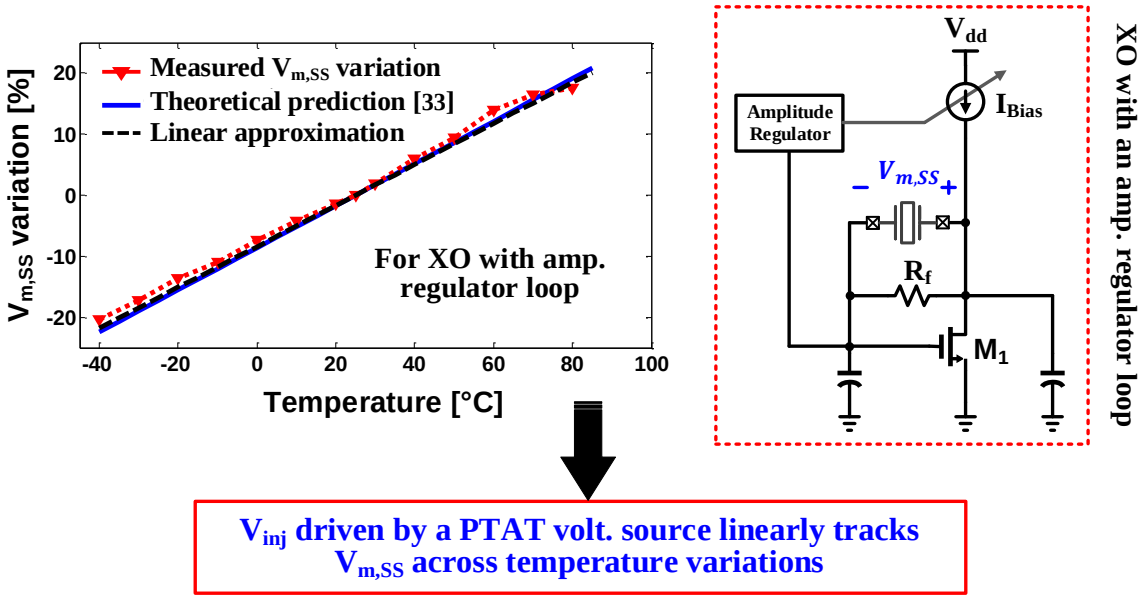

Figure 3.13: Steady-state oscillation amplitude, $V_{m,SS}$, of a crystal oscillator with an amplitude-regulator loop linearly varies over temperature.

$\pm 10\%$ variations in $T_{inj,opt.}$ is tolerable, the linear approximation in Fig. 3.13 needs to be only $\pm 10\%$ accurate. Note that, in practice, in order to determine the value of λ, the value of $V_{m,SS}$ is needed to be known at one arbitrary temperature.

3.5.2 Temperature-Compensated Ring Oscillator

According to the discussion in Section 3.3.1 and the analysis in Section 3.4.1, the proposed technique is very tolerant of large frequency mismatch between ω_{inj} and ω_m. As long as the frequency mismatch is within the TIFE given by (3.8), the transient after T_{inj}, and hence the start-up time, is minimized. This enables the use of a simple on-chip ring oscillator as the injection signal. The ring oscillator is designed using the simple temperature-compensation technique proposed in [1]. The schematic of the ring oscillator is shown in Fig. 3.14(a), where a low-variation current source is used to bias the ring oscillator. The analysis in [1] and [57] is used to obtain the optimized design parameters to ensure a stable bias current I_b —the sum of I_1 and I_2— and hence a stable oscillation frequency in the presence of temperature

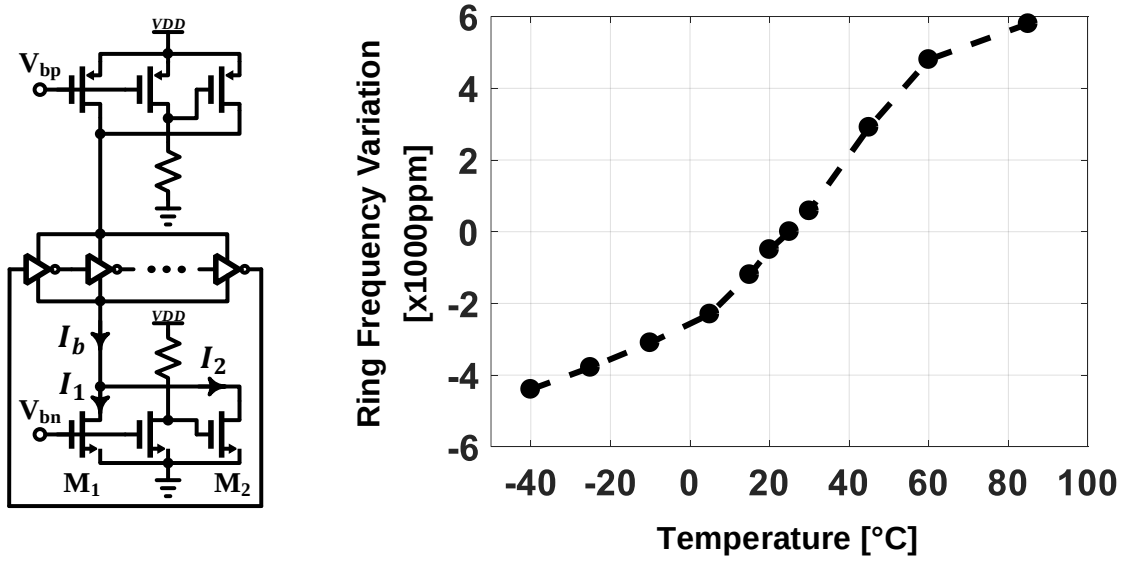

(a)

(b)

Figure 3.14: Temperature-compensated, current-starved ring oscillator [1] (a) schematic (b) measured variation of oscillation frequency over temperature.

fluctuations.

In order to compensate for the variations in CMOS fabrication process, the sizes of the transistors in Fig. 3.14(a), and hence the value of the bias current I_b, are initially trimmed by using proper static control bits. Fig. 3.14(b) shows the measured sensitivity of the ring oscillator's frequency to the temperature variations. On-chip oscillators with lower temperature sensitivities have been reported [53–55], however, the sensitivity shown in Fig. 3.14(b) is sufficient for successful quick start-up over the industrial temperature range, as verified by our measurement results in Section 3.6.

3.5.3 Buffer

The buffer between the ring oscillator and the resonator in Fig. 3.12 is employed to drive the resonator and isolate the ring oscillator from the large capacitive load ($2C_L > 13$pF). The buffer is made up of a chain of standard tapered inverters [58]. Note that since the

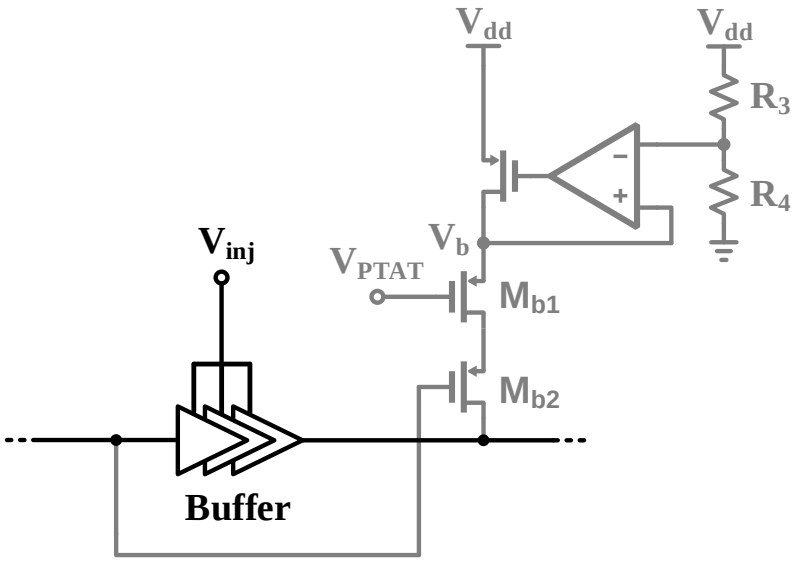

Figure 3.15: A simple technique to reduce the output slew rate variation of the buffer under temperature variations.

supply voltage of the buffer (V_{inj}) varies in a PTAT manner, the slope (slew rate), and hence the fundamental frequency component of the injection signal varies over temperature. According to the analysis in Section 3.4, also verified by the measurement results in Section 3.6, for $\varepsilon = 10\%$, variations within $\pm 10\%$ would not cause any significant degradation in the start-up time. However, as shown in Fig. 3.15, transistors M_{b1} and M_{b2}, along with a voltage regulator, are added to adjust the pull-up strength of the buffer in case V_{PTAT} changes considerably at hot/cold temperatures. Note that as long as V_b in Fig. 3.15 is lower than V_{inj}, the output level of the buffer is set by V_{inj} with proper slew-rate control. Furthermore, using an inverter chain sharpens the transitions in the injection signal and decreases their variations over PVT.

3.6 Measurement Results and Comparison

A prototype IC was fabricated in TSMC 65nm standard CMOS process [49, 50]. The test board along with the die micrograph is shown in Fig. 3.16. The IC includes three different

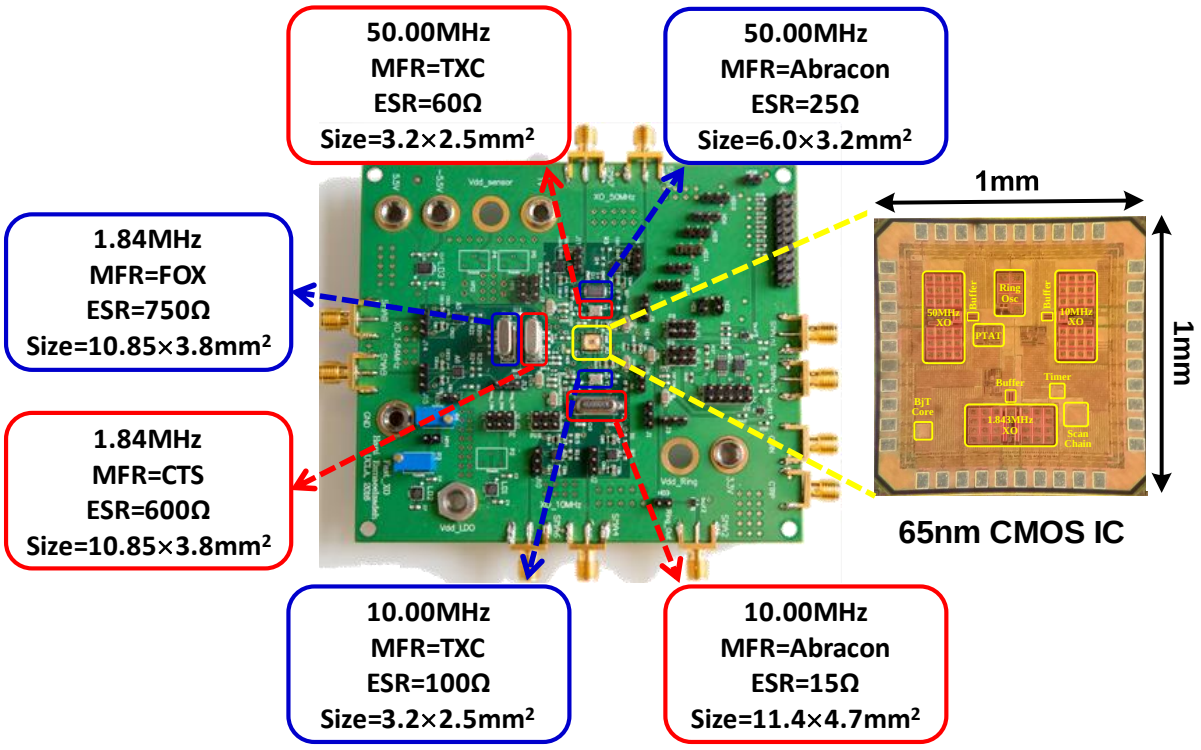

Figure 3.16: Implemented test-board including the fabricated IC and six different tested crystal devices.

crystal oscillators, targeting 1.843MHz, 10MHz, and 50MHz. To verify the robustness of the proposed technique over crystal parameters and frequency variations, two crystal devices with different packagings and Q factors from different manufacturers were tested for each oscillator, as shown in Fig. 3.16. The active area is 0.09mm^2 per crystal oscillator in a 1mm×1mm die. Most of the active area is occupied by the metal-insulator-metal (MIM) capacitor banks, included for debug/testing purposes. Note that a BJT core is used to measure the Si temperature, but only because it facilitates testing the IC over the industrial temperature range.

Fig. 3.17 shows the measured transient output voltage of the 10MHz oscillator for three different injection durations. The output voltage is measured at the gate of the transistor M_1 in Fig. 3.12. In order to isolate the oscillator from the input impedance of the measuring probe, an off-the-shelf discrete operational amplifier (ADA4817) in a unity-gain feedback configuration is used to act as a high-speed analog buffer between the oscillator and the probe. As is evident in Fig. 3.17, there is a long transient time after injection, if the injection duration is not equal to its optimum value of $7.7\mu s$, calculated from (3.6). However, the output signal quickly reaches steady-state when the right amount of $T_{inj,opt.} = 7.7\mu s$ is applied. This result corroborates the proposed theory presented in Section 3.3.

To demonstrate the resilience of the proposed technique, intentional errors in the injection duration, T_{inj}, and the injection frequency, ω_{inj}, are introduced, and the measured start-up times are plotted in Fig. 3.18(a) and (b), respectively, for the 10MHz oscillator. There is no noticeable degradation in the start-up time for up to ±10% variation in $T_{inj,opt.}$, and up to ±6500ppm mismatch between ω_{inj} and ω_m. For comparison's sake, Fig. 3.18(b) also plots the measured start-up time for conventional pre-energization, i.e. when $T_{inj} \neq T_{inj,opt.}$, but an arbitrary $T_{inj} = 6\mu s$ is used instead. As can be seen in Fig. 3.18(b), the proposed technique demonstrates 20x lower start-up time and dramatically lower sensitivity to the injection frequency as well.

It is important that the power overhead needed for the fast start-up circuitry be minimized in order to reduce the overall energy consumption. Table 3.1 shows the breakdown of the start-up energy consumed by each of the start-up auxiliary circuitry. As can be seen, the

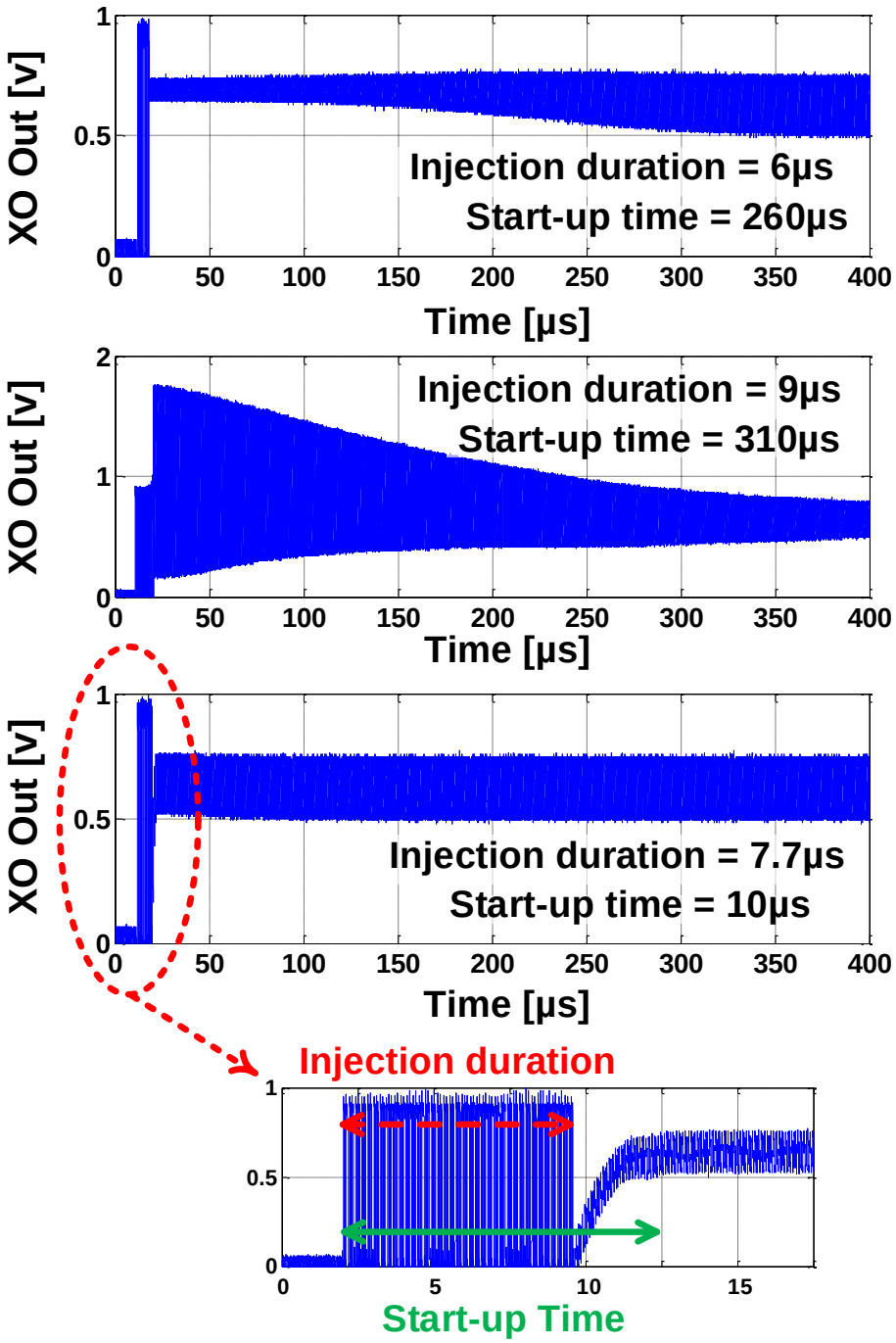

Figure 3.17: Measured transient response of the 10MHz oscillator during start-up (measured at the gate of M_1 in Fig. 3.12) for three different injection durations: start-up time is minimized for $T_{inj,opt.} = 7.7\mu s$.

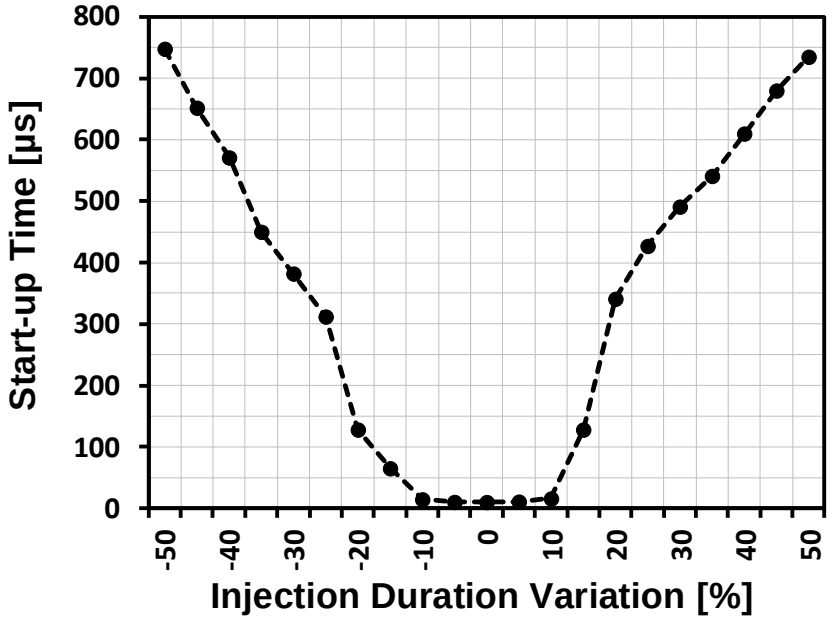

(a)

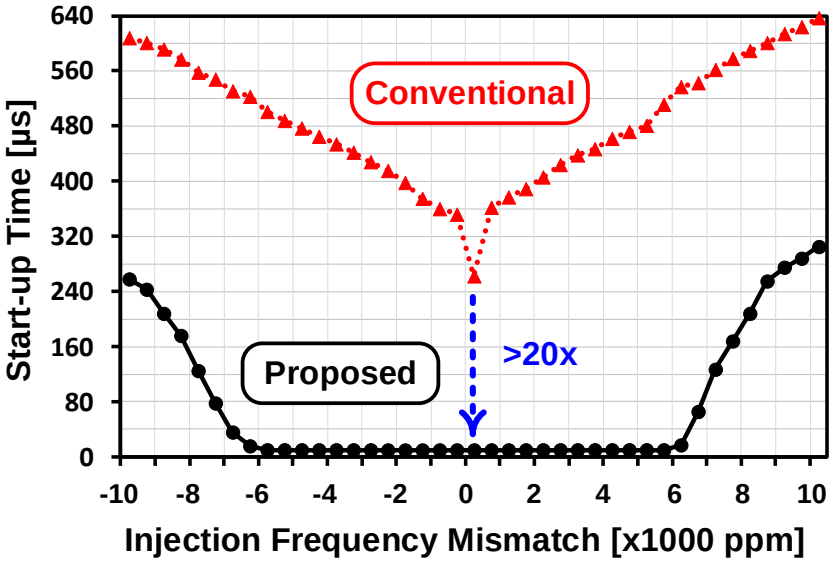

(b)

Figure 3.18: Measured start-up sensitivity of the 10MHz oscillator (a) sensitivity to the variations in the optimal injection duration (b) sensitivity to the injection frequency mismatch: proposed technique shows more than 20x faster start-up with much less sensitivity to the injection frequency.

Table 3.1: Energy consumption breakdown during start-up

	Start-up energy (nJ)		
Frequency (MHz)	**1.84**	**10.0**	**50.0**
Buffer	6.25	10.1	8.74
Ring oscillator	0.75	0.9	0.5
PTAT regulator	4.5	0.9	0.1
Digital circuitry (timer)	0.1	0.1	0.06
Total start-up energy (nJ)	**11.6**	**12**	**9.4**

largest contributor to energy consumption is the buffer mainly because it has to drive the crystal's large capacitive load. To the authors' best knowledge, the proposed technique in this work has the lowest start-up energy in the literature (See Table 3.2). The low start-up energy of this work is a direct result of having a small injection duration.

Measured start-up time variations of the 10MHz XO over temperature for two different injection durations of 6μs and 7.7μs is shown in Fig. 3.19. As evident by the results, start-up time variation is only 3% when the optimum injection duration of 7.7μs is used as opposed to about 80% variation for the non-optimal injection duration of 6μs. The large start-up variation of the non-optimal case is due to the fact that the injected energy is small and the steady state is reached mainly by the feedback loop. The time constant of the feedback loop heavily depends on the nonlinearity of the circuit that is PVT-sensitive. Therefore, the start-up time in the case of non-optimal T_{inj} significantly varies over PVT. Figure 3.20 shows the measured start-up time variations over temperature for each of the six tested crystal oscillators. The injection duration for each case, $T_{inj,opt.}$, is calculated from (3.6). The worst-case start-up time variation is within 10%.

Table 3.2 summarizes the measured performance of the proposed precisely-timed energy injection technique, and compares the results with other fast start-up techniques reported in the literature. Since start-up time scales with the oscillation frequency, to normalize over frequency, the number of cycles needed for start-up is also reported for each design. As can be seen, employing the proposed solution, the crystal oscillator, in all the tested cases, only takes about 100-120 number of cycles to fully turn on, which is $\sim$15x faster than the best case in prior art. It is also worth noting that this implementation of the proposed technique employs a low supply voltage of 1.0V, which is one of the smallest amongst the compared prior art in Table 3.2. Further speed-up can be achieved using a higher supply voltage as it allows a larger injection amplitude.

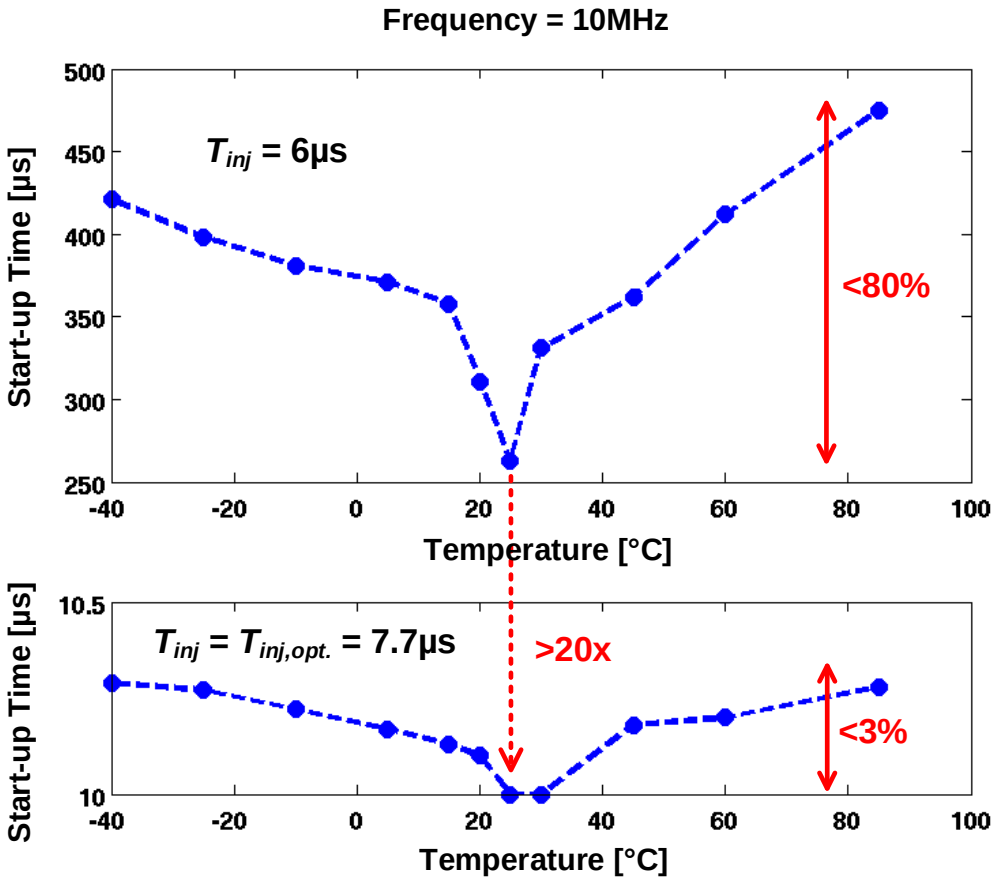

Figure 3.19: Measured start-up time variation of the 10MHz crystal oscillator over temperature: (top) 80% variation in start-up time when injection duration is arbitrarily chosen to 6μs, (bottom) start-up time and its variation are significantly reduced when the optimal injection duration of 7.7μs is applied.

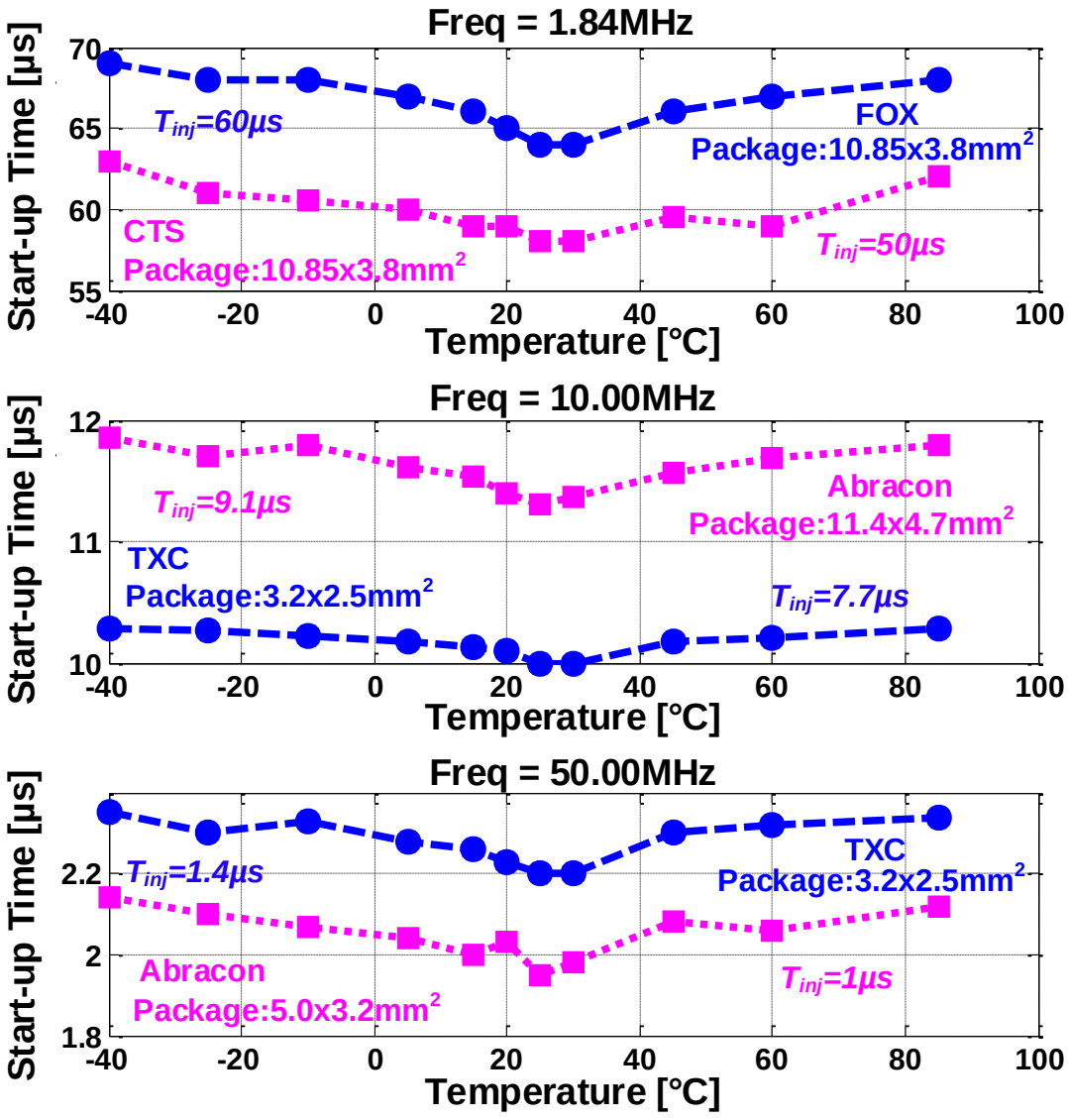

Figure 3.20: Measured crystal oscillator start-up variations over temperature for six different crystal devices (ESR ranging from 15Ω to 750Ω) at three different frequencies.

Table 3.2: Performance summary of the proposed fast start-up technique and comparison with prior art

	RFIC'09 [26]	TI-CC2650 [28]	JSSC'16 [29]	ISSCC'16 [30]	ISSCC'17 [31]	ISSCC'18 [32]	This work (JSSC'18 [50])					
CMOS process (nm)	130	N/A	180	65	90	65	65					
Supply voltage (V)	1.2	3.0	1.5	1.68	1.0	0.35	1.0					
Active area (mm^2)	N/A	N/A	0.12	0.08	0.072	0.023	0.09 per XO					
Frequency (MHz)	19	24	39	24	24	24	50		10		1.8432	
Xtal Manufacturer	N/A	N/A	Daishinku	N/A	N/A	N/A	Abracon	TXC	Abracon	TXC	CTS	FOX
Load capacitance (pF)	N/A	N/A	8	6	10	6	9	9	9	8	6.5	6.5
Steady-state power consumption (μW)	22	N/A	181	393	95	31.8	195	74.2	23.6	45.5	6.7	8.6
Start-up energy (nJ)	N/A	N/A	349	N/A	36.7	14.2	9.4	13.3	13.5	12	11.6	12.7
Start-up time* (μs)	1200	150	158	64	200	400	1.95	2.2	11.3	10	58	64
Start-up time (No. of cycles)	22800	3600	6162	1536	4800	9600	98	110	113	100	107	118
Start-up variation over temperature	N/A	N/A	±7% (-30 to 125°C)	±35% (-40 to 90°C)	27.5% (-40 to 90°C)	7.5% (-40 to 90°C)	10%	7%	5%	3%	9%	8%
							(-40 to 85°C)					
Technique	High g_m	Calibrated RC-Osc. injection	Chirp injection + negative resistance boost	Dithered injection	Dynamically-adjusted load	Chirp injection + inductive loading	Precisely-timed injection					

*Start-up time is defined as the time it takes for the oscillation amplitude to reach 90% of its steady-state value (same definition as prior art).

3.7 Extended Tolerable Injection Frequency Error

While the current implementation of the proposed technique does provide a robust quick start-up, it still requires a temperature-compensated injection oscillator that has frequency variations within the TIFE. The reason that the start-up time increases beyond the TIFE in Fig. 3.18(b) is because of the fact that the injection duration (T_{inj}) is approximated by a constant value, given by (3.6). The approximation is valid for small $\Delta\omega_{inj}$, however, for larger $\Delta\omega_{inj}$, the injection duration should be chosen based on the injection frequency to ensure that the injected energy into the resonator is exactly equal to its steady-state value, i.e., to satisfy (3.2). As proven in Appendix A, the envelope of the motional current at the end of injection duration, given by (3.4), can be approximated by

$$i_{m,env}(T_{inj}) \simeq \frac{T_{inj} \cdot V_{inj}}{2L_m} \cdot \left(1 - \frac{(\Delta\omega_{inj} \cdot T_{inj})^2}{24}\right) \tag{3.10}$$

By substituting (3.10) in (3.2) and using the PVT-invariant technique proposed in Section 3.3.3, the optimal injection duration is found to follow

$$\frac{\Delta\omega_{inj}^2}{24} T_{inj,opt.}^3 - T_{inj,opt.} = -\frac{1}{\lambda \cdot \Delta\omega_{SS}} \tag{3.11}$$

In order to further extend the frequency insensitivity range (TIFE) in Fig. 3.18(b), we propose to dynamically vary the T_{inj} according to (3.11), instead of using a constant value. In this manner, as the injection frequency deviates beyond the "insensitive region", the start-up time is reduced to its minimum value by appropriately changing the T_{inj}. Equation (3.11) shows how T_{inj} needs to be chosen based on the $\Delta\omega_{inj}$. In case of using a non-temperature-compensated injection oscillator, the $\Delta\omega_{inj}$ becomes a function of temperature. Hence, by properly choosing T_{inj} from (3.11), the minimum start-up time can be achieved in the presence of large variations in ω_{inj}.

The measured result of the dynamically-adjusted T_{inj} technique of (3.11) applied to a 10MHz XO is shown in Fig. 3.21. As seen, the minimum start-up time can be maintained over a wide temperature range, if the T_{inj} is properly adjusted (based on (3.11)) over the injection frequency. Note that while Fig. 3.21 only depicts an example of this technique for

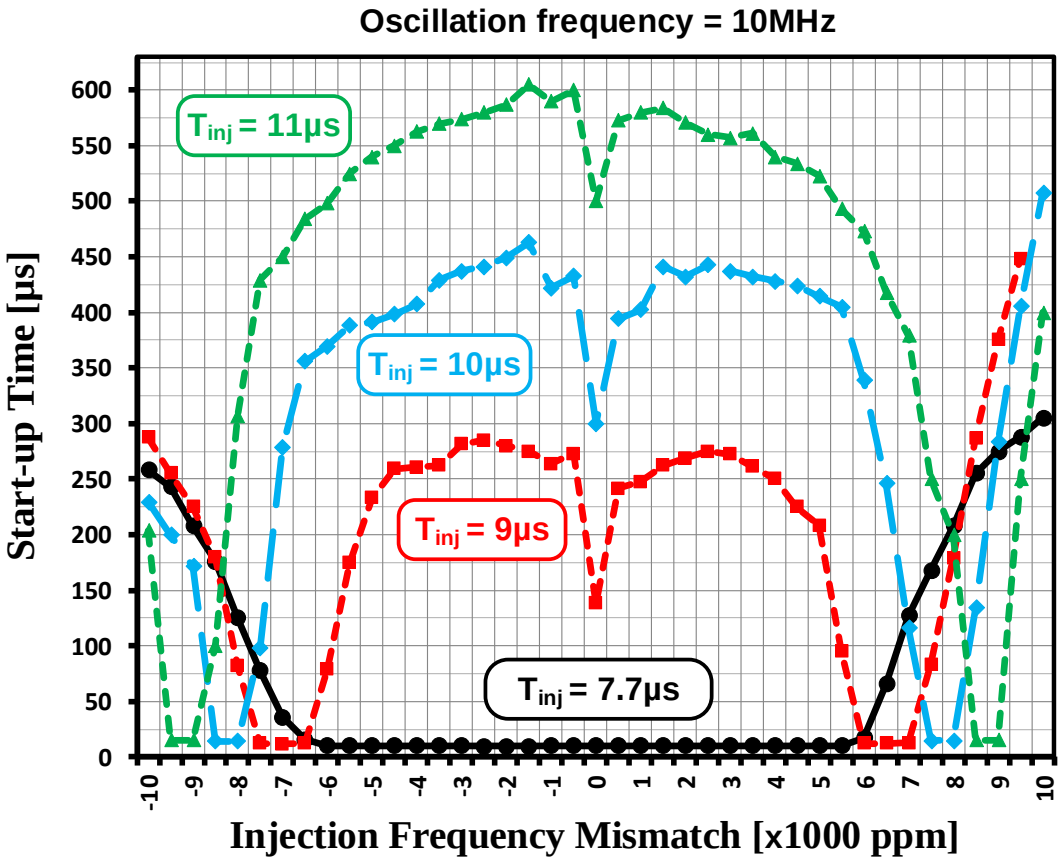

Figure 3.21: Extending the frequency insensitivity range of the 10MHz oscillator by dynamically adjusting the injection duration (measured results).

T_{inj} up to $11\mu s$, larger values of T_{inj} can be used to widen the frequency insensitivity range as needed.

Figure 3.22 shows a possible implementation of the proposed dynamically-adjusted T_{inj} technique where a look-up table hooked up to a temperature sensor is used to control the injection duration based on (3.11). At start-up, the appropriate value of T_{inj} will be applied according to the temperature sensor's output to achieve fast start-up across a wide range of temperature to relax the accuracy requirement of the injection oscillator frequency.

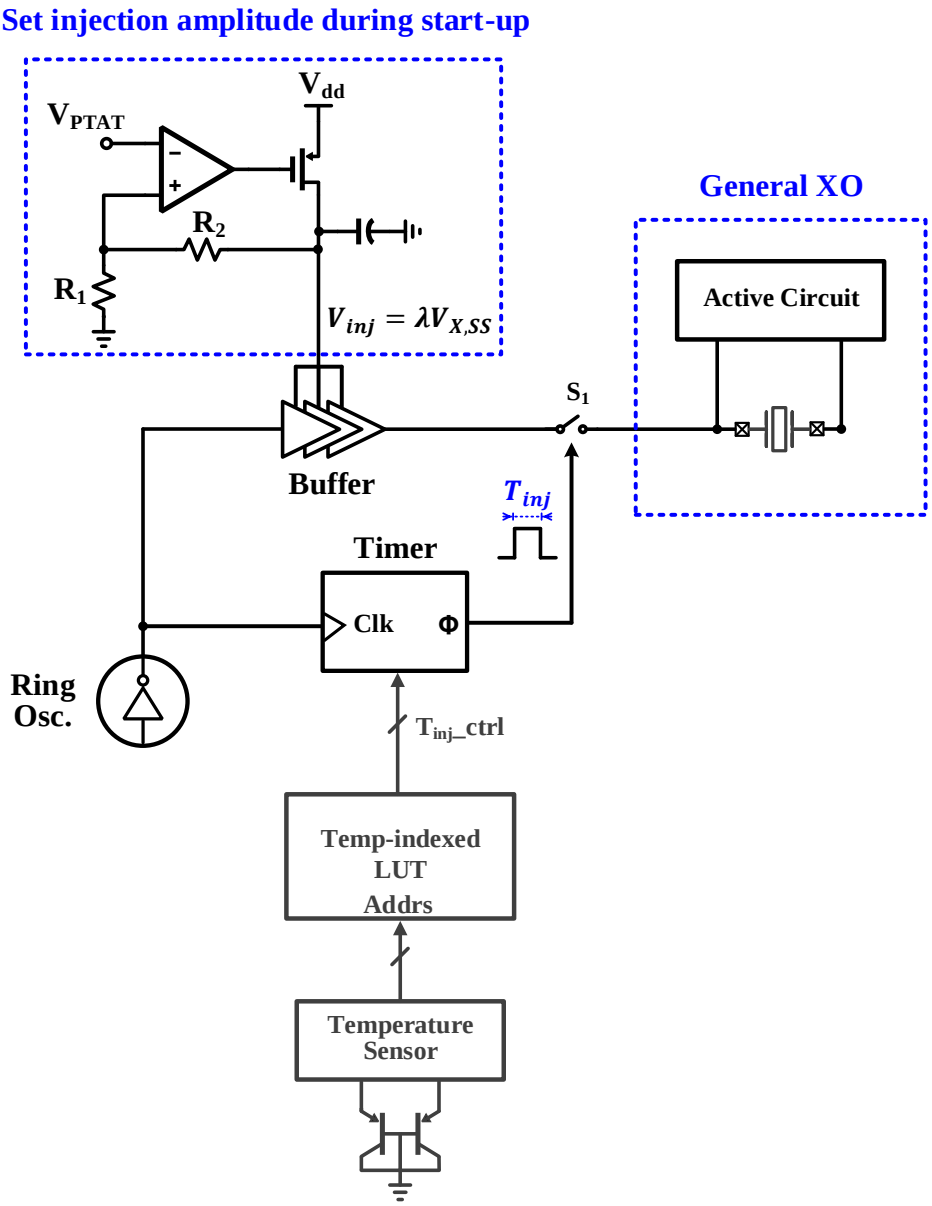

Figure 3.22: A possible implementation of the dynamically-adjusted injection duration technique to extend the TIFE, hence the temperature range.

3.8 A Comparison of Injection-Based Fast Start-Up Techniques

As established before, the start-up time of high-Q oscillators plays a critical role in determining the average power consumption of a duty-cycled system. Moreover, for energy-constrained systems, whether battery-powered or energy-harvesting systems, the start-up energy is crucial as it may demand a large current from the energy source. The energy spent at start-up is typically dominated by the energy consumption of the drivers used to inject energy into the resonator. Therefore, the start-up energy is tightly related to the start-up time. As a result, an injection technique with a shorter start-up time leads to a lower start-up energy consumption. This is why the chirped injection technique usually consumes a high amount of energy at start-up as it has to vary the injection frequency over time to overcome the issue of frequency mismatch. The temperature sensitivity of the injection signal, on the other hand, has a bearing on the start-up time and start-up energy as well. To shed more light on this, let us break down the start-up time to its main components:

$$T_{start-up} = T_{inj} + T_{feedback} \tag{3.12}$$

where T_{inj} is the injection period and $T_{feedback}$ is the feedback loop settling time after the injection signal is disconnected. Figure 3.23 illustrates the general shape of the power spectral density of different injection techniques. As seen, the chirped/dithered injection techniques provide a wider power spread over frequency and as a result, the TIFE is widened. A wide TIFE relaxes the temperature sensitivity requirement of the injection oscillator. However, the amount of energy injected into the resonator is usually very small for the case of chirped/dithered injection. The small injected energy leads to a long feedback loop settling time ($T_{feedback}$ in (3.12)) which prolongs the overall start-up time. Furthermore, since the feedback settling behavior heavily depends on the circuit nonlinearity, the start-up time becomes very sensitive to process, voltage, and temperature (PVT) variations for the chirped/dithered injection. So, even though the chirped/dithered injection relaxes the temperature sensitivity of the injection oscillator, it makes the start-up time very sensitive to PVT variations. Moreover, the chirped/dithered injection leads to a high start-up energy mainly due to its long start-up time and the wide power spread over frequency as well.

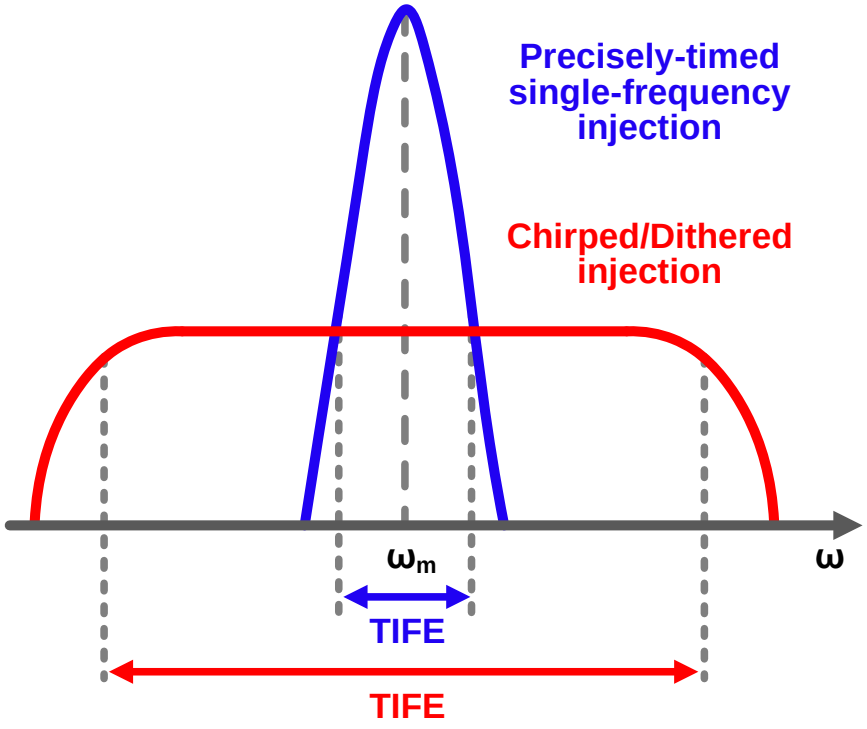

Figure 3.23: Power spectral density of different injection duration.

The proposed precisely-timed injection technique, on the other hand, has a narrower power spectral density as shown in Fig. 3.23 where most of the energy is focused around the resonance frequency, ω_m. With the constant frequency and narrowband injection, a somewhat accurate injection frequency, e.g., ±7500ppm in Fig. 3.18(b), is required to excite the high-Q resonator. As a result, a ring or an RC oscillator has to be compensated over temperature to provide the injection signal. On the other hand, since there is almost no transient settling after the injection signal is disconnected ($T_{feedback} \simeq 0$), the start-up time is minimized. Furthermore, the achieved low start-up time of the precisely-timed injection technique is very stable and PVT-invariant. Because of the dense energy spread around the resonance frequency combined with the small start-up time, the start-up energy of the proposed technique is also very low.

Figure 3.24 depicts the time-domain frequency variation of a chirp-modulated signal.

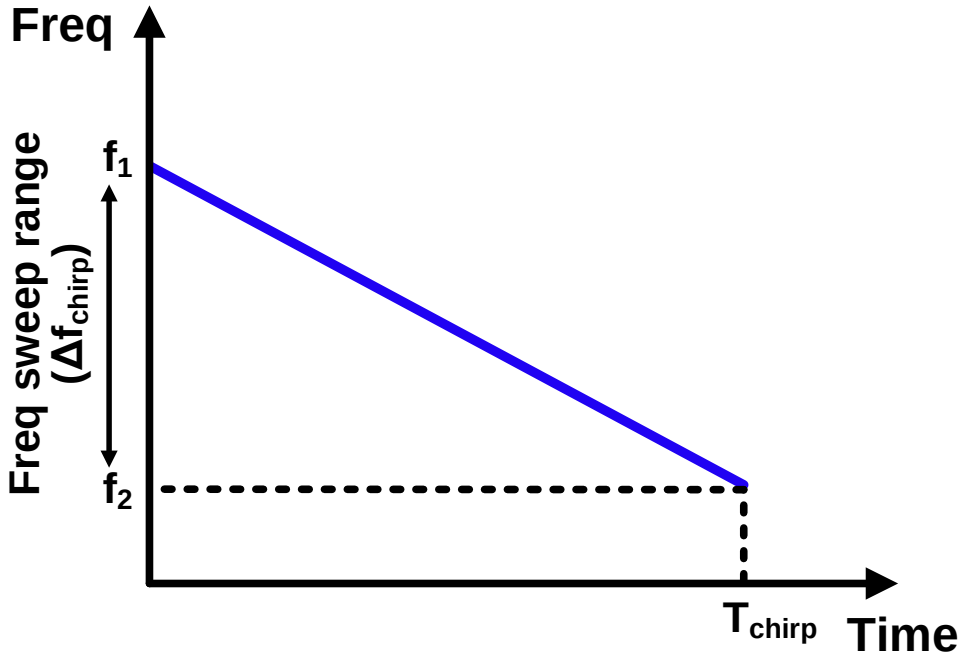

Figure 3.24: Frequency variation of a linear chirp-modulated signal over time.

Such a signal can be expressed in time domain by

$$V_{chirp}(t) = V_{inj} \cdot \sin\left(\omega_1 t + \frac{\Delta\omega_{chirp}}{2T_{chirp}} t^2\right) \tag{3.13}$$

where $\omega_1 = 2\pi f_1$ and $\Delta\omega_{chirp} = \omega_2 - \omega_1$ are the starting angular frequency and the frequency sweep range of the chirp signal, respectively, and T_{chirp} is the duration of the chirp signal according to Fig. 3.24. Normalized spectrum of a chirp-modulated signal described by (3.13) is shown in Fig. 3.25 for the two cases of $\Delta f_{chirp} = 10\% f_m$ with $T_{chirp} = 100\mu s$ and $\Delta f_{chirp} = 50\% f_m$ with $T_{chirp} = 500\mu s$. As seen in the figure, increasing the range of the chirp frequency sweep, i.e., Δf_{chirp}, by 5 times increases the spectrum bandwidth by 5 times, while decreasing the energy density by the same factor. Nonetheless, a chirp-modulated signal provides a wide-band injection spectrum which avoids the need of an accurate injection oscillator. However, as discussed in the following, chirp injection requires a long injection duration that consequently increases the start-up time and start-up energy consumption.

Assuming a high Q-factor, the envelope of the motional current, i.e., $i_{m,env}(t)$, of a res-

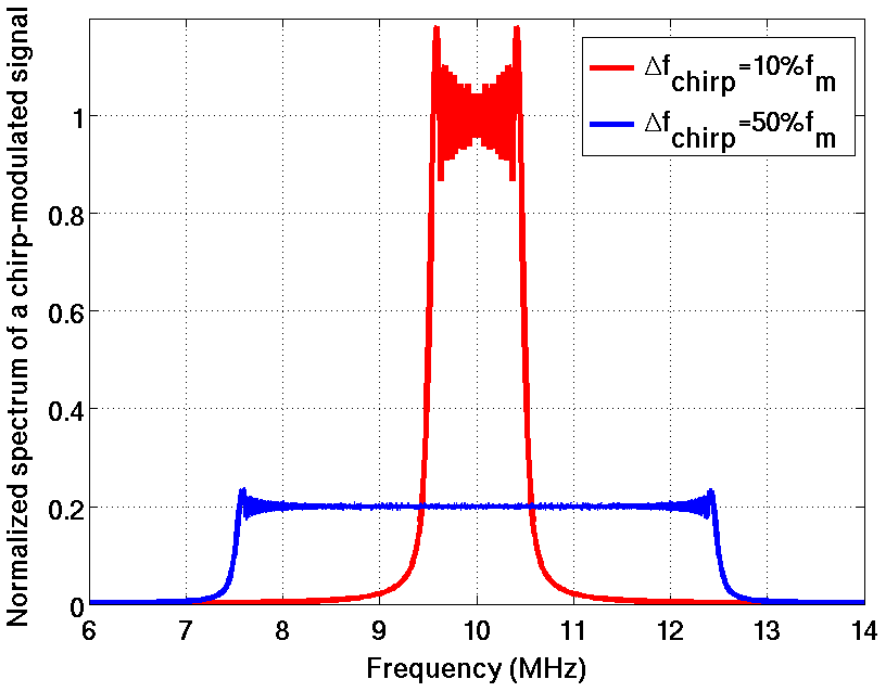

Figure 3.25: Normalized spectrum of a chirp-modulated signal with $\Big(\Delta f_{chirp} = 10\% f_m$, $T_{chirp} = 100\mu s\Big)$, and $\Big(\Delta f_{chirp} = 50\% f_m$, $T_{chirp} = 500\mu s\Big)$.

onator driven by a chirp-modulated signal expressed in (3.13) at $t = T_{chirp}$ is given by [29]

$$i_{m,env}(t = T_{chirp}) = \frac{V_{inj}}{2L_m} \cdot \sqrt{\frac{T_{chirp}}{|\Delta f_{chirp}|}} \tag{3.14}$$

Using our findings described in Section 3.3, stating that the optimal injection duration is achieved when the injected energy into the resonator is exactly equal to its steady-state energy as expressed in (3.2), we find the optimal chirp duration for a desired frequency sweep range Δf_{chirp} to be

$$T_{chirp} = |\Delta f_{chirp}| \cdot \Big(\frac{2L_m \cdot I_{m,SS}}{V_{inj}}\Big)^2$$

$$= |\Delta f_{chirp}| \cdot \Big(T_{inj,opt.}\Big)^2 \tag{3.15}$$

where $T_{inj,opt.}$ is the optimal injection duration of the proposed single-frequency, precisely-timed energy injection (PTI) that is given by (3.5). Equation (3.15) shows how the chirp

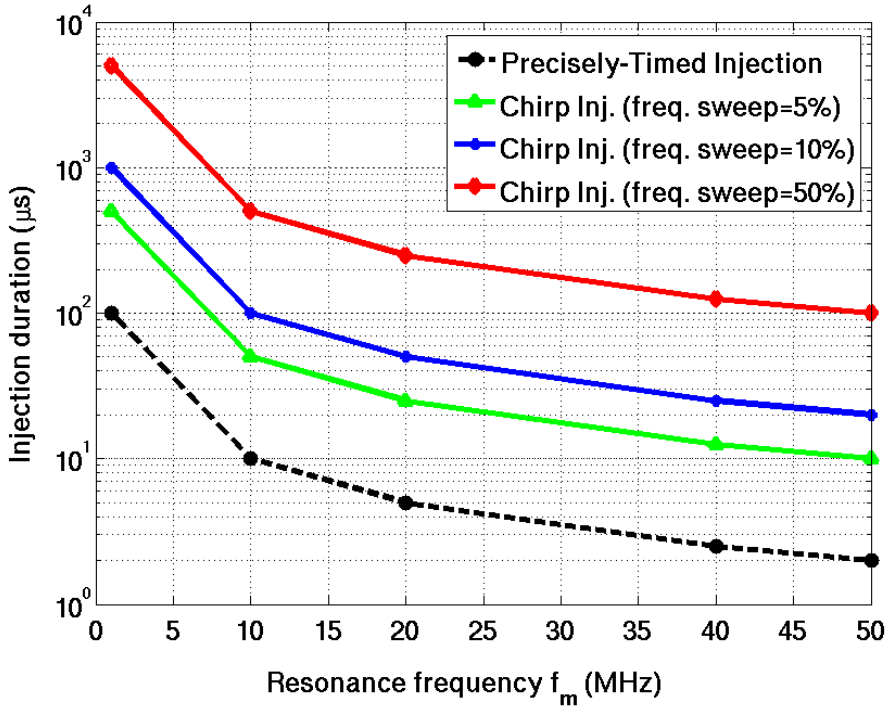

Figure 3.26: Optimal injection duration of the single-frequency, precisely-timed injection technique compared to the chirp injection technique over different oscillation frequency.

duration with a certain Δf_{chirp} relates to the proposed precisely-timed injection technique described in Section 3.3. The optimal injection duration for a single-frequency, precisely-timed injection technique as opposed to the chirp injection is shown in Fig. 3.26 for multiple resonators with different resonance frequencies as well as different frequency sweep ranges for the chirp-modulated signal. As seen, the precisely-timed injection technique is in the orders of magnitude faster than the chirp injection technique, which also leads to a very small start-up energy consumption.

Circuit-level simulations of the transient response of a 10MHz resonator driven by a chirp-modulated signal for $100\mu s$ with a $\Delta f_{chirp} = 10\% f_m$ is shown in Fig. 3.27(b). The time-dependent frequency variation of the applied chirp signal is shown in Fig. 3.27(a). As seen, the amplitude of $i_m(t)$ rapidly starts to increase once the injection frequency matches the resonator's resonance frequency f_m, which in this example happens at $50\mu s$. As a comparison, the same resonator is excited by a single-frequency injection signal that is about 10,000ppm away from the resonance frequency. The transient response is shown in Fig. 3.27(c). As

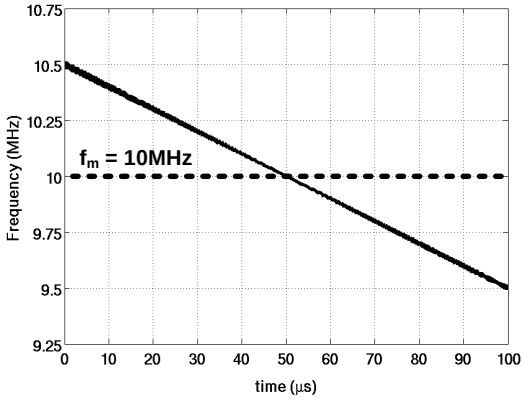

(a)

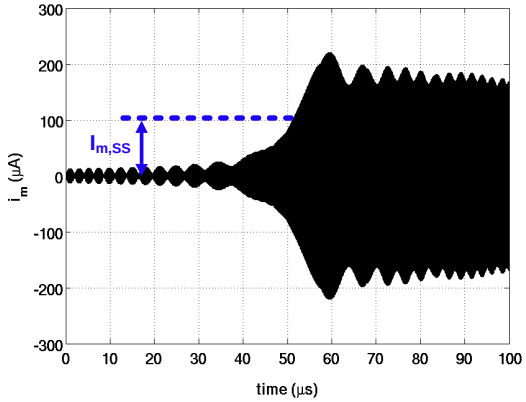

(b)

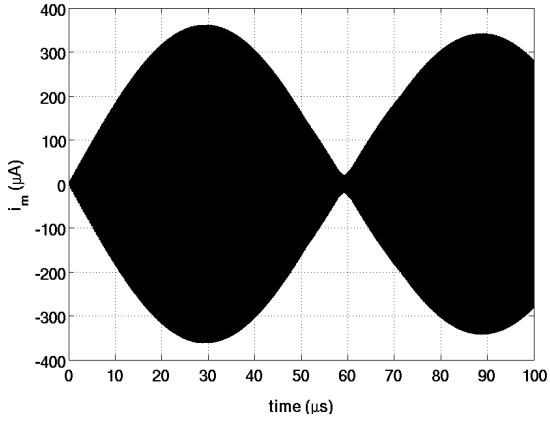

(c)

Figure 3.27: Simulated time-domain waveforms of (a) chirp frequency with $\Delta f_{chirp} = 10\% f_m$ and $T_{chirp} = 100\mu s$ (b) resonator's motional current in response to the chirp waveform (c) resonator's motional current due to a single-frequency injection signal.

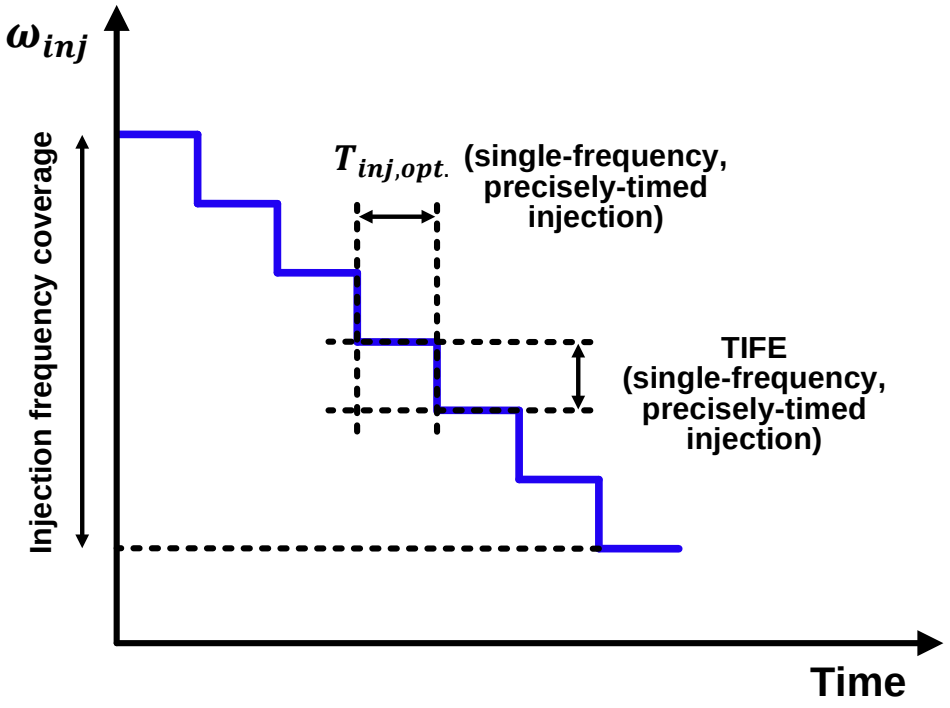

Figure 3.28: Injection frequency profile of a chirped, precisely-timed injection technique.

evident in the figure, the precisely-timed injection technique takes less than $10\mu s$ to reach a steady-state current of $100\mu A$ while the chirped injection technique can take up to $100\mu s$ depending on when the transient frequency matches the resonance frequency. As the injection frequency sweep of the chirped signal increases, the injection duration also has to increase according to (3.15) and also shown in Fig. 3.26.

One technique to further relax the temperature sensitivity requirement of the injection oscillator is to use a dynamically-adjusted injection duration instead of a fixed one as described in Section 3.7. A possible implementation of this technique is shown in Fig. 3.22 where a temperature sensor along with a look-up table is required. Another possible solution is to combine the precisely-timed energy injection technique with a chirped injection oscillator. Figure 3.28 shows the injection frequency profile of such a combination where the duration of each frequency step is equal to the optimum injection duration of a single-tone injection calculated from (3.6). With each step covering a TIFE of a single-tone injection ($\pm$7500ppm in Fig. 3.18), a much wider frequency coverage can be achieved by using multiple frequency

steps as shown in Fig. 3.28. As long as the frequency of the injection oscillator is within the frequency coverage of Fig. 3.28, the combined chirped injection technique changes the injection frequency to bring it to within the TIFE of a single-frequency injection shown in Fig. 3.23. Doing so greatly relaxes the frequency stability requirement of the injection oscillator and minimum start-up time is achieved as long as the resonance frequency falls within the injection frequency coverage of Fig. 3.28. A simple envelope detector can be used to extract the oscillation amplitude and stop the injection signal once steady-state oscillation is detected. The combined chirped injection widens the power spectral density of the proposed precisely-timed injection shown in Fig. 3.23 while it ensures that the required steady-state energy is injected into the resonator regardless of the injection frequency. In comparison with the precisely-time injection technique, the combined chirped injection technique greatly relaxes the frequency sensitivity requirement of the injection signal at the cost of increased start-up time and energy.

In summary, the dithered/chirped injection relaxes the temperature sensitivity of the injection oscillator, but it makes the start-up time very sensitive to PVT variations. Furthermore, the start-up time is usually long such that the chirp technique is usually combined with another technique, e.g., increasing g_m in [29] or inductive loading in [32], to reduce the start-up time. The long start-up time increases the start-up energy as well. The proposed precisely-timed injection (PTI) technique, on the other hand, drastically reduces the start-up time and energy and makes the start-up time very robust and almost insensitive to PVT variations. This comes at the cost of a higher temperature stability requirement of the injection oscillator. A combination of the two chirped and PTI techniques, as shown in Fig. 3.28, can relax the temperature stability requirement of the injection oscillator while achieving a rather robust and fast start-up with low start-up energy.

CHAPTER 4

Ultra-Low Power 32KHz Crystal Oscillator

As mentioned earlier, many sensor nodes in Internet-of-Things (IoT) applications are battery powered. Hence, burst-mode communication, where the radio is only activated when needed, is widely used to reduce the average power consumption and improve the battery life as a result. The wake-up and synchronization function in a duty-cycled IoT radio is typically performed by a sleep timer. As will be discussed in this chapter, the frequency of sleep timers has to be very accurate and stable that dictates the use of crystal oscillators. High frequency stability in the sleep timers is required to accurately synchronize the transmitter and receiver to minimize the power consumption. Furthermore, since the sleep timer is always ON, its power consumption has to be minimal.

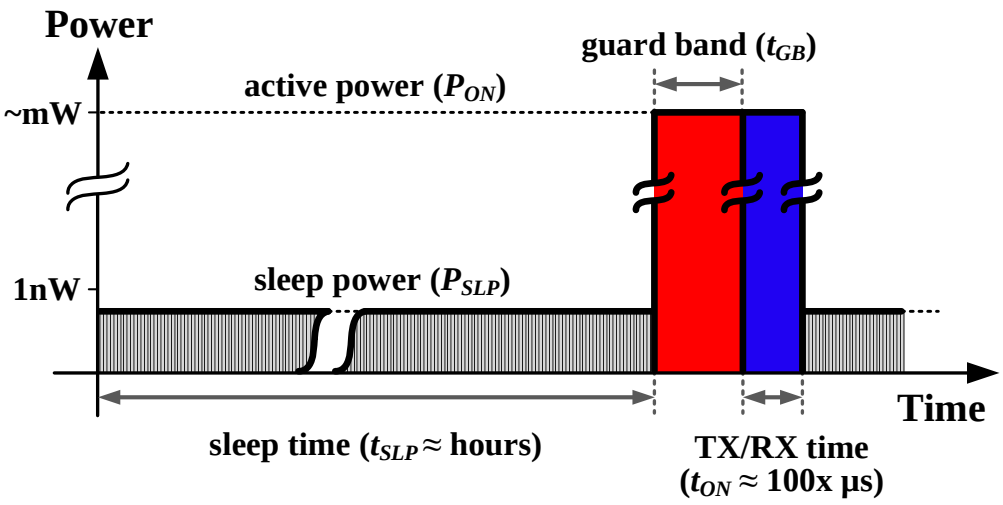

Figure 4.1: A simplified timing profile of an IoT radio.

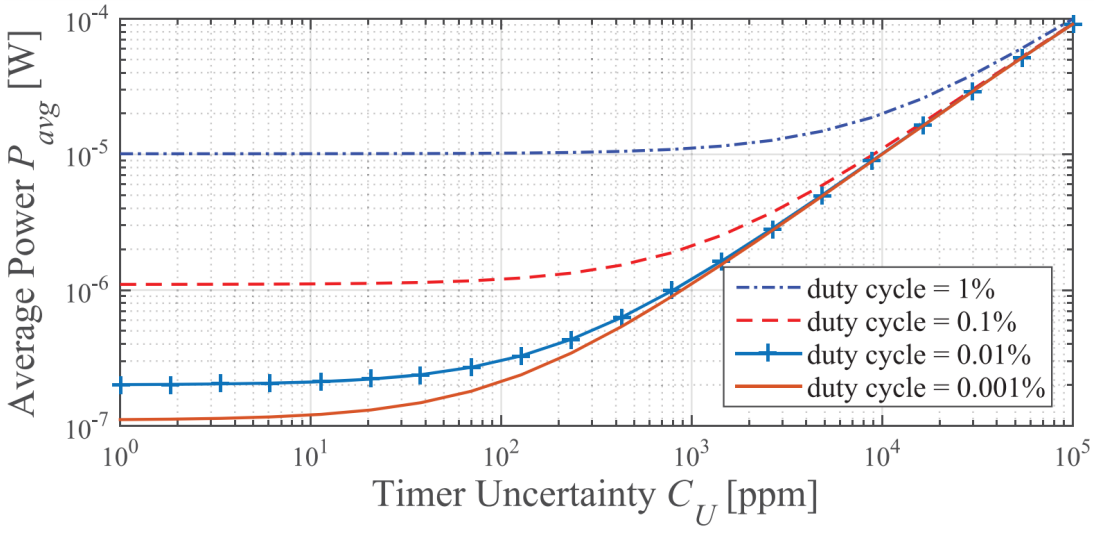

Figure 4.2: Average power consumption of a duty-cycled radio as a function of the timing accuracy of the sleep timer for various duty-cycle ratios [2].

4.1 Performance Requirement of Sleep Timers

As discussed, the sleep timer is always ON to synchronize the transmitting and receiving functions. As a result, its power consumption is crucial in heavily duty-cycled radios where the system spends most of the time in the sleep mode. Furthermore, if the sleep timer has some frequency inaccuracy, the radio receiver has to turn on early during a guard band window, t_{GB}, to ensure that the receiver receives the transmitted packet. A simplified timing profile for a duty-cycled IoT radio is shown in Fig. 4.1 [2]. The average power consumption (P_{avg}) can be calculated from the following equation:

$$P_{avg} = \frac{P_{SLP} \cdot t_{SLP} + P_{ON} \cdot (t_{ON} + t_{GB})}{t_{SLP} + t_{ON} + t_{GB}} \tag{4.1}$$

where t_{SLP} is the sleep time, t_{ON} is the ON time post guard band, and P_{SLP} and P_{ON} are the sleep power and the active power, respectively (Fig. 4.1). Timing uncertainty of the sleep timer leads to a large guard band (t_{GB}) and can significantly increase the average power consumption of wireless sensing nodes according to (4.1).

Figure 4.2 illustrates the dependency of the average power consumption on the sleep timer uncertainty for various duty-cycle ratios. As can be seen, For sufficiently low duty-cycles,

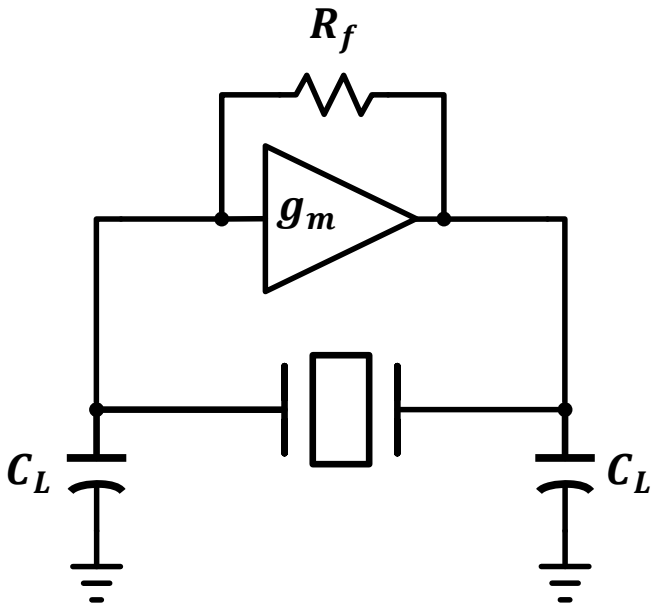

Figure 4.3: Conventional Pierce crystal oscillator.

there is limited additional reduction of average power for a more aggressive duty-cycling. This is because the average power consumption of the system is limited by the sleep power at very low duty-cycles. Moreover, the average power consumption in Fig. 4.2 quickly increases with the timer uncertainty.

All in all, in order to reduce the average power consumption of the system, it is crucial for the sleep timer to be extremely low power (sub-nW) with very small timing inaccuracy.

4.2 Pierce XO as a Sleep Timer

The high timing accuracy requirement of the sleep timers necessitates the use of crystal oscillators to provide the timer functionality. Pierce oscillator is the most commonly-used XO configuration because of its simple implementation. A conventional implementation of the Pierce crystal oscillator is shown in Fig. 4.3. Considering only the load capacitors, C_L, and neglecting all the other capacitors, the negative resistance shown by the active circuit

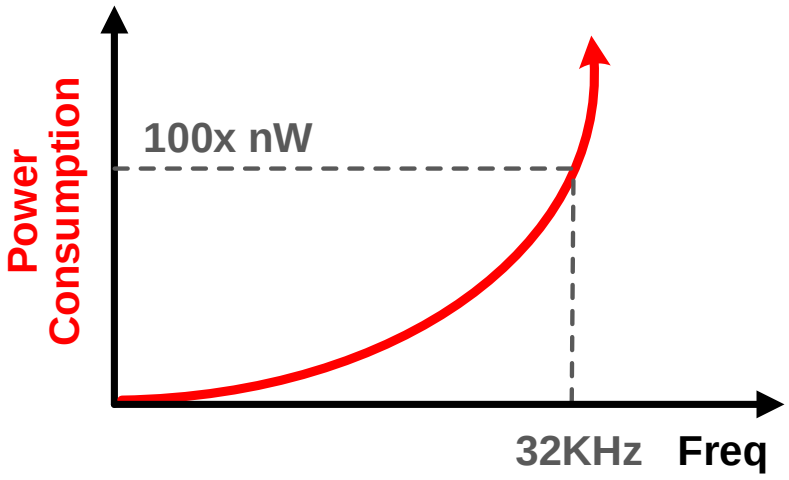

Figure 4.4: Power consumption of Pierce crystal oscillators quadratically increases with the oscillation frequency.

at the oscillation frequency is

$$R_N = -\frac{g_m}{C_L^2 \cdot \omega_O^2} \tag{4.2}$$

where g_m is the transconductance of the active circuit and ω_O is the oscillation frequency. In order to maintain the oscillation, R_N has to be greater than the motional resistance of the resonator, R_m, to compensate for the resonator's loss, hence

$$g_m > \omega_O^2 \cdot C_L^2 \cdot R_m \tag{4.3}$$

Equation (4.3) shows that the transconductance, and hence the current consumption, of Pierce XO quadratically increases with the oscillation frequency and the load capacitance. It is also important to note that large load capacitors are required for this architecture to minimize the sensitivity of the oscillation frequency to parasitics resulting from the PCB traces, I/O pads, and etc. This causes a trade-off between the power consumption and frequency stability of Pierce XOs. As shown in Fig. 4.4, the power consumption of Pierce XOs is in the orders of 100nW for a 32KHz sleep timer, which is too much for heavily duty-cycled IoT systems.

4.3 Review of Prior Art

A number of techniques have been reported in the literature to reduce the power consumption of crystal-based sleep timers to sub-10nW levels. In [3], the average power consumption of a Pierce XO is reduced to 1.5nW (at room temperature) by operating at a reduced XO voltage swing and also duty-cycling the sustaining amplifier. The circuit architecture of the ULP XO proposed in [3] is shown in Fig. 4.5. Since ULP is achieved by operating at low XO swing and supply, low-threshold (LVT) transistors are needed to achieve better performance at 0.3V supply voltage. LVT transistors increase the leakage current and limit the power efficiency. Furthermore, the bias current and hence the negative resistance of this implementation is very sensitive to PVT variations. Therefore, significant calibration is needed to address the PVT sensitivity and to ensure that the design meets the oscillation criteria at all times. An external resistor (R_C in Fig. 4.5) is also needed as part of the calibration circuitry. Since the oscillation does not die right away once the amplifier is disabled, duty-cycling the amplifier between ON and OFF states is used to further reduce the power consumption (from 2.1nW to 1.5nW). Extra control circuitry is required to properly time the amplifier duty-cycling. Even though the main sustaining amplifier runs of a low 0.3V supply, a second supply voltage of 0.9V is needed for the calibration and control circuitry.

Another technique introduced in the literature that effectively reduces the power consumption is a pulse injection scheme that strives to eliminate the high-power sustaining amplifier used in the Pierce XO [4, 5, 59]. The pulse injection technique injects narrow current pulses at the peaks and trough of the XO output waveform in order to compensate for the crystal loss. By injecting only at these extremes, the XO voltage swing is recovered and the power consumption is reduced. However, precise timing of the injection pulses is required to improve the power efficiency. The authors in [59] incorporated a delay-locked loop (DLL) into the XO to generate the injection signals and were able to achieve a room temperature power consumption of 5.58nW. However, this approach requires a high-power amplifier and delay cells that limit the power efficiency of the technique. The design in [59] also requires multiple power domains and careful power planning to reduce the power consumption to

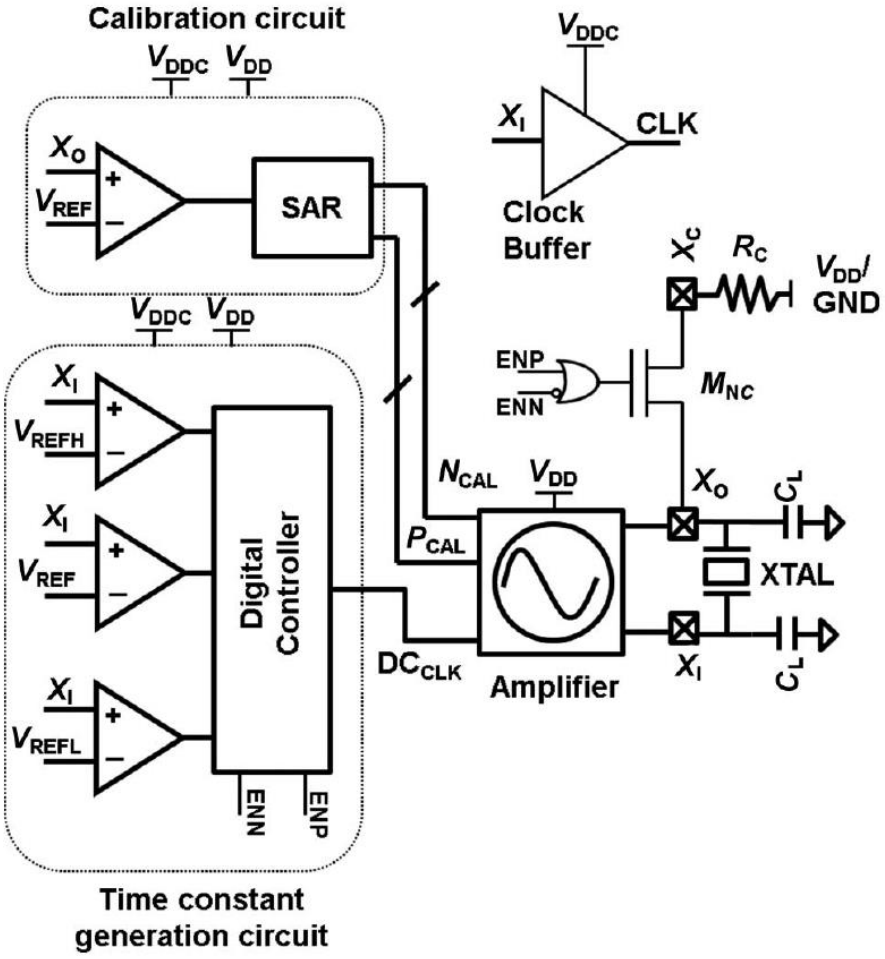

Figure 4.5: Circuit architecture of the ULP XO developed in [3].

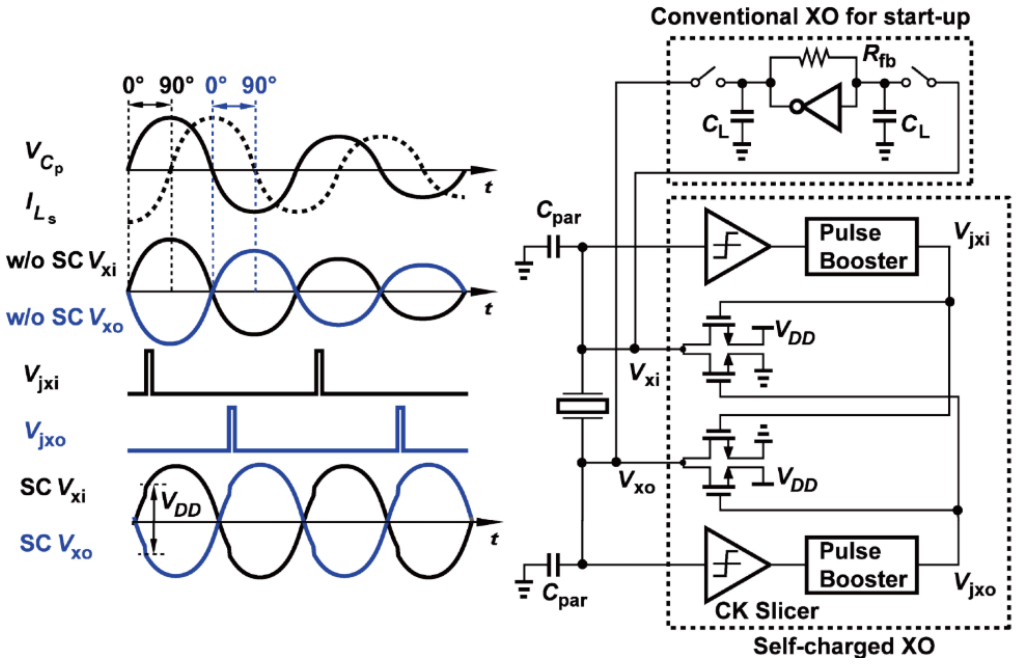

Figure 4.6: Architecture and waveforms of the self-charging XO proposed in [4].

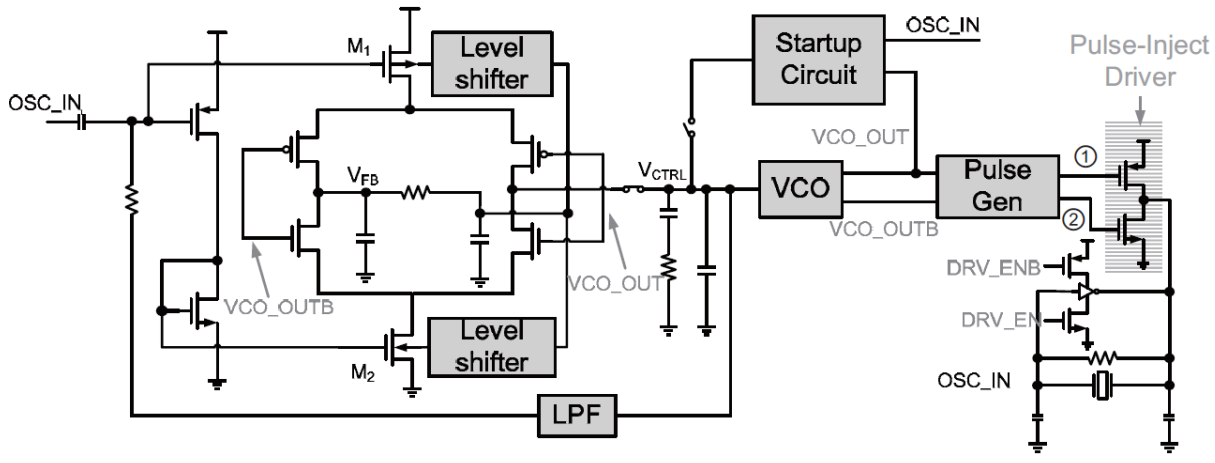

Figure 4.7: Circuit architecture of the XO proposed in [5].

nW scale. It also has a large area and complicated designs for its implementation. A self-charging XO design introduced in [4] reduces the power consumption to 5nW measured at room temperature. The architecture of the self-charging XO along with its waveforms are shown in Fig. 4.6. In this architecture, a self-charging loop is used to periodically inject charge at both ends of the crystal resonator (V_{xi} and V_{xo}) to replenish the energy loss in the crystal's motional resistance. The logic-based design of this architecture provides low-power consumption by eliminating the need of any high-power amplifiers. However, the injection timing is not accurate that degrades the injection efficiency. To ensure accurate timing of the pulse injection signals, [5] uses a 90° phase aligned PLL to generate the injection signals. By improving the injection efficiency by properly timing the injection signals, [5] reported a low-power consumption of 1.7nW measured at room temperature. The circuit architecture of this technique is shown in Fig. 4.7. Since the PLL used in this architecture has very limited locking range, it needs a conventional PLL to ensure that the VCO locks to the correct frequency. This architecture also requires two power domains, one for the main PLL and start-up circuit and another one for the XO pulse-inject drivers. It is also important to note that one common requirement of the pulse injection scheme [4, 5, 59] is some sort of start-up circuitry to establish the initial oscillation signal. Since the start-up time of sleep timers does not have to be short, the start-up circuit is typically a conventional Pierce amplifier.

4.4 Sub-nW Sleep Timer Based on a DC-Only Sustaining Amplifier

In this section, we present a new ultra-low power XO architecture that achieves sub-nW power consumption for a 32KHz sleep timer. As mentioned in Section 4.2, the power consumption of Pierce XO quadratically increases with the oscillation frequency as illustrated in Fig. 4.4. The basic idea of this work is to process the oscillation signal at DC, instead of the oscillation frequency, in order to reduce the power consumption of the main amplifier.

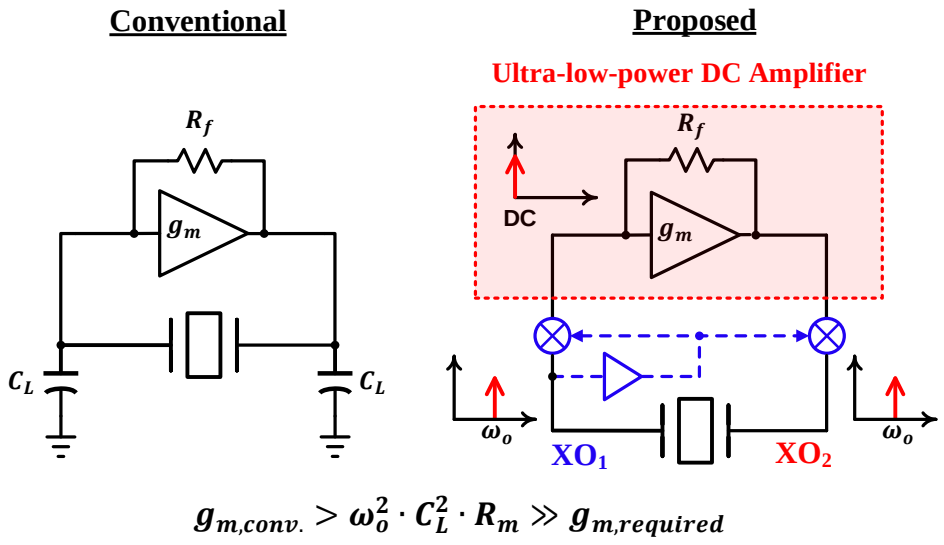

(a)

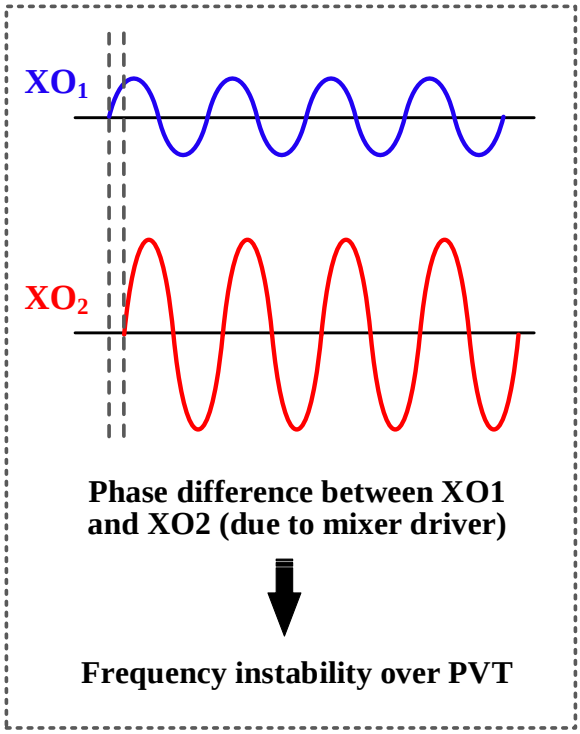

(b)

Figure 4.8: (a) Basic concept of the proposed ULP XO (b) phase difference between the XO_1 and XO_2 waveforms degrades the frequency stability.

4.4.1 Theory of Operation

Figure 4.8 illustrates the basic concepts of the proposed ultra-low power oscillator architecture. As depicted in Fig. 4.8(a), the new structure, instead of amplifying the oscillation signal at the oscillation frequency, downconverts the crystal's motional current to DC, amplifies it at DC, then upconverts the amplified signal back to the oscillation frequency. By processing the oscillation signal at DC, the proposed techniques eliminates the aforementioned minimum g_m requirement of the Pierce XO, and only requires that the DC amplifier's feedback resistor, R_f, to be sufficiently greater than the motional resistance of the crystal, R_m. As shown later, the DC amplifier can be designed to consume as low as 50pW.

It is important to note that the frequency conversion (to DC and back) shown in Fig. 4.8(a) can result in a non-zero phase shift across the resonator (Fig. 4.8(b)). This is mainly due to the delay in the mixers' gate-drivers as shown in Fig. 4.9. The problem with a non-zero phase shift is that it varies over PVT and consequently degrades the frequency stability of the XO. Downcoversion of the oscillation signals using two orthogonal signals is proposed in the next section to address this issue.

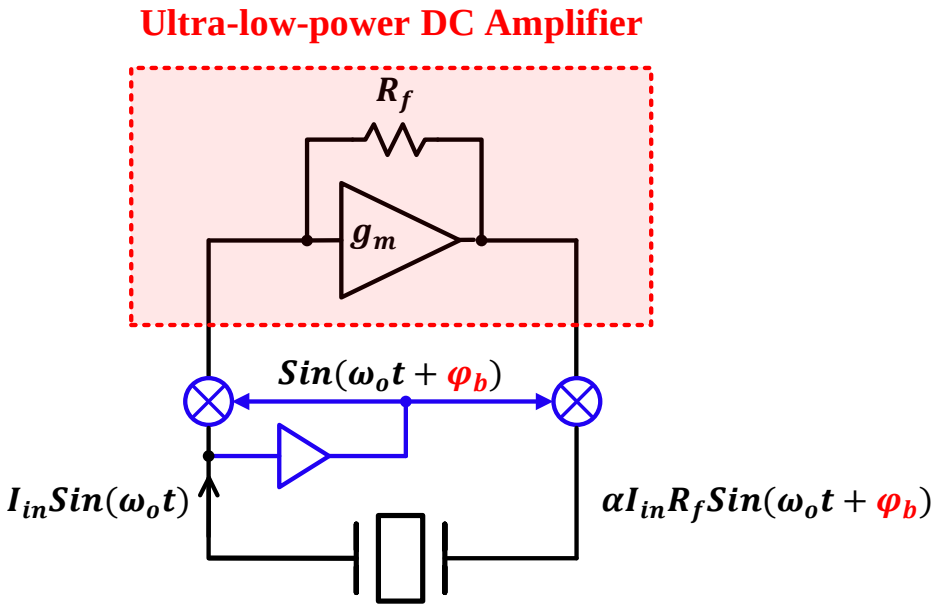

Figure 4.9: Phase difference across the resonator as a result of mixer's gate-driver.

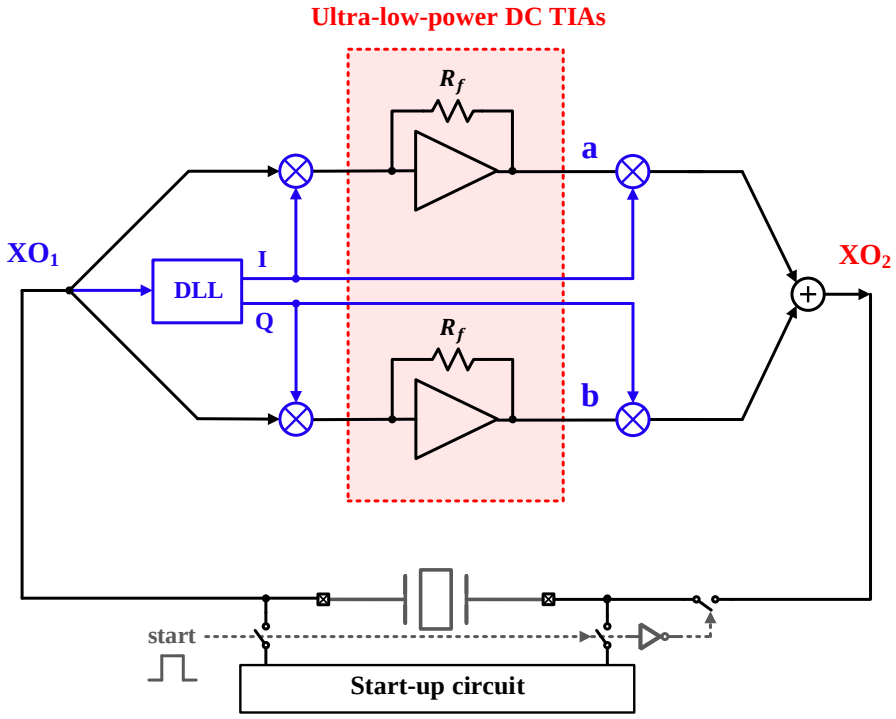

Figure 4.10: Employing orthogonal I/Q paths to maintain zero-phase shift across the resonator- series resonance.

4.4.2 Frequency Conversion Using Orthogonal I/Q signals

As mentioned in the previous section, downconversion of the oscillation signal to DC, by self-mixing, loses the phase information of the signal and creates a phase shift in the waveforms across the resonator that degrades the frequency stability of the XO. In order to address this issue, we use two orthogonal signals, i.e., 90° out-of-phase I/Q signals, to downconvert and subsequently upconvert the oscillation signal. This idea is shown in Fig. 4.10. As will be shown shortly, employing orthogonal I/Q signal paths in the frequency conversions preserves the phase information of the oscillation signal and ensures a nominally zero phase shift across the resonator. Consequently, the XO oscillates at its series-resonance frequency. Since the quality factor of the resonator is maximum at its series-resonance frequency, the proposed architecture improves frequency stability even without requiring large load capacitors. This further improvers the power efficiency of the XO.

4.4.2.1 Principle of Operation

According to Fig. 4.11, $i_m(t) = I_m \sin(\omega_O t + \theta)$ is the motional current of the resonator, which passes through the passive current-commutating mixers. The mixers are driven by orthogonal, binary I/Q signals. As a result, the motional current, $i_m(t)$, is multiplied by 90° out-of-phase square waves that toggle between -1 and +1. The downconverted signals at the TIA inputs are[1]:

$$i_I = \frac{1}{2} i_m(t) \cdot \operatorname{sgn}\Big(\sin(\omega_O t)\Big) \tag{4.4}$$

$$= \frac{1}{2} I_m \sin(\omega_O t + \theta) \cdot \frac{4}{\pi} \sum_{n=0}^{\infty} \frac{1}{2n+1} \sin\Big((2n+1)\omega_O t\Big)$$

$$= \frac{1}{2} I_m \sin(\omega_O t + \theta) \cdot \frac{4}{\pi} \Big[\sin(\omega_O t) + \frac{1}{3}\sin(3\omega_O t) + \cdots \Big]$$

$$= \frac{1}{\pi} I_m \Big(\cos(\theta) - \cos(2\omega_O t + \theta) + \frac{1}{3}\cos(2\omega_O t - \theta) + \cdots \Big)$$

$$i_Q = \frac{1}{2} i_m(t) \cdot \operatorname{sgn}\Big(\cos(\omega_O t)\Big) \tag{4.5}$$

$$= \frac{1}{2} I_m \sin(\omega_O t + \theta) \cdot \frac{4}{\pi} \sum_{n=0}^{\infty} \frac{(-1)^n}{2n+1} \cos\Big((2n+1)\omega_O t\Big)$$

$$= \frac{1}{2} I_m \sin(\omega_O t + \theta) \cdot \frac{4}{\pi} \Big[\cos(\omega_O t) - \frac{1}{3}\cos(3\omega_O t) + \cdots \Big]$$

$$= \frac{1}{\pi} I_m \Big(\sin(\theta) + \sin(2\omega_O t + \theta) + \frac{1}{3}\sin(2\omega_O t - \theta) + \cdots \Big)$$

Assuming that the TIA has a small bandwidth and a gain of $K.R_f$ with a phase shift of

[1] $\operatorname{sgn}(\cdot)$ is the signum function, defined as $\operatorname{sgn}(x) = \frac{x}{|x|}$.

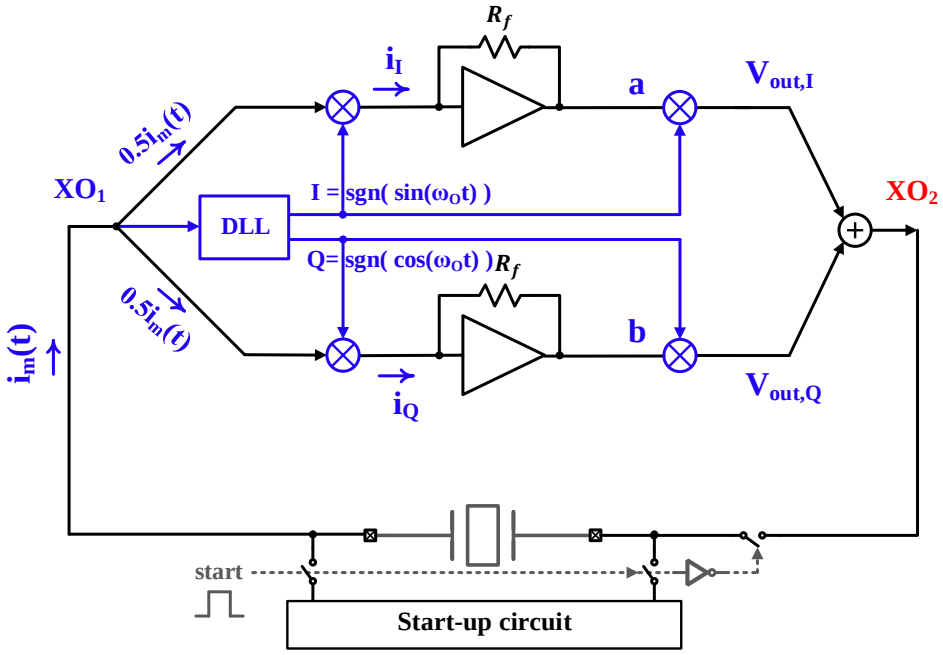

Figure 4.11: Principle of operation of the ULP XO with I/Q frequency conversion.

$-\phi_{TIA}$ at $2\omega_O$ where $K < 1$ (Fig. 4.12) while it sufficiently suppresses the higher-order harmonic contents in i_I and i_Q:

$$V_a = \frac{1}{\pi} I_m R_f \Big(\cos(\theta) - K\cos(2\omega_O t + \theta - \phi_{TIA}) + \frac{K}{3}\cos(2\omega_O t - \theta - \phi_{TIA}) \Big) \tag{4.6}$$

$$V_b = \frac{1}{\pi} I_m R_f \Big(\sin(\theta) + K\sin(2\omega_O t + \theta - \phi_{TIA}) + \frac{K}{3}\sin(2\omega_O t - \theta - \phi_{TIA}) \Big) \tag{4.7}$$

Finally the crystal driving signal XO_2 is

$$XO_2 = V_a \cdot \mathrm{sgn}\Big(\sin(\omega_O t)\Big) + V_b \cdot \mathrm{sgn}\Big(\cos(\omega_O t)\Big) \tag{4.8}$$

$$= \frac{4}{\pi^2} I_m R_f \Big(\cos(\theta)\cdot\sin(\omega_O t) + \sin(\theta)\cdot\cos(\omega_O t)$$

$$+ K\sin(\omega_O t + \theta - \phi_{TIA}) + \frac{K}{9}\sin(\omega_O t + \theta + \phi_{TIA}) + \cdots \Big)$$

Now, assuming that the TIA has a very small gain at $2\omega_O$, i.e., $K << 1$, and all the higher-

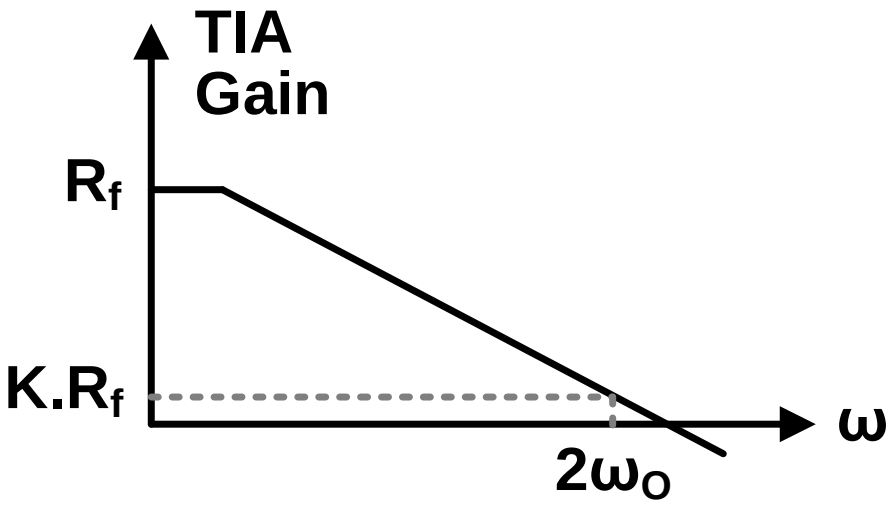

Figure 4.12: Frequency response of the ULP TIA.

order harmonic content of XO_2 are suppressed by the narrow bandwidth of the high-Q resonator, we have

$$XO_2 = \frac{4}{\pi^2} I_m R_f \sin(\omega_O t + \theta) \tag{4.9}$$

As seen in (4.9), employing orthogonal signals to perform the frequency conversion preserves the phase information such that XO_2 has the same phase as $i_m(t) = I_m \sin(\omega_O t + \theta)$. This causes the resonator to oscillate at its series resonance frequency, i.e., $\omega_O = \omega_m$. Oscillation at series resonance improves the frequency stability without requiring the large load capacitor common in Pierce XO.

4.4.2.2 Barkhausen Criteria

Barkhausen criteria states that a circuit may oscillate at a frequency ω_O, if the following conditions are satisfied [60]:

$$|T(j\omega_O)| \geq 1 \tag{4.10}$$

$$\angle T(j\omega_O) = 0 \tag{4.11}$$

where $|T(j\omega_O)|$ and $\angle T(j\omega_O)$ are the amplitude and phase of the oscillator's loop transfer function at the frequency $\omega = \omega_O$, respectively. From (4.9) and the fact that the resonator's impedance at its series resonance frequency is equal to its motional resistance, R_m, we find the loop gain to be

$$|T(j\omega_O)| = \frac{4}{\pi^2} \cdot \frac{R_f}{R_m} \tag{4.12}$$

The amplitude condition of the Barkhausen criteria, (4.10), demands that

$$R_f \geq \frac{\pi^2}{4} \cdot R_m \tag{4.13}$$

In order to ensure oscillation in the presence of PVT variations, R_f should be chosen at least twice or three times the required value.

The second Barkhausen criterion stated in (4.11) is automatically satisfied in the proposed architecture of Fig. 4.10 as the total phase shift of the signal traveling around the loop is always zero.

4.4.3 Ultra-Low Power Realization

The block diagram shown in Fig. 4.10 strives to achieve very low-power consumption by amplifying the oscillation signal at DC. However, the output adder sums up the upconverted I/Q signals and consequently consume a high power consumption. In this section, we show that the same functionality can be achieved without explicitly using a power-hungry adder.

As depicted in Fig. 4.13(a), the output adder sums up the amplified, upconverted I/Q signals, i.e., $XO_2 = a{\cdot}I + b{\cdot}Q$ where a and b are the amplified DC signals in the I and Q path, respectively. As a result, the output of the adder, i.e., XO_2, is a 4-level signal at the oscillation frequency as shown in Fig. 4.13(a). The four different levels are named V_1 through V_4, and they correspond to different combination of the sum of a and b, i.e., $(\pm a \pm b)$.

Alternatively, instead of using a high-power adder, the signal XO_2 can be generated by switching between the four DC levels, $V_1, \cdots, V_4$, using non-overlapping 25%-duty-cycle signals, $D_1, \cdots, D_4$, respectively. As shown in Fig. 4.13(b), by using $D_1, \cdots, D_4$, the same functionality is achieved while avoiding an explicit power-hungry adder.

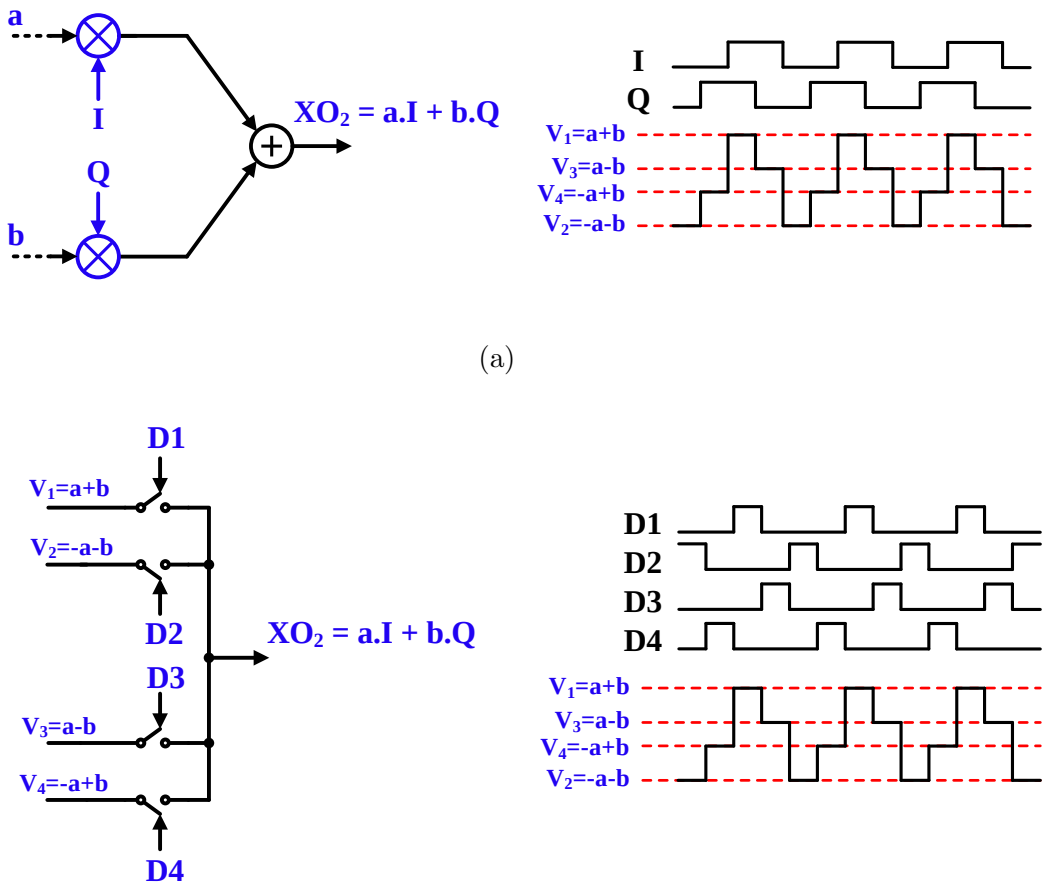

Figure 4.13: (a) Output adder functionality (b) low-power implementation of the output adder using 25%-duty-cycle signals, $D_1, \cdots, D_4$.

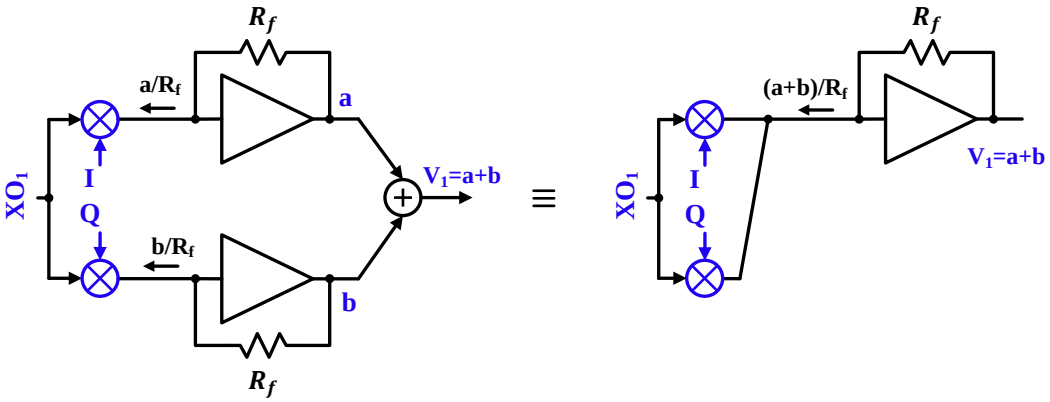

(a)

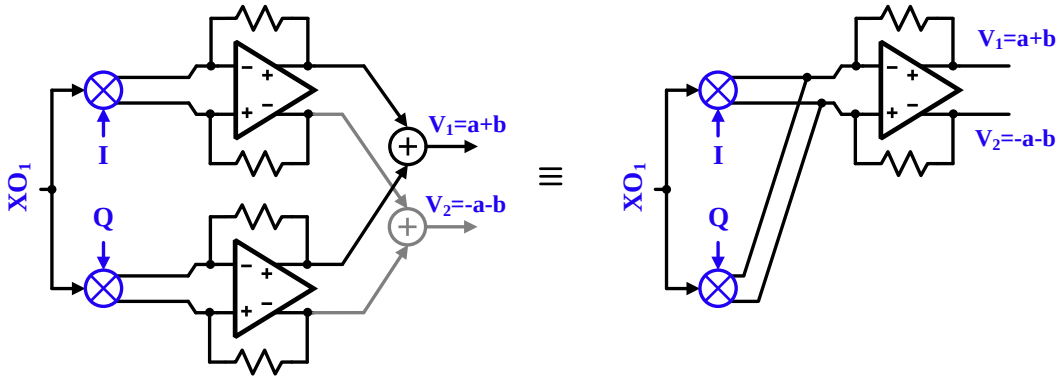

(b)

Figure 4.14: (a) Realization of V_1 (b) differential implementation is used to realize V_2.

The DC voltages V_1 through V_4 can be implemented using DC adders. Figure 4.14(a) shows a simple implementation of V_1 as an example. To further simplify the hardware implementation, the addition functionality can be moved to the current domain, i.e., the input of the TIA. Since adding signals in the current domain is as simple as shorting them together, the implementation of signal V_1 is simplified by avoiding the DC adder and one TIA as shown in the right part of Fig. 4.14(a).

Since $V_2 = -a - b$ is the negative of $V_1 = a + b$, signal V_2 becomes available by simply using differential TIAs. The implementation of V_1 and V_2 is shown in Fig. 4.14(b). With a similar approach, the DC signals V_3 and V_4 can be implemented.

The block diagram of the proposed ULP XO is shown in Fig. 4.15. Passive current-commutating mixers are used to downconvert the oscillation signal to DC, which feed the TIAs. The voltage levels ($V_1 = a + b$) and ($V_3 = a - b$) are generated by downconverting XO_1 using $(I + Q)$ and $(I - Q)$ instead of I and Q, respectively. The other voltage levels ($V_2 = -a - b$) and ($V_4 = -a + b$) are available simply from using differential TIAs. All four passive mixers are implemented using transmission gates. Small transistors suffice since their on-resistance is smaller than the high motional resistance of 32kHz crystal devices ($R_m > 30k\Omega$).

The DC output currents of the mixers are amplified by ULP TIAs. The TIAs are realized by using a low-voltage, ULP two-stage opamp. Each opamp consumes only 50pW and, as will be described later, is biased by a PTAT current source to ensure a constant-g_m over temperature. The design of the TIA and the ULP opamp is discussed in Section 4.4.5.2.

An amplitude control loop is used to control the oscillation amplitude by comparing the maximum value of V_1 through V_4 with a reference voltage and adjusting the TIA gain accordingly. The detailed implementation of the amplitude control loop will be discussed in Section 4.4.5.3. Voltage-controlled feedback resistors are used in each TIA to vary the gain by the amplitude control loop. The voltage-controlled feedback resistors are implemented by using PMOS transistors as will be shown later in Section 4.4.5.2.

The amplified DC output signals of the TIAs, i.e., V_1 through V_4, are switched back to the resonator by using non-overlapping 25%-duty-cycle signals, D_1 through D_4. Any higher-order harmonic content resulting from mixing is greatly suppressed by the low bandwidth of the DC TIAs and the high-Q crystal.

A ULP delay-locked loop (DLL) derives the binary I/Q signals from the oscillation signal and is described later in Section 4.4.5.4. The 25%-duty-cycle signals, D_1 through D_4, are generated from the I and Q signals by using a 25%-duty-cycle clock generator circuit that is described in Section 4.4.5.5. To reduce the power consumption of the output buffer, the rail-to-rail swing at either I/Q signals can be taken as the XO final output.

Since the I/Q signals are unavailable at start-up, a dedicated start-up circuit is required.

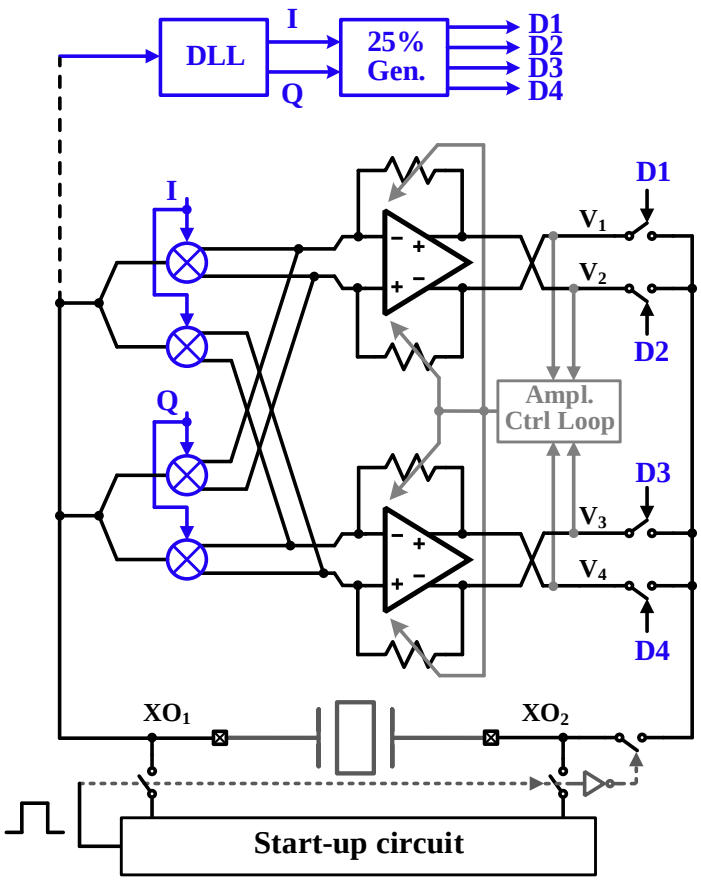

(a)

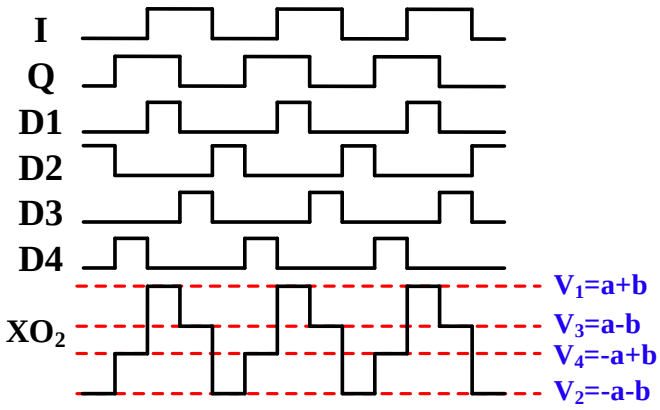

(b)

Figure 4.15: (a) Block diagram of the ULP XO (b) clock timing diagram.

The start-up circuit can simply be a Pierce-based sustaining amplifier [4, 5, 59], or a pre-energization technique based on the scheme described in Section 3.3. During start-up, the DLL and the biasing circuits get enough time to settle to their steady state to guarantee proper start-up and normal operation.

4.4.4 Effect of Nonidealities

In order to achieve the best performance, nonidealities of the system such as harmonic mixing, I/Q mismatch, and offset mismatch between TIAs should be considered carefully. In this section, the mechanism of the mentioned nonidealities is explained and their impact on the XO's overall performance is analyzed and quantified. As will be shown later, all the mentioned nonidealities contribute to a non-zero phase-shift around the crystal resonator that will eventually change the oscillation frequency. Therefore, before delving into the details of nonideality mechanisms, we take a look at the frequency stability of the XO as a function of the phase shift across the resonator.

4.4.4.1 Phase Response of a Second-Order, Underdamped System

In order to better understand and quantify the impact of random phase shift across the resonator, it is important to first characterize the phase-frequency response of a high-Q resonator such as a crystal. To a first degree, a high-Q resonator oscillating at its main oscillation mode can be modelled by a series RLC circuit with an impedance Z_m. it can be shown that

$$Z_m(j\omega) = R_m\Big[1 + jQ(\frac{\omega}{\omega_m} - \frac{\omega_m}{\omega})\Big] \tag{4.14}$$

where R_m, Q, and ω_m are the motional resistance, quality factor, and series resonance of the resonator, respectively. From (4.14), the phase shift of the resonator as a result of a frequency shift (and vice versa) can be calculated:

$$\Delta\phi = \angle Z_m(j\omega) = \arctan\Big[Q(\frac{\omega^2 - \omega_m^2}{\omega \cdot \omega_m})\Big] \tag{4.15}$$

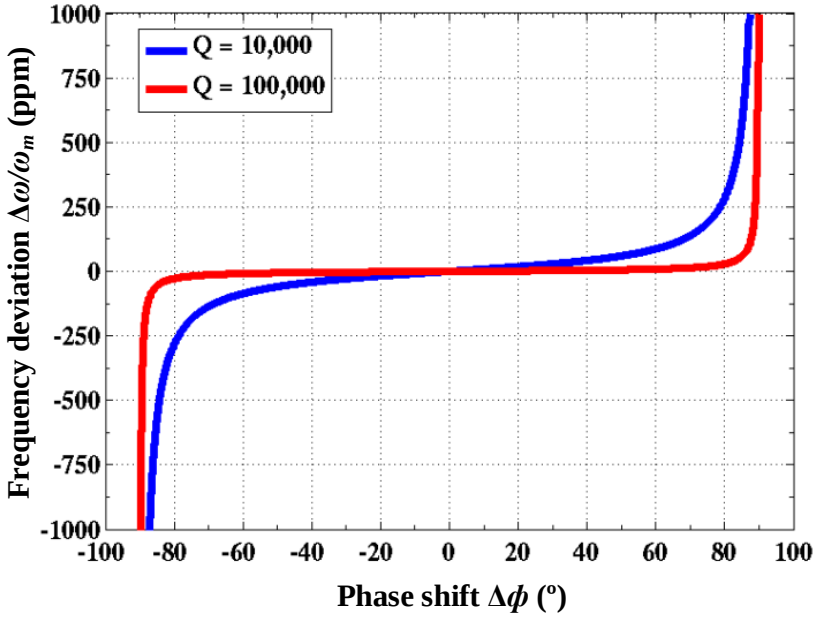

Figure 4.16: Frequency deviation of a high-Q resonator as a function of phase shift across it.

Figure 4.16 plots the frequency deviation of a resonator for two different quality factors of $Q = 10,000$ and $Q = 100,000$ as a function of the phase shift across the resonator according to (4.15). The amount of frequency deviation decreases with increasing the quality factor, as expected from (4.15).

Bode straight-line approximations give a very useful insight into the frequency variation of the amplitude and phase of a system without the need of complex calculations. Figure 4.17 plots the magnitude and phase response of the resonator as a function of frequency where straight-line Bode approximation is used. As seen, if the phase shift across the resonator is zero, the resonator will oscillate at its series resonance frequency, i.e., $\omega_O = \omega_m$. It can be shown that in case of a phase shift $\Delta\phi$, the oscillation frequency will shift according to

$$\frac{\Delta\omega}{\omega_m} = \frac{\omega_O - \omega_m}{\omega_m} \simeq 10^{\frac{1}{Q}\cdot\frac{\Delta\phi}{\pi}} - 1 \tag{4.16}$$

For small phase shifts in a high-Q resonator, i.e., the linear region in Fig. 4.16, (4.16) can be approximated by

$$\frac{\Delta\omega}{\omega_m} \simeq \frac{1}{Q}\cdot\frac{\Delta\phi}{\pi}\cdot\ln(10) \tag{4.17}$$

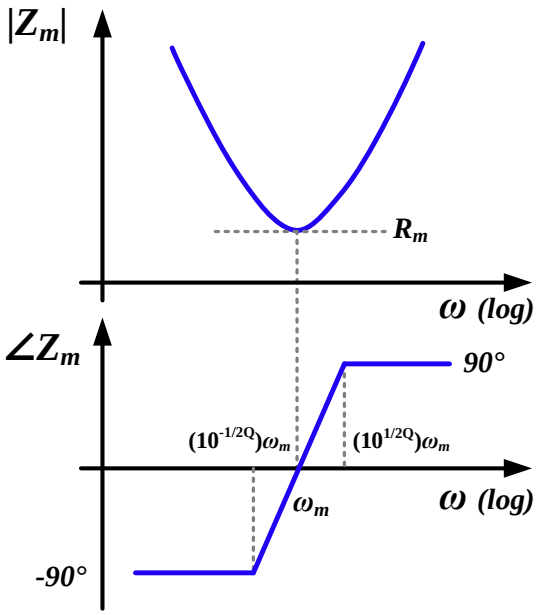

Figure 4.17: magnitude and phase of a high-Q resonator's impedance using straight-line phase approximation.

where the approximation $10^x \simeq 1 + x \cdot \ln(10)$ for $x \ll 1$ is used. According to (4.17), a phase shift of $\Delta\phi = \pm 5^\circ$ for a resonator with $Q = 10,000$ changes the frequency by about ± 6.4ppm, while it changes the frequency by only ± 0.64ppm if a crystal resonator with $Q = 100,000$ is used.

4.4.4.2 Effect of Harmonic Mixing

As mentioned in Section 4.4.2, the mixing operation is carried out by passive mixers that effectively multiply the oscillation signal by all the harmonics of the mixer driving signal. Even though the higher order harmonics resulting from the mixing are greatly suppressed by the small bandwidth of the TIAs and the high-Q resonator, the mixing artifacts at the oscillation frequency will not be attenuated by the resonator. The downconverting mixers in Fig. 4.10 generate a desired DC component as well as higher order frequency components resulted from harmonic mixing and calculated by (4.4) and (4.5) for the I and Q paths,

respectively. Assuming that the TIA only amplifies the desired DC component by R_f and the second harmonic by $K.R_f$ ($0 < K < 1$ with a phase shift of $-\phi_{TIA}$) while it sufficiently suppresses all the other harmonics, an artifact at the oscillation frequency will be generated as a result of the second harmonic mixing with the main and third harmonic of the I/Q signals at the upconverting mixers. The resultant output signal XO_2 is given by (4.8). Ignoring the $^K/_9$ term,

$$XO_2 = \frac{4}{\pi^2} I_m R_f \Big(\sin(\omega_O t + \theta) + K \sin(\omega_O t + \theta - \phi_{TIA}) \Big) \tag{4.18}$$

$$= \frac{4}{\pi^2} I_m R_f \sqrt{1 + K^2 + 2K\cos(\phi_{TIA})} \sin\Big(\omega_O t + \theta - \arctan(\frac{K\sin(\phi_{TIA})}{1 + K\cos(\phi_{TIA})})\Big)$$

Equation (4.18) shows that the limited second-harmonic rejection of the TIA slightly changes the loop gain and also causes the following phase shift across the resonator:

$$\Delta\phi = \arctan(\frac{K\sin(\phi_{TIA})}{1 + K\cos(\phi_{TIA})}) \tag{4.19}$$

Maximum phase shift happens for $\phi_{TIA} = 90°$, hence

$$\Delta\phi_{max} = \arctan(K) \tag{4.20}$$

Assuming a maximum tolerable phase shift of $\Delta\phi = \pm 5°$ (corresponding to a certain frequency deviation according to (4.17)), the second-harmonic rejection of the TIA has to be $K < 0.087$ which corresponds to 22dB attenuation of the second harmonic. This sets a limit for the maximum bandwidth of the TIA. For instance, a one-pole TIA has to have a bandwidth$< 0.16\omega_O$ to ensure more than 22dB attenuation at the second harmonic frequency.

It is also apparent from (4.18) that harmonic mixing also changes the loop gain. It can be shown that the minimum loop gain is

$$\begin{aligned} |T(j\omega_O)|_{min} &= \frac{4}{\pi^2} \cdot \frac{R_f}{R_m} \cdot \sqrt{1 + K^2 - 2K} \\ &= \frac{4}{\pi^2} \cdot \frac{R_f}{R_m} \cdot (1 - K) \end{aligned} \tag{4.21}$$

As seen from (4.21), the loop gain reduction is minimal especially since K is usually much smaller than one ($K << 1$). Nevertheless, as long as (4.21) satisfies the Barkhausen gain criterion, i.e, (4.10), it will not degrade the XO performance.

4.4.4.3 Effect of I/Q Phase Mismatch

Another source of error is the phase mismatch of the I/Q outputs (from 90°) of the delay-locked loop. Assuming there is a mismatch of δ between the I and Q signals in Fig. 4.11, i.e., $I = \text{sgn}\Big(\sin(\omega_O t + {}^{\delta}\!/_{2})\Big)$ and $Q = \text{sgn}\Big(\cos(\omega_O t - {}^{\delta}\!/_{2})\Big)$, and only considering the main frequency component,

$$i_I = \frac{1}{\pi} I_m \Big(\cos(\theta - {}^{\delta}\!/_{2}) + \cdots\Big) \tag{4.22}$$

$$i_Q = \frac{1}{\pi} I_m \Big(\sin(\theta + {}^{\delta}\!/_{2}) + \cdots\Big) \tag{4.23}$$

Consequently,

$$XO_2 = \frac{4}{\pi^2} I_m R_f \Big(\sin(\omega_O t + \theta) + \sin(\delta)\cdot\cos(\omega_O t - \theta)\Big) \tag{4.24}$$

$$= \frac{4}{\pi^2} I_m R_f \sqrt{1 + \sin^2(\delta) + 2\delta\sin(2\theta)}\cdot\sin\Big(\omega_O t + \frac{\pi}{2} - \arctan\big(\frac{\sin(\delta)\sin(\theta) + \cos(\theta)}{\sin(\delta)\cos(\theta) + \sin(\theta)}\big)\Big)$$

As seen in (4.24), the I/Q phase mismatch creates a sinusoid at the oscillation frequency that changes the loop gain and the phase shift across the resonator. We can show that the minimum loop gain for $\delta << 1$ is

$$\begin{aligned} |T(j\omega_O)|_{min} &= \frac{4}{\pi^2}\cdot\frac{R_f}{R_m}\cdot\sqrt{1 + \delta^2 - 2\delta} \\ &= \frac{4}{\pi^2}\cdot\frac{R_f}{R_m}\cdot(1 - \delta) \end{aligned} \tag{4.25}$$

The effect of I/Q phase mismatch on the loop gain reduction is minimal according to (4.25). For small values of phase mismatch ($\delta << 1$), the phase shift across the resonator is approximately equal to δ, i.e. $\Delta\phi \simeq \delta$.

4.4.4.4 Effect of Offset Voltage of TIAs

Mismatches in the TIA circuits introduce input-referred offsets in the I and Q paths, namely $V_{OS,I}$ and $V_{OS,Q}$. Taking into account the effect of offsets in Fig. 4.11,

$$V_a = \frac{1}{\pi} I_m R_f \cos(\theta) + V_{OS,I} \tag{4.26}$$

$$V_b = \frac{1}{\pi} I_m R_f \sin(\theta) + V_{OS,Q} \tag{4.27}$$

Finally the crystal driving signal XO_2 is

$$XO_2 = \frac{4}{\pi}\Big(\frac{1}{\pi} I_m R_f \sin(\omega_O t + \theta) + V_{OS,I} \sin(\omega_O t) + V_{OS,Q} \cos(\omega_O t)\Big) \tag{4.28}$$

Therefore, the following has to be satisfied by design to minimize the impact of the offset voltage:

$$\sqrt{V_{OS,I}^2 + V_{OS,Q}^2} << \frac{1}{\pi} I_m R_f \tag{4.29}$$

Offset voltage can be greatly reduced by using large input devices in the opamp and a proper layout. Since the opamps do not require a large bandwidth, large input devices can be used to minimize the offset voltage and satisfy (4.29).

4.4.5 Circuit Implementation

This section goes over the different circuit blocks needed to implement the proposed ULP XO shown in Fig. 4.15.

4.4.5.1 Ultra-low power PTAT Bias Generation

One of the main challenges in low-power circuit design is the generation of robust bias circuitry. A proportional-to-absolute-temperature (PTAT) current source is used in this work to bias the opamps. This is to ensure that the opamps maintain a constant-g_m over temperature. Figure 4.18(a) shows a common implementation of a PTAT current source,

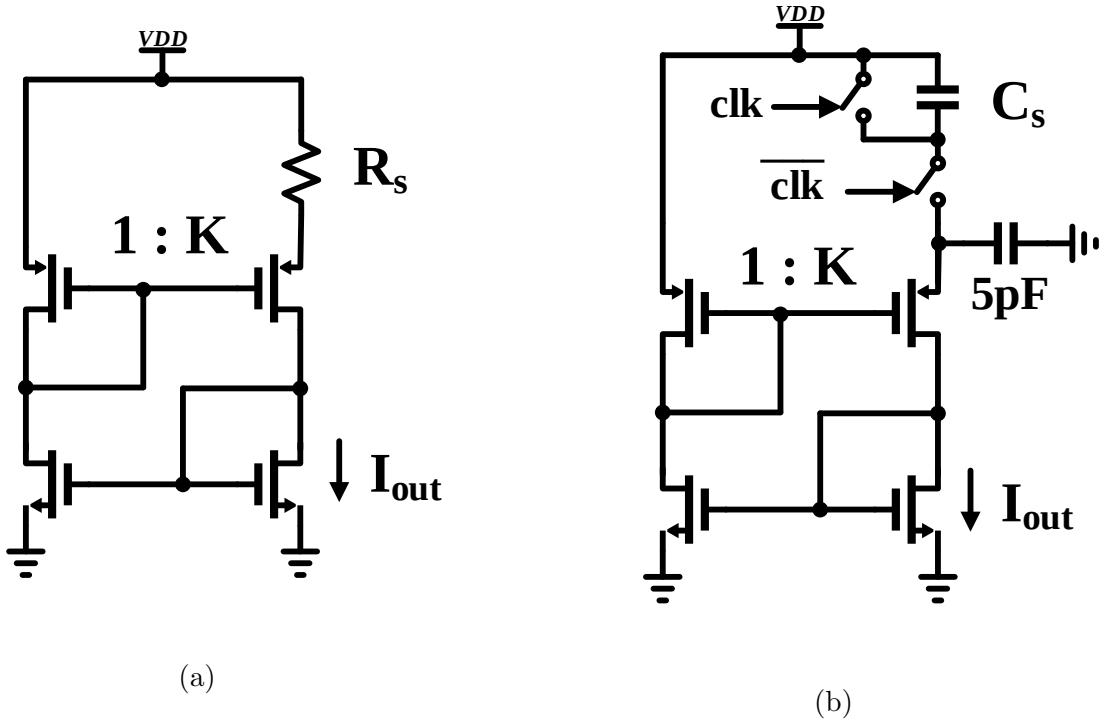

Figure 4.18: (a) Conventional PTAT current source (b) Ultra-low power PTAT current source.

where the gate-source voltage difference of two PMOS transistors is put across the resistor R_S. Consequently, the output current is

$$I_{out} = \frac{\Delta V_{gs}}{R_S} \simeq \frac{\phi_t \cdot \ln(K)}{R_S} \tag{4.30}$$

where ϕ_t is the thermal voltage and K is the ratio of the PMOS transistor sizes. In order to generate a low current of 10pA at room temperature, (4.30) states that a huge resistor of 1.8GΩ is required which is not feasible. So, the problem with this structure is that it is not applicable to ultra-low current generation.

To solve the mentioned issue, we took advantage of the fact that we have a very stable clock frequency available to us and replaced the resistor with a switched-capacitor circuit as shown in Fig. 4.18(b). By substituting R_S in (4.30) with the equivalent resistance of the switched-capacitor circuit ($^1/_{f_{clk}C_S}$), we arrive at the following equation for the output

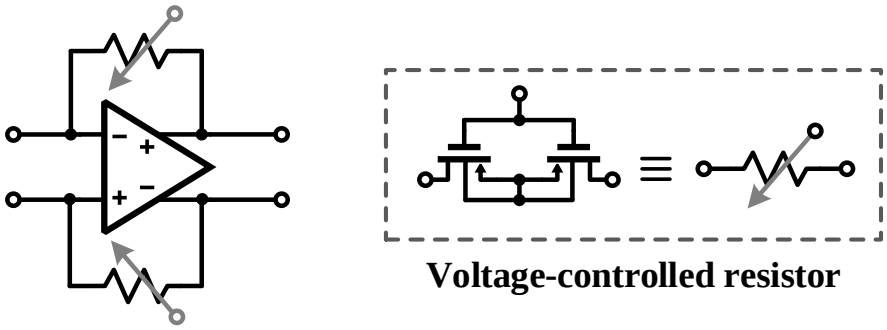

Figure 4.19: Trans-impedance amplifier with voltage-controlled feedback resistor to control the gain.

current,

$$I_{out} = f_{clk} \cdot C_S \cdot \phi_t \cdot \ln(K) \tag{4.31}$$

Clocked by the crystal oscillator's accurate 32kHz signal, Fig. 4.18(b) generates currents as low as 10pA without requiring any bulky/off-chip components. The 5pF capacitor is added to shunt the high-frequency components resulting from switching to ground. Furthermore, since the absolute value of integrated capacitors is more tightly controlled with a much smaller temperature coefficient than that of resistors, this technique provides a higher accuracy compared to Fig. 4.18(a) [60].

4.4.5.2 Trans-Impedance Amplifier (TIA)

The DC output current of the current-commutating mixers is amplified by a trans-impedance amplifier (TIA). The architecture of the TIA is shown in Fig. 4.19, where voltage-controlled feedback resistors are used to control the gain of the TIA. As will be discussed later, a variable TIA gain is necessary to control the oscillation amplitude. The voltage-controlled resistors are implemented by using two PMOS transistors in series that operate in triode region.

The TIA consists of a ULP, low-voltage opamp that operates from a 0.5V supply and only consumes 50pW. Figure 4.20 shows the opamp architecture. As mentioned in Section 4.4.5.1,

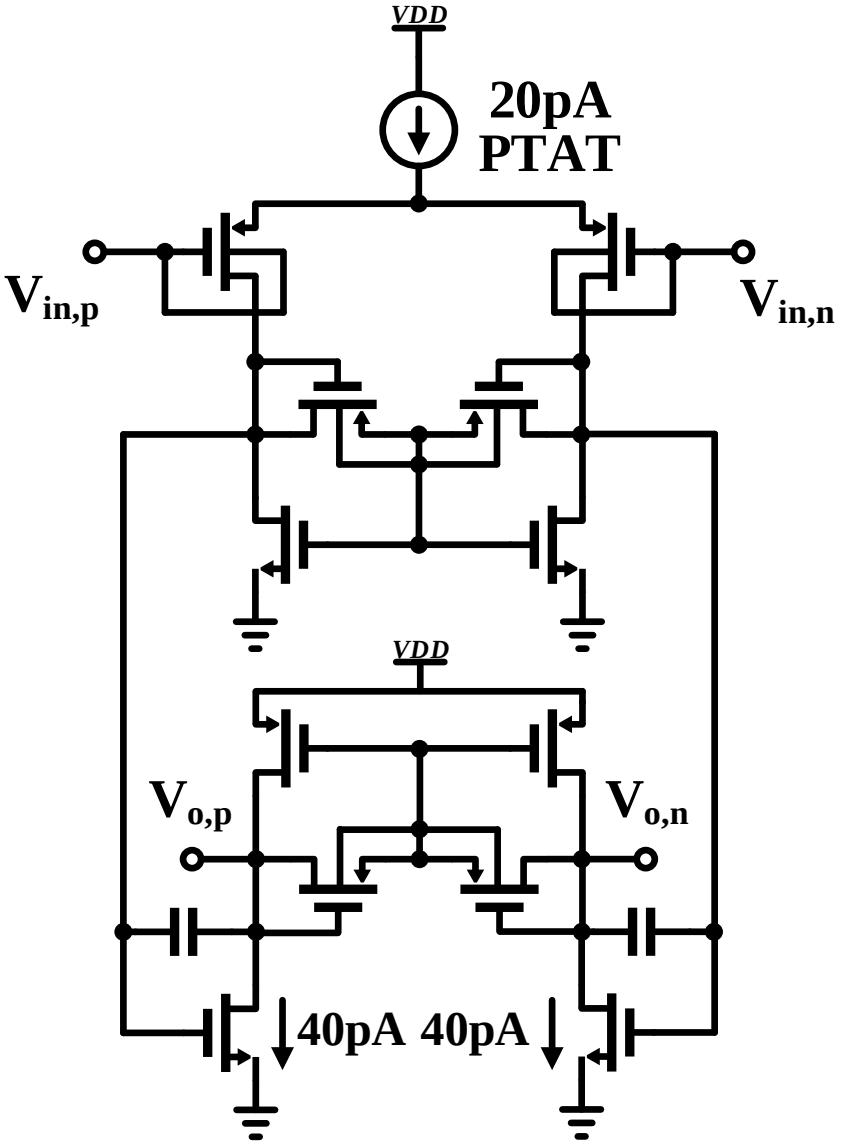

Figure 4.20: Ultra-low power, low-voltage opamp.

the opamp is biased by a PTAT current source to ensure a constant-g_m over temperature. In order to make the opamp compatible with the low supply voltage of only 0.5V, the bulks of the input PMOS pair are connected to their corresponding gates to reduce the threshold voltage. Since the devices always operate in the subthreshold region, the source/drain junction diodes remain reverse-biased at all times. Furthermore, since only a small bandwidth is needed, large input devices are used to minimize the offset voltage and mismatch between the I/Q TIAs.

As shown in Fig. 4.20, pseudo-resistors are used to set the output common-mode voltage of both stages. It also helps to maximize the DC gain.

4.4.5.3 Amplitude Control Loop

Amplitude control loops are widely used in crystal oscillators to control the oscillation amplitude by reducing the nonlinearity and improving the frequency stability. As shown in Fig. 4.15(a), an amplitude control loop can be realized by comparing the maximum value of V_1 through V_4 with a reference voltage and adjusting the TIA gain accordingly. The TIA gain is varied through the voltage-controlled feedback resistors shown in Fig. 4.19. The maximum value of V_1 through V_4 is computed using three low switching activity voltage comparators with negligible power consumption as shown in Fig. 4.21.

4.4.5.4 Delay-Locked Loop

As mentioned in Section 4.4.3, a delay-locked loop (DLL) is used to extract the 90° out-of-phase I/Q signals from the oscillation signal. The DLL implementation is shown in Fig. 4.22(a). A ULP open-loop opamp is used to convert the XO_1 output to a differential signal. To have a well-defined common-mode voltage at the opamp input, XO_1 is AC-coupled and diode-connected NMOS devices are used to set the input voltage. The differential signal is then fed to a two-stage current-controlled delay line. The amount of delay in the delay cells is controlled by the shown charge pump such that it generates quadrature outputs. The charge pump is implemented using a servo loop [61] to ensure equal up and down current

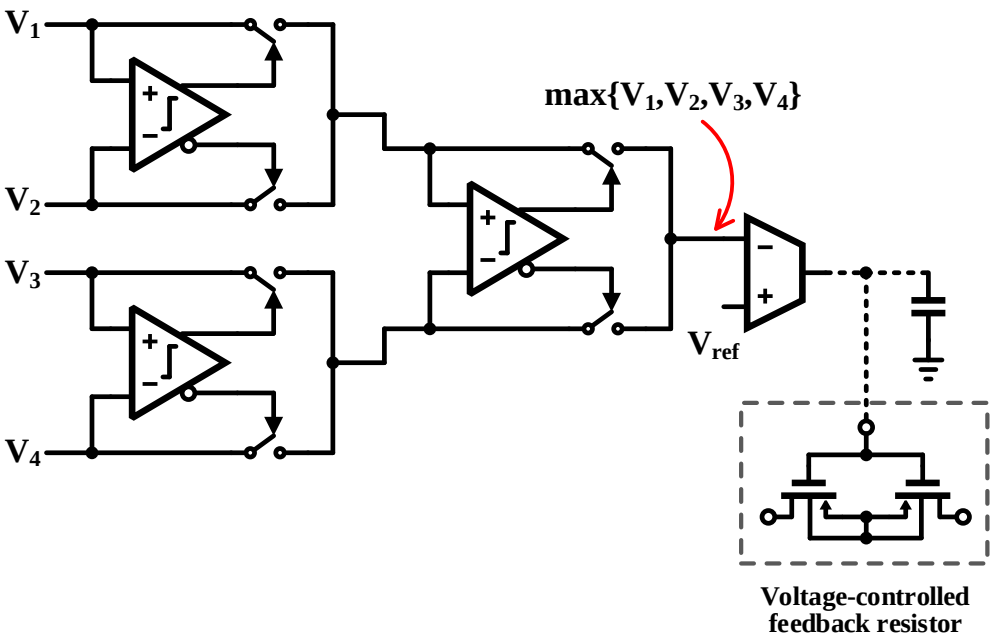

Figure 4.21: Amplitude control loop.

with minimal mismatch. Another advantage of this charge pump topology is that the opamp does not need to provide a fast response as it is in a closed-loop configuration at all times [42]. This allows of using an ultra-low power opamp.

The simulated transient response of the DLL control voltage, V_{ctrl}, is plotted in Fig. 4.22(b). As seen, the DLL settles to its steady state in 13ms that is well within the XO start-up time of about 0.2s to ensure proper start-up and steady-state operation. Typically an output buffer is required to drive the system with the crystal oscillatory signal. To reduce the power consumption of the output buffer, the rail-to-rail swing at either I/Q signals can be taken as the XO final output.

4.4.5.5 25%-Duty-Cycle Clock Generation

As mentioned in Section 4.4.3, non-overlapping 25%-duty-cycle signals, D_1 through D_4, are used to implement the addition function of the I/Q paths while avoiding the power-hungry output adder of Fig. 4.10. As shown in the block diagram of Fig. 4.15, signals D_1 through

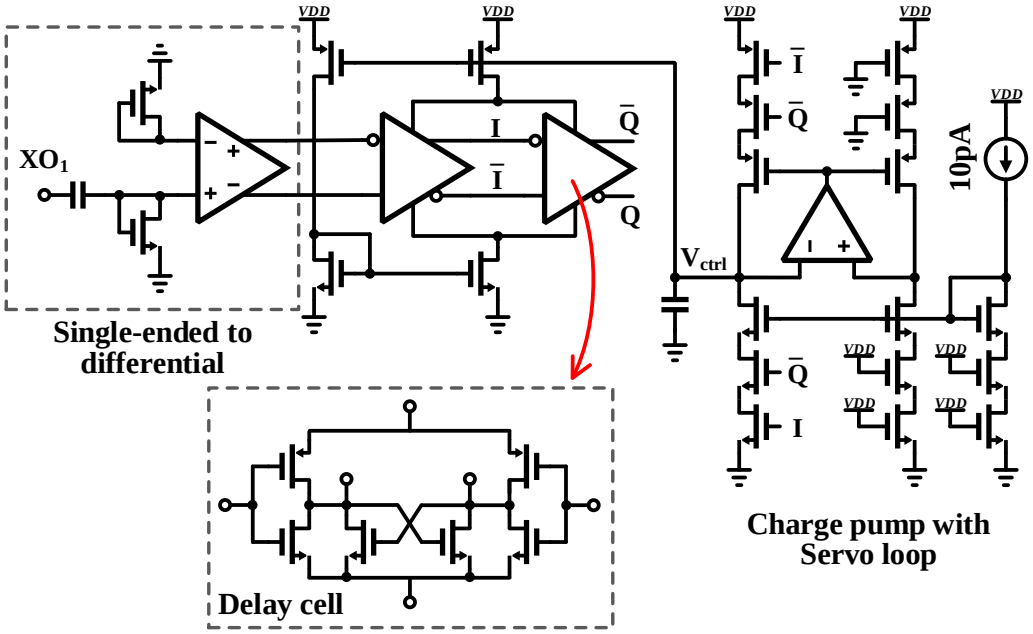

(a)

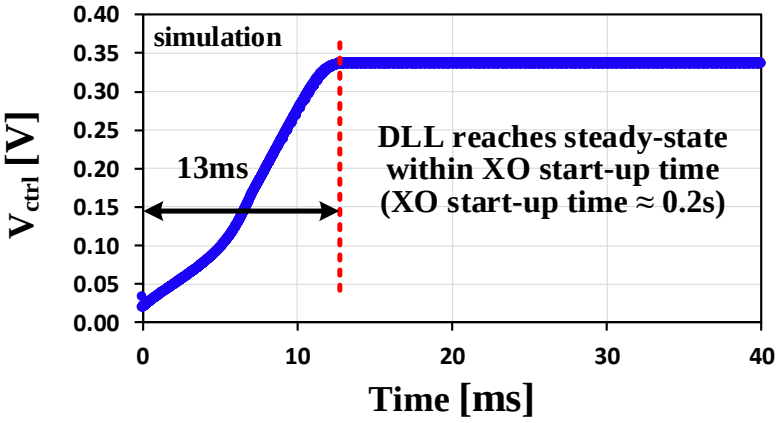

(b)

Figure 4.22: (a) Delay-locked loop implementation (b) simulated transient response of DLL.

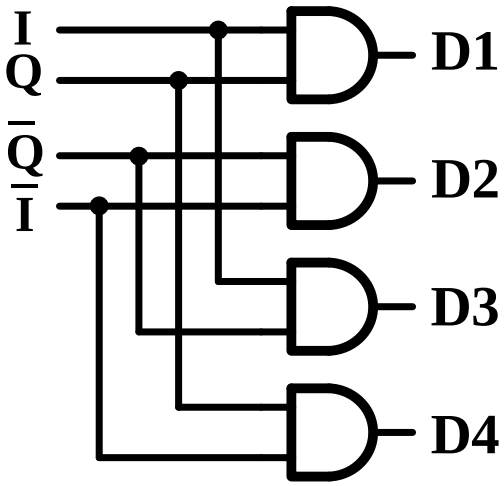

Figure 4.23: 25%-duty-cycle clock generation circuit.

D_4 are extracted from the I/Q outputs of the DLL. A simple logic implementation is used to generate the 25%-duty-cycle signals as shown in Fig. 4.23.

4.4.6 Measurement Results

As a proof-of-concept, a prototype IC of the proposed ULP 32kHz XO was fabricated in TSMC 65nm standard CMOS technology. The test board along with the die micrograph is shown in Fig. 4.24. The active core area is 0.027mm^2.

Measuring ultra-low current values is not trivial and requires delicate considerations. Hence, before delving into the detail of the measurement results, we discuss the measurement setup first. Figure 4.25 depicts the measurement setup used to measure few pAs of currents. Since voltages can be readily measured with a higher accuracy, the idea in Fig. 4.25 is to convert the supply current to a DC voltage and then measure the DC voltage to calculate the current consumption. To do so, the supply current is passed through a TIA that comprises a precision amplifier from Texas Instruments (LMP7721). The precision amplifier has about only 3fA input bias current with very low input offset voltage. To minimize the current

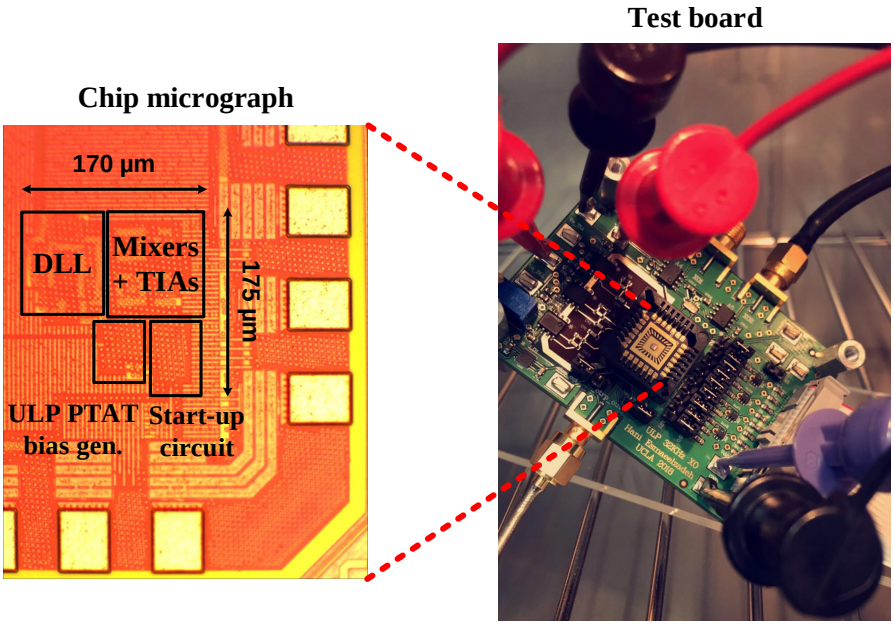

Figure 4.24: ULP XO test board and the chip micrograph.

leakage, all the sensitive PCB traces are surrounded by a guard trace that has the same potential as the supply voltage, i.e., 0.5V. To further reduce the DC current leakage on PCB, a constant-potential island is formed around the sensitive areas as shown in Fig. 4.26. The constant-potential island is at the same potential as the supply voltage and extends to all the PCB layers. All the measurements were carried out in a chamber with controlled temperature and minimal interferences.

Figure 4.27 shows the measured power consumption and frequency deviation of the proposed ULP 32kHz XO over temperature from -20°C to 80°C (at $V_{DD} = 0.5V$). The measurements were performed across 20 different dies. At room temperature, the power consumption averaged across 20 measurements is 0.55nW with a worst-case of 0.7nW. Measured frequency deviation is within 80ppm over temperature.

Figure 4.28 shows the measured power consumption and frequency deviation of the proposed ULP 32kHz XO under supply voltage variations from 0.4V to 0.9V (at 25°C). The average power consumption at a high supply voltage of 0.9V is about 2nW, and the line sensitivity is about 13ppm/V.

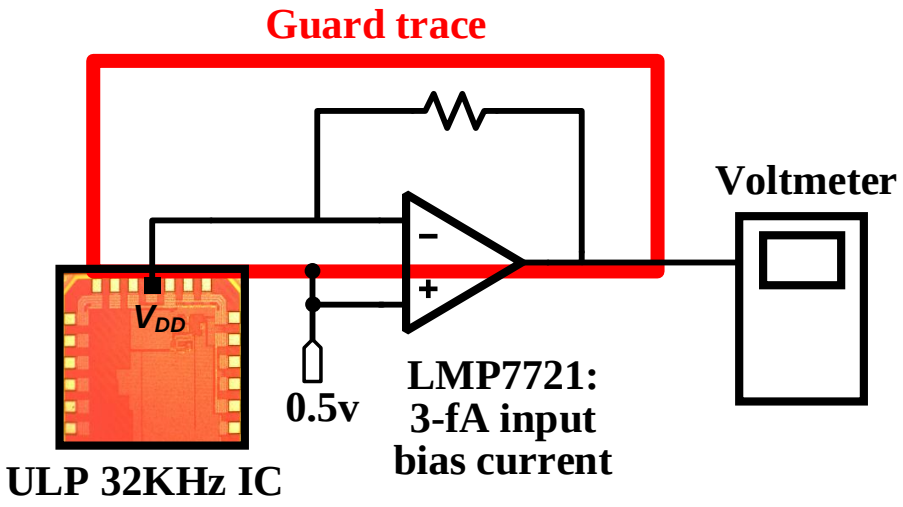

Figure 4.25: Ultra-low current measurement setup.

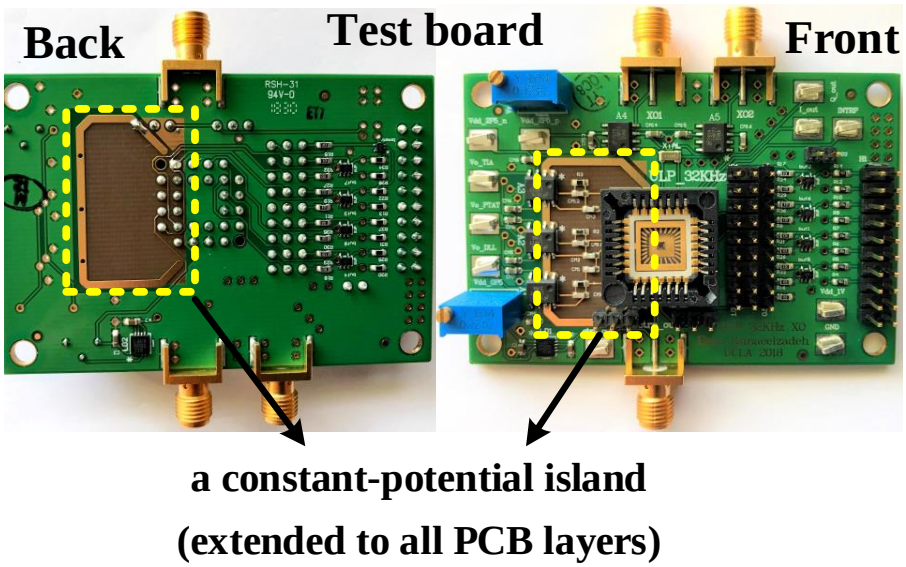

Figure 4.26: Test board: all sensitive traces are surrounded by an equal-potential guard ring/plane (on all PCB layers) to minimize leakage.

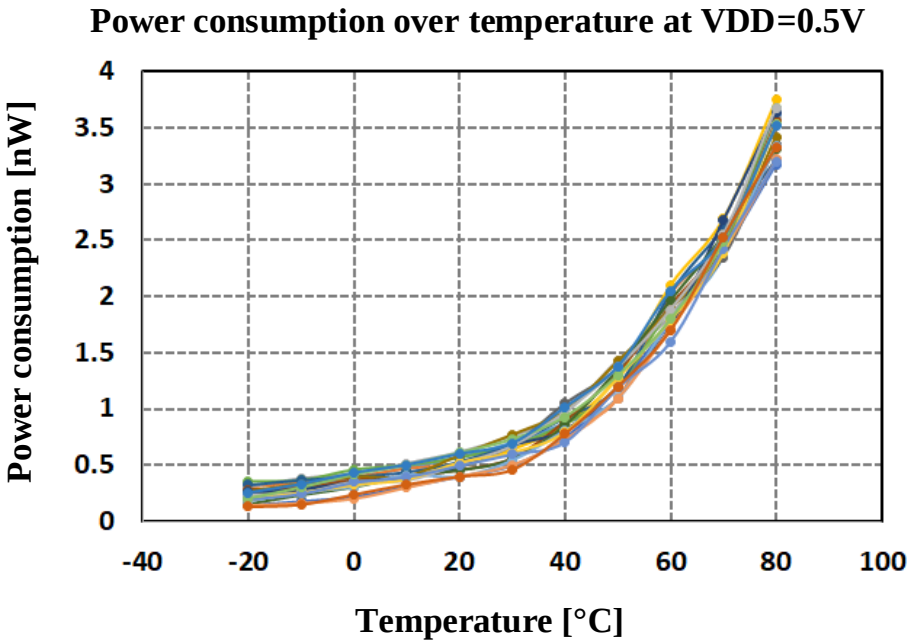

(a)

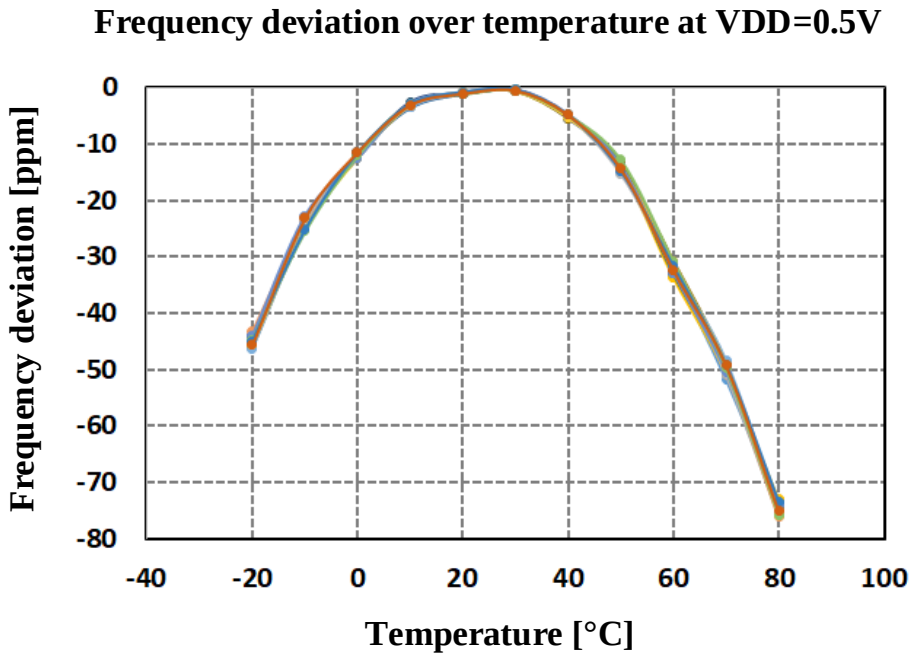

(b)

Figure 4.27: Measurement results for 20 dies: (a) power consumption and (b) frequency variations over temperature.

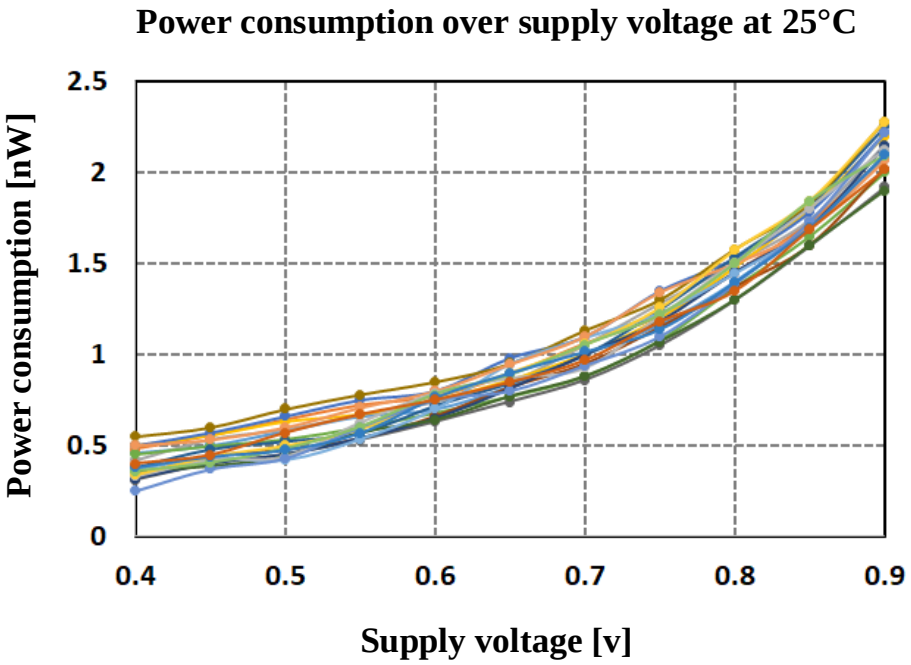

(a)

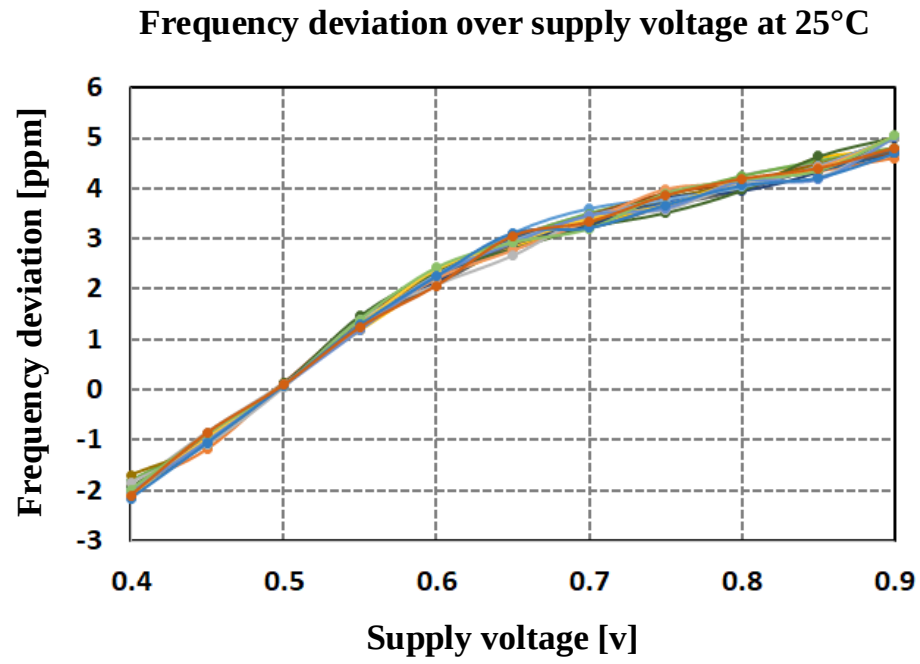

(b)

Figure 4.28: Measurement results for 20 dies: (a) power consumption and (b) frequency variations over supply voltage.

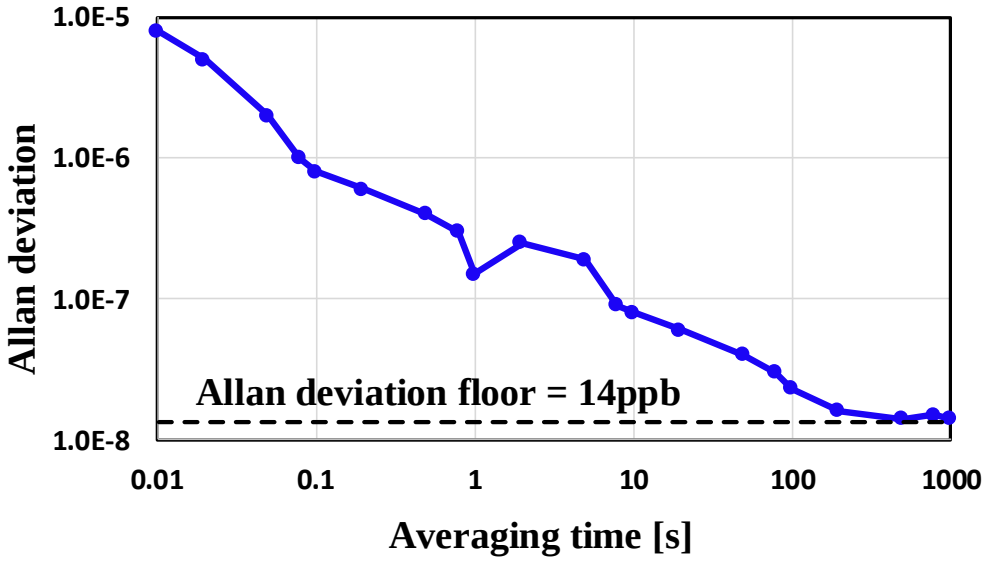

Figure 4.29: Measured Allan deviation.

For sleep timers, the long-term variation of the timing noise is important and is typically characterized by the Allan deviation. Figure 4.29 plots the measured Allan deviation for one die. The measured Allan floor shows that the long-term frequency stability of the XO is better than 14ppb.

To verify the robustness of the proposed XO to mismatches between the I/Q paths, intentional errors were introduced between I and Q phases using an external clock generator. Figure 4.30 shows the deviation of the oscillation frequency as a result of the intentional I/Q phase mismatch (from 90°). The frequency deviation is minimal (±0.6ppm within ±5°), as the high-Q resonator only has to be slightly pulled off resonance to compensate for the phase mismatch.

Figure 4.31 shows the power contribution of the main circuit blocks. Unlike the commonly-used Pierce oscillator where the sustaining amplifier consumes more than 85% of the power, the DC opamps in the proposed XO only contribute ∼14%. Most of the power consumption is coming from the DLL, the mixers' gate drivers, and the 25%-duty-cycle clock generator that are mostly digital and scale well with CMOS technology.

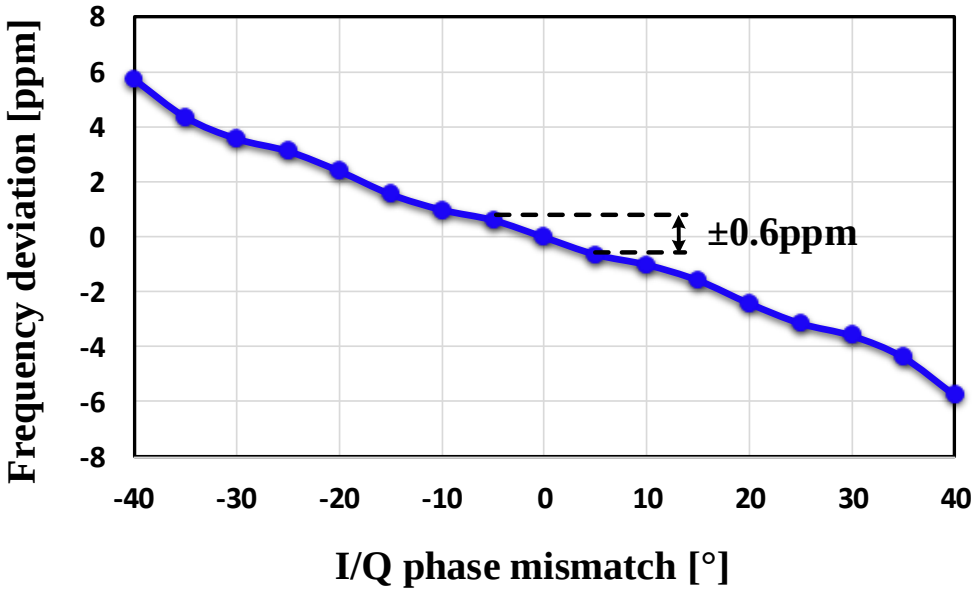

Figure 4.30: Measured sensitivity of the oscillation frequency to intentionally-introduced mismatch in the I/Q phase using external signal generators.

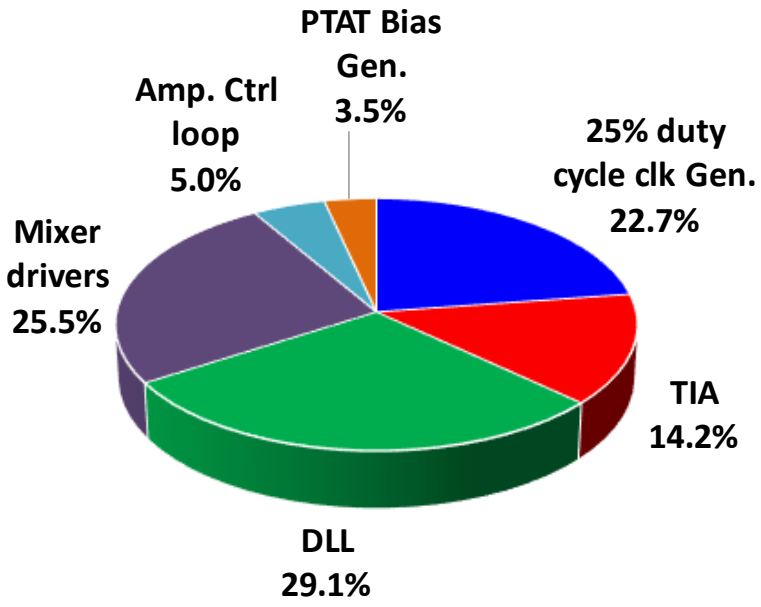

Figure 4.31: Power contribution of main blocks of the ULP 32kHz XO.

Table 4.1: Performance summary and comparison with state-of-the-art 32kHz XOs

	This work* (ISSCC'19)	VLSI'17 [5]	JSSC'16 [59]	ISSCC'14 [4]	JSSC'16 [3]
Technology (nm)	65	55	180	28	180
Area (mm^2)	0.027	0.16	0.3	0.03	0.062
Supply voltage (V)	0.5	0.5	1.2	0.2	0.3
Power consumption at 25°C (nW)	0.55	1.7	5.58	5.0	1.5
Temperature stability (ppm)	80 (-20°C to 80°C)	109 (-20°C to 80°C)	133 (-20°C to 80°C)	50 (-20°C to 80°C)	150 (0°C to 80°C)
Line sensitivity (ppm/V)	13.0	6.7	30.3	85.0	7.0
Allan deviation (ppb)	14	25	10	10	70
Calibration required	NO	YES	YES	NO	YES

*Averaged results across 20 dies with a worst-case power consumption of 0.55nW.

Table 4.1 summarizes the performance of the proposed XO and compares it with other state-of-the-art 32kHz XOs. As can be seen, the proposed oscillator only consumes 0.55nW, which is ∼2.7x lower than the best case in prior art. Furthermore, the proposed architecture does not need calibration and multiple supplies, unlike most prior art [3, 5, 59].

CHAPTER 5

Conclusion

This work focused on energy-efficient clock generation for ultra low power applications. Both the proposed quick start-up technique and the ULP sleep timer reduce the average power consumption of duty-cycled systems by reducing the sleep power consumption as well as the active power consumption. Here is a summary of the main contributions of this research:

This work presented a novel precisely-timed energy injection technique to speed up the start-up behavior of high-Q oscillators. The proposed solution is also insensitive to the frequency variations of the injection signal over a wide enough range called the "tolerable injection frequency error". This enables the use of integrated, temperature-compensated oscillators as the injection signal. The TIFE is analytically derived and proven that it is independent of the Q factor for high-Q resonators. A theoretical analysis is carried out to calculate the optimal injection duration.

As a proof-of-concept, the proposed quick start-up technique is incorporated in the design of crystal oscillators and is realized in a TSMC 65nm CMOS technology. To verify the robustness of our technique across resonator parameters and frequency variations, six crystal resonators from different manufacturers with different packagings and Q factors were tested. The implemented IC includes multiple crystal oscillators at 1.84MHz, 10MHz, and 50MHz frequencies, with measured start-up times of 58μs, 10μs, and 2μs, while consuming 6.7μW, 45.5μW, and 195μW at steady state, respectively. To the authors' best knowledge, this is the fastest, reported start-up time in the literature, with >15x improvement over prior art, while requiring the smallest start-up energy ($\sim$12nJ).

In order to further extend the frequency insensitivity range (TIFE) in Fig. 3.18(b), a dynamically-adjusted injection duration, instead of using a constant value, was proposed.

The optimal dynamic injection duration as a function of injection frequency was analytically derived. In this manner, as the injection frequency deviates beyond the "insensitive region", the start-up time is reduced to its minimum value by appropriately changing the injection duration T_{inj}.

A combination of the precisely-timed injection with the chirped injection technique was proposed to further relax the frequency stability requirement of the injection oscillator. In this technique, the energy injection happens over different frequency steps. The duration of each frequency step is chosen to be equal to the optimal injection duration of a single-tone injection. With each frequency step covering a TIFE of about ±7500ppm, a much wider overall TIFE can be achieved by the multiple injection steps.

A new ultra low power oscillator architecture was introduced as part of this research that reduced the power consumption of a 32KHz sleep timer to about 0.55nW drawn from a 0.5V supply. The ultra low power consumption is achieved by amplifying the oscillation signal at DC by means of downconverting and upconverting passive mixers. By amplifying the oscillation signal at DC, our proposed architecture eliminated the minimum transconductance requirement of conventional oscillators and lead to an ULP operation. Furthermore, our technique realized a series resonance oscillator by employing an I/Q frequency conversion technique. Doing so improved the frequency stability of the oscillator without requiring large load capacitors which further improved the power efficiency of our oscillator architecture.

Measurements performed across 20 different standard CMOS dies showed an average power consumption of 0.55nW at 32KHz with a worst-case measured power consumption of 0.7nW at room temperature. The measured power consumption of the proposed oscillator is about 2.7 times lower than the best case in prior art. At a high power supply of 0.9V, the oscillator consumes an average power consumption of about 2nW. The line sensitivity of the oscillator was measured to be 13ppm/V. The measured long-term frequency stability of the oscillator, indicated by the Allan deviation floor, is 14ppb. Unlike most prior art, the proposed oscillator in this work does not require any calibration schemes and/or multiple supply domains.

Appendix A

Derivation of high-Q oscillator's motional current envelope

Based on developing an analytic signal, the analysis in [62] states that the envelope of an arbitrary signal $i_m(t)$ is

$$i_{m,env}(t) = 2 \cdot \left| \frac{1}{2\pi} \int_{-\infty}^{+\infty} I_{m+}(j\omega) \cdot \mathrm{e}^{j\omega t} \, \mathrm{d}\omega \right| \tag{A.1}$$

where $I_{m+}(j\omega) = \mathscr{F}\{i_m(t)\}$ for $\omega > 0$. In case of the circuit shown in Fig. 3.6,

$$i_{m,env}(t) = 2 \cdot \left| \frac{1}{2\pi} \int_{-\infty}^{+\infty} V_{inj+}(j\omega) \cdot H_+(j\omega) \cdot \mathrm{e}^{j\omega t} \, \mathrm{d}\omega \right| \tag{A.2}$$

where $I_{m+}(j\omega) = V_{inj+}(j\omega) \cdot H_+(j\omega)$ is used. Based on the fact that $H_+(j\omega)$ is a very high-Q filter centered at $\omega = \omega_m$,

$$i_{m,env}(t) = \left| V_{inj+}(j\omega_m) \right| \cdot \left| \frac{1}{\pi} \int_{-\infty}^{+\infty} H_+(j\omega) \cdot \mathrm{e}^{j\omega t} \, \mathrm{d}\omega \right| \tag{A.3}$$

Note that the second term in (A.3) is equal to the envelope of $h(t)$, hence

$$i_{m,env}(t) = \left| V_{inj+}(j\omega_m) \right| \cdot h_{env}(t) \tag{A.4}$$

$h_{env}(t = T_{inj})$ is a very slow-moving function over time that can be readily calculated as

$$h_{env}(t = T_{inj}) = \frac{1}{L_m} \cdot \mathrm{e}^{-T_{inj}/\tau} \tag{A.5}$$

where $\tau = 2Q/\omega_m$ is the time-constant of the circuit.

Now, let us consider the case of injecting a single tone, i.e. $v_S(t) = V_{inj} \cdot \cos(\omega_{inj} t)$. As should be noted in Fig. 3.1(b), the injection signal, in the frequency domain, is the convolution of the applied single tone with a sinc function. Hence,

$$\left| V_{inj+}(j\omega) \right| = \frac{T_{inj} \cdot V_{inj}}{2} \cdot \left| \mathrm{sinc} \left[\frac{T_{inj}}{2} (\omega_{inj} - \omega) \right] \right| \tag{A.6}$$

The envelope of the motional current at the end of injection duration given by (3.4) is now readily proved by substituting (A.5) and (A.6) in (A.4):

$$i_{m,env}(T_{inj}) = \frac{T_{inj} \cdot V_{inj}}{2L_m} \cdot \left| \text{sinc}\left[\frac{T_{inj}}{2} \cdot \Delta\omega_{inj}\right]\right| \cdot \text{e}^{-T_{inj}/\tau} \tag{A.7}$$

Equation (A.7) can be further simplified by substituting the sinc function with its following Taylor series:

$$\text{sinc}(x) = \frac{\sin(x)}{x} = 1 - \frac{x^2}{3!} + \frac{x^4}{5!} - \cdots \tag{A.8}$$

Assuming $T_{inj} \ll \tau$ and $T_{inj} \cdot |\Delta\omega_{inj}| \ll 2$, and using the Taylor series of the sinc function given in (A.8), the envelope of the motional current at the end of injection duration is

$$i_{m,env}(T_{inj}) \simeq \frac{T_{inj} \cdot V_{inj}}{2L_m} \cdot \left(1 - \frac{(\Delta\omega_{inj} \cdot T_{inj})^2}{24}\right) \tag{A.9}$$

Appendix B

Time-domain derivation of oscillator's motional current

Consider a high-Q resonator modeled by its series RLC network as shown in Fig. B.1. The resonator is driven by an injection signal of $v_{inj}(t) = V_{inj}.\cos(\omega_{inj}t)$. It can be shown that the laplace transform of the transfer function is

$$H(s) = \frac{I_m(s)}{V_{inj}(s)} = \frac{1}{R_m[1 + Q.(\frac{s}{\omega_m} + \frac{\omega_m}{s})]} \tag{B.1}$$

where $\omega_m = {}^{1}/_{\sqrt{L_m C_m}}$ is the resonator's series resonance frequency and $Q = {}^{L_m\omega_m}/_{R_m} = {}^{1}/_{R_m C_m \omega_m}$ is the resonator's quality factor. Using laplace inverse, the time-domain transfer function is

$$h(t) = \frac{\omega_m}{2Q^2 R_m}[2Q\cos(\omega_m t) - \sin(\omega_m t)]\mathrm{e}^{-t\frac{\omega_m}{2Q}}\,\mathrm{u}(t) \tag{B.2}$$

Assuming $Q \gg 1$,

$$\begin{aligned} h(t) &\simeq \frac{\omega_m}{QR_m}\cos(\omega_m t)\mathrm{e}^{-t\frac{\omega_m}{2Q}}\,\mathrm{u}(t) \\ &= \frac{1}{L_m}\cos(\omega_m t)\mathrm{e}^{-t\frac{\omega_m}{2Q}}\,\mathrm{u}(t) \end{aligned} \tag{B.3}$$

Using convolution and assuming $i_m(t = 0) = 0$, the motional current flowing into the resonator is found as follows

$$i_m(t) = \frac{V_{inj}}{L_m}\int_0^\infty \cos(\omega_m \tau)\mathrm{e}^{-\tau\frac{\omega_m}{2Q}}\cos\Big(\omega_{inj}(t-\tau)\Big)\,\mathrm{d}\tau \tag{B.4}$$

According to (B.4), if $\omega_{inj} = \omega_m$ and $Q \gg 1$,

$$i_m(t) \simeq \frac{V_{inj}}{R_m}(1 - \mathrm{e}^{-t\frac{\omega_m}{2Q}})\cos(\omega_m t) \quad \omega_{inj} = \omega_m \tag{B.5}$$

The envelope of the motional current has the shape of a first-order response and is equal to

$$i_{m,env}(t) = \frac{V_{inj}}{R_m}(1 - \mathrm{e}^{-t\frac{\omega_m}{2Q}}) \qquad \omega_{inj} = \omega_m \tag{B.6}$$

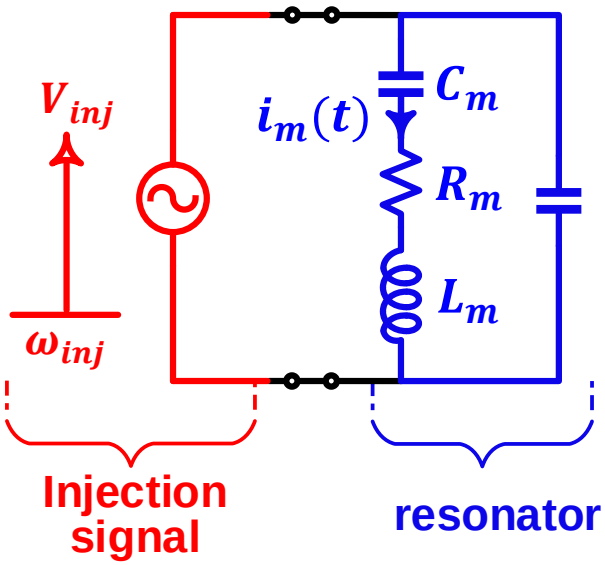

Figure B.1: A high-Q resonator driven by an injection signal.

However, a more interesting and practical case is when $\omega_{inj} \neq \omega_m$,

$$\begin{aligned} i_m(t) =& \frac{V_{inj}.\omega_m}{R_m.Q^2.(\omega_{inj}^2 - \omega_m^2)^2} \\ & \times \Big[Q.\omega_{inj}(\omega_{inj}^2 - \omega_m^2)\sin(\omega_{inj}t) \\ & + \omega_{inj}^2.\omega_m \cos(\omega_{inj}t) \\ & - Q.\omega_m.(\omega_{inj}^2 - \omega_m^2)\mathrm{e}^{-t\frac{\omega_m}{2Q}} \sin(\omega_m t) \\ & - \omega_{inj}^2.\omega_m \mathrm{e}^{-t\frac{\omega_m}{2Q}} \cos(\omega_m t) \Big] \quad \omega_{inj} \neq \omega_m \end{aligned} \tag{B.7}$$

For $Q \gg 1$ $\left(\text{more precisely: } Q \gg \frac{\omega_{inj}.\omega_m}{\omega_{inj}^2 - \omega_m^2} \simeq \frac{\omega_m}{2(\omega_{inj} - \omega_m)}\right)$,

$$\begin{aligned} i_m(t) =& \frac{V_{inj}}{L_m(\omega_{inj}^2 - \omega_m^2)} \\ & \times \Big[\omega_{inj}.\sin(\omega_{inj}t) - \omega_m.\mathrm{e}^{-t\frac{\omega_m}{2Q}} \sin(\omega_m t) \Big] \quad \omega_{inj} \neq \omega_m \end{aligned} \tag{B.8}$$

The envelope of $i_m(t)$ in this case, i.e. $\omega_{inj} \neq \omega_m$, has an underdamped response given by

$$i_{m,env}(t) = \frac{V_{inj}}{L_m|\omega_{inj}^2 - \omega_m^2|} \times \Bigg[\omega_{inj}^2 + \omega_m^2.\mathrm{e}^{-t\frac{\omega_m}{Q}} - 2\omega_{inj}.\omega_m.\mathrm{e}^{-t\frac{\omega_m}{2Q}}.\cos\Big((\omega_{inj} - \omega_m)t\Big)\Bigg]^{1/2} \tag{B.9}$$

By substituting $\omega_{inj} = \omega_m + \Delta\omega_{inj}$, and some manipulation, it can be shown that (B.9) reduces to (A.9).

REFERENCES

[1] X. Zhang and A. B. Apsel, "A Low-Power, Process-and-Temperature-Compensated Ring Oscillator With Addition-Based Current Source," *IEEE Transactions on Circuits and Systems I: Regular Papers*, vol. 58, no. 5, pp. 868–878, May 2011.

[2] H. Wang and P. P. Mercier, "A Reference-Free Capacitive-Discharging Oscillator Architecture Consuming 44.4 pW/75.6 nW at 2.8 Hz/6.4 kHz," *IEEE Journal of Solid-State Circuits*, vol. 51, no. 6, pp. 1423–1435, June 2016.

[3] A. Shrivastava, D. A. Kamakshi, and B. H. Calhoun, "A 1.5 nW, 32.768 kHz XTAL Oscillator Operational From a 0.3 V Supply," *IEEE Journal of Solid-State Circuits*, vol. 51, no. 3, pp. 686–696, March 2016.

[4] K. Hsiao, "A 1.89nw/0.15v self-charged xo for real-time clock generation," in *2014 IEEE International Solid-State Circuits Conference Digest of Technical Papers (ISSCC)*, Feb 2014, pp. 298–299.

[5] Y. Zeng, T. Jang, Q. Dong, M. Saligane, D. Sylvester, and D. Blaauw, "A 1.7nW PLL-assisted current injected 32KHz crystal oscillator for IoT," in *2017 Symposium on VLSI Circuits*, June 2017, pp. C68–C69.

[6] V. Raghunathan, S. Ganeriwal, and M. Srivastava, "Emerging techniques for long lived wireless sensor networks," *IEEE Communications Magazine*, vol. 44, no. 4, pp. 108–114, April 2006.

[7] J. P. Thomas, M. A. Qidwai, and J. C. Kellogg, "Energy scavenging for small-scale unmanned systems," *Journal of Power Sources*, vol. 159, no. 2, pp. 1494 – 1509, 2006. [Online]. Available: http://www.sciencedirect.com/science/article/pii/S0378775306001121

[8] O. Kanoun and H. Trankler, "Energy-Management for Power Aware Portable Sensor Systems," in *2006 IEEE Instrumentation and Measurement Technology Conference Proceedings*, April 2006, pp. 1673–1678.

[9] M. T. Penella and M. Gasulla, "A Review of Commercial Energy Harvesters for Autonomous Sensors," in *2007 IEEE Instrumentation Measurement Technology Conference IMTC 2007*, May 2007, pp. 1–5.

[10] H. Liu, Z. Sun, D. Tang, H. Huang, T. Kaneko, W. Deng, R. Wu, K. Okada, and A. Matsuzawa, "An ADPLL-centric Bluetooth Low-Energy transceiver with 2.3mW interference-tolerant hybrid-loop receiver and 2.9mW single-point polar transmitter in 65nm CMOS," in *2018 IEEE International Solid - State Circuits Conference - (ISSCC)*, Feb 2018, pp. 444–446.

[11] M. Ding *et al.*, "A 0.8V 0.8mm^2 Bluetooth 5/BLE digital-intensive transceiver with a 2.3mW phase-tracking RX utilizing a hybrid loop filter for interference resilience in

40nm CMOS," in *2018 IEEE International Solid - State Circuits Conference - (ISSCC)*, Feb 2018, pp. 446–448.

[12] K. A. A. Makinwa, A. Baschirotto, and P. Harpe, *Low-Power Analog Techniques, Sensors for Mobile Devices, and Energy Efficient Amplifiers*, 1st ed. Springer International Publishing, 2019.

[13] "Product Specification for PGEB014461." [Online]. Available: http://www.powerstream.com/p/PGEB014461.pdf

[14] "Product Specification for GMB-300910." [Online]. Available: http://www.powerstream.com/p/GMB300910.pdf

[15] "Product Specification for EFL700A39." [Online]. Available: http://www.st.com/st-webui/static/active/en/resource/technical/document/datasheet/CD00270103.pdf

[16] "Product Specification for CBC050." [Online]. Available: http://www.cymbet.com/pdfs/DS-72-01.pdf

[17] "Product Specification for CBC012." [Online]. Available: http://www.cymbet.com/pdfs/DS-72-02.pdf

[18] E. A. Vittoz, M. G. R. Degrauwe, and S. Bitz, "High-performance crystal oscillator circuits: theory and application," *IEEE Journal of Solid-State Circuits*, vol. 23, no. 3, pp. 774–783, June 1988.

[19] W. G. Cady, "Method of Maintaining Electric Currents of Constant Frequency," May 28 1921, US Patent 1,472,583. [Online]. Available: https://patents.google.com/patent/US1472583A

[20] G. W. Pierce, "Piezoelectric Crystal Resonators and Crystal Oscillators Applied to the Precision Calibration of Wavemeters," *Proceedings of the American Academy of Arts and Sciences*, vol. 59, no. 4, pp. 81–106, 1923. [Online]. Available: http://www.jstor.org/stable/20026061

[21] ——, "Electrical system," Oct. 18 1938, US Patent 2,133,642. [Online]. Available: https://www.google.mk/patents/US2133642

[22] E. A. Vittoz, *The Design of Low-Power High-Q Oscillators*. Boston, MA: Springer US, 2013, pp. 121–154. [Online]. Available: https://doi.org/10.1007/978-1-4419-8798-3_5

[23] E. Vittoz, *Low-Power Crystal and MEMS Oscillators*, 1st ed. Springer Netherlands, 2010.

[24] S. A. Blanchard and J. J. Rice, "Stimulated quick start oscillator," Nov. 16 2004, US Patent 6,819,195. [Online]. Available: https://www.google.mk/patents/US6819195

[25] M. Lin, "Fast wake-up crystal oscillating circuit," Nov. 21 2006, US Patent 7,138,881. [Online]. Available: https://www.google.mk/patents/US7138881

[26] R. van Langevelde, M. van Elzakker, D. van Goor, H. Termeer, J. Moss, and A. J. Davie, "An ultra-low-power 868/915 MHz RF transceiver for wireless sensor network applications," in *2009 IEEE Radio Frequency Integrated Circuits Symposium*, June 2009, pp. 113–116.

[27] Y. Chang, J. Leete, Z. Zhou, M. Vadipour, Y. T. Chang, and H. Darabi, "A differential digitally controlled crystal oscillator with a 14-bit tuning resolution and sine wave outputs for cellular applications," *IEEE Journal of Solid-State Circuits*, vol. 47, no. 2, pp. 421–434, Feb 2012.

[28] Texas Instruments, "CC2650 SimpleLink Multistandard Wireless MCU," 2015, datasheet. [Online]. Available: http://www.ti.com/lit/ds/symlink/cc2650.pdf

[29] S. Iguchi, H. Fuketa, T. Sakurai, and M. Takamiya, "Variation-tolerant quick-start-up CMOS crystal oscillator with chirp injection and negative resistance booster," *IEEE Journal of Solid-State Circuits*, vol. 51, no. 2, pp. 496–508, Feb 2016.

[30] D. Griffith, J. Murdock, and P. T. R∅ine, "A 24MHz crystal oscillator with robust fast start-up using dithered injection," in *2016 IEEE International Solid-State Circuits Conference (ISSCC)*, Jan 2016, pp. 104–105.

[31] M. Ding *et al.*, "5.3 a 95μw 24MHz digitally controlled crystal oscillator for IoT applications with 36nJ start-up energy and >13x start-up time reduction using a fully-autonomous dynamically-adjusted load," in *2017 IEEE International Solid-State Circuits Conference (ISSCC)*, Feb 2017, pp. 90–91.

[32] K. Lei, P. Mak, M. Law, and R. P. Martins, "A regulation-free sub-0.5V 16/24MHz crystal oscillator for energy-harvesting BLE radios with 14.2nJ startup energy and 31.8pW steady-state power," in *2018 IEEE International Solid - State Circuits Conference - (ISSCC)*, Feb 2018, pp. 52–54.

[33] J. de Boeck, "IoT: The Impact of Things," in *2015 Symposium on VLSI Circuits (VLSI Circuits)*, June 2015, pp. T82–T83.

[34] K. Philips, "Ultra Low Power short range radios: Covering the last mile of the IoT," in *ESSCIRC 2014 - 40th European Solid State Circuits Conference (ESSCIRC)*, Sept 2014, pp. 51–58.

[35] C. C. Enz, A. El-Hoiydi, J. D. Decotignie, and V. Peiris, "WiseNET: an ultralow-power wireless sensor network solution," *Computer*, vol. 37, no. 8, pp. 62–70, Aug 2004.

[36] Y. H. Liu *et al.*, "A 3.7mW-RX 4.4mW-TX fully integrated Bluetooth Low-Energy/IEEE802.15.4/proprietary SoC with an ADPLL-based fast frequency offset compensation in 40nm CMOS," in *2015 IEEE International Solid-State Circuits Conference - (ISSCC) Digest of Technical Papers*, Feb 2015, pp. 1–3.

[37] B. Gosselin and M. Sawan, "Event-driven data and power management in high-density neural recording microsystems," in *2009 Joint IEEE North-East Workshop on Circuits and Systems and TAISA Conference*, June 2009, pp. 1–4.

[38] D. Griffith, F. Dlger, G. Feygin, A. N. Mohieldin, and P. Vallur, "A 65nm CMOS DCXO system for generating 38.4MHz and a real time clock from a single crystal in 0.09mm^2," in *2010 IEEE Radio Frequency Integrated Circuits Symposium*, May 2010, pp. 321–324.

[39] M.-D. Tsai, C.-W. Yeh, Y.-H. Cho, L.-W. Ke, P.-W. Chen, and G.-K. Dehng, "A temperature-compensated low-noise digitally-controlled crystal oscillator for multi-standard applications," in *2008 IEEE Radio Frequency Integrated Circuits Symposium*, June 2008, pp. 533–536.

[40] S. Farahvash, C. Quek, and M. Mak, "A temperature-compensated digitally-controlled crystal Pierce oscillator for wireless applications," in *2008 IEEE International Solid-State Circuits Conference - Digest of Technical Papers*, Feb 2008, pp. 352–619.

[41] J. Lin, "A low-phase-noise 0.004-ppm/step DCXO with guaranteed monotonicity in the 90-nm CMOS process," *IEEE Journal of Solid-State Circuits*, vol. 40, no. 12, pp. 2726–2734, Dec 2005.

[42] B. Razavi, *RF Microelectronics*, 2nd ed. Upper Saddle River, NJ, USA: Prentice Hall Press, 2012.

[43] A. Rusznyak, "Start-up time of CMOS oscillators," *IEEE Transactions on Circuits and Systems*, vol. 34, no. 3, pp. 259–268, Mar 1987.

[44] O. Yamashiro, "Initiation circuit in a crystal-controlled oscillator," Aug. 2 1977, US Patent 4,039,973. [Online]. Available: https://www.google.mk/patents/US4039973

[45] K. Jackoski, J. Simmons, and G. Schwieterman, "Method and apparatus for optimizing an oscillator start up time," Dec. 1 1998, US Patent 5,844,448. [Online]. Available: https://www.google.mk/patents/US5844448

[46] S. Logan, "Oscillator with increased reliability start up," Jul. 9 1996, US Patent 5,534,826. [Online]. Available: https://www.google.mk/patents/US5534826

[47] S. A. Blanchard, "Quick start crystal oscillator circuit," in *Proceedings of the 15th Biennial University/Government/ Industry Microelectronics Symposium (Cat. No.03CH37488)*, June 2003, pp. 78–81.

[48] Y. I. Kwon, S. G. Park, T. J. Park, K. S. Cho, and H. Y. Lee, "An Ultra Low-Power CMOS Transceiver Using Various Low-Power Techniques for LR-WPAN Applications," *IEEE Transactions on Circuits and Systems I: Regular Papers*, vol. 59, no. 2, pp. 324–336, Feb 2012.

[49] H. Esmaeelzadeh and S. Pamarti, "A Precisely-Timed Energy Injection Technique Achieving 58/10/2μs Start-Up in 1.84/10/50MHz Crystal Oscillators," in *Proceedings of the 2017 IEEE Custom Integrated Circuits Conference*, May 2017, pp. 1–4.

[50] ——, "A Quick Startup Technique for High- Q Oscillators Using Precisely Timed Energy Injection," *IEEE Journal of Solid-State Circuits*, vol. 53, no. 3, pp. 692–702, March 2018.

[51] K. Sundaresan, P. E. Allen, and F. Ayazi, "Process and temperature compensation in a 7-MHz CMOS clock oscillator," *IEEE Journal of Solid-State Circuits*, vol. 41, no. 2, pp. 433–442, Feb 2006.

[52] N. Sadeghi, A. Sharif-Bakhtiar, and S. Mirabbasi, "A 0.007-mm^2 108-ppm/°C 1-MHz Relaxation Oscillator for High-Temperature Applications up to 180°C in 0.13-μm CMOS," *IEEE Transactions on Circuits and Systems I: Regular Papers*, vol. 60, no. 7, pp. 1692–1701, July 2013.

[53] J. Wang, W. L. Goh, X. Liu, and J. Zhou, "A 12.77-MHz 31 ppm/°C On-Chip RC Relaxation Oscillator With Digital Compensation Technique," *IEEE Transactions on Circuits and Systems I: Regular Papers*, vol. 63, no. 11, pp. 1816–1824, Nov 2016.

[54] Y. Tokunaga, S. Sakiyama, A. Matsumoto, and S. Dosho, "An On-Chip CMOS Relaxation Oscillator With Voltage Averaging Feedback," *IEEE Journal of Solid-State Circuits*, vol. 45, no. 6, pp. 1150–1158, June 2010.

[55] Y. K. Tsai and L. H. Lu, "A 51.3-MHz 21.8-ppm/°C CMOS Relaxation Oscillator With Temperature Compensation," *IEEE Transactions on Circuits and Systems II: Express Briefs*, vol. 64, no. 5, pp. 490–494, May 2017.

[56] J. Lu, S. Onishi, and Y. Tsuzuki, "A discussion on start-up time of crystal oscillators," *IEE J. Trans. Electron. Inf. Syst.*, vol. 111-C, no. 9, pp. 384–389, Sep 1991, (in Japanese).

[57] A. M. Pappu, X. Zhang, A. V. Harrison, and A. B. Apsel, "Process-Invariant Current Source Design: Methodology and Examples," *IEEE Journal of Solid-State Circuits*, vol. 42, no. 10, pp. 2293–2302, Oct 2007.

[58] S. Kang and Y. Leblebici, *CMOS Digital Integrated Circuits Analysis & Design*, ser. McGraw-Hill Series in Electrical and Computer Engineering. McGraw-Hill Education, 2003. [Online]. Available: https://books.google.com/books?id=l1XyQ7RJ36cC

[59] D. Yoon, T. Jang, D. Sylvester, and D. Blaauw, "A 5.58 nw crystal oscillator using pulsed driver for real-time clocks," *IEEE Journal of Solid-State Circuits*, vol. 51, no. 2, pp. 509–522, Feb 2016.

[60] B. Razavi, *Design of Analog CMOS Integrated Circuits*, 2nd ed. McGraw-Hill Education, 2015.

[61] J.-S. Lee, M.-S. Keel, S.-I. Lim, and S. Kim, "Charge Pump with Perfect Current Matching Characteristics in Phase-Locked Loops," *Electronics Letters*, vol. 36, no. 23, pp. 1907–1908, Nov 2000.

[62] M. Schwartz, W. Bennett, and S. Stein, *Communication Systems and Techniques*, ser. An IEEE press classic reissue. Wiley, 1995.